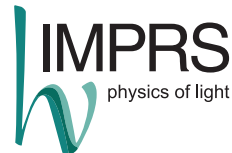


NOVEL METHODS IN OPTICAL AND MECHANICAL BIOSENSORS



FRIEDRICH-ALEXANDER
UNIVERSITÄT
ERLANGEN-NÜRNBERG



Der Naturwissenschaftlichen Fakultät
der Friedrich-Alexander-Universität Erlangen-Nürnberg
und
Das Max-Planck-Institut für die Physik des Lichts

zur
Erlangung des Doktorgrades Dr. rer. nat.

vorgelegt von
Aaron Webster
aus Oregon, USA

Als Dissertation genehmigt von der Naturwissenschaftlichen Fakultät der Universität Erlangen-Nürnberg

Tag der mundlichen Prüfung: Saturday 16th April, 2016

Evaluation Committee

First Advisor

Dr. habil. rer. nat. Frank Vollmer, PhD
Laboratory of Biophotonics and Biosensing
Max Planck Institute for the Science of Light
Günther-Scharowsky-Str.1 / Bau 24
91058 Erlangen

Second Advisor

Prof. Dr. Ulf Peschel
Institute of Optics, Information and Photonics
University Erlangen-Nürnberg
Günther-Scharowsky-Str.1 / Bau 24
91058 Erlangen

Abstract

The commercialization of biosensing is driven by application. Toward this goal, many interesting physical phenomena inherent in biosensing platforms are de-emphasized in favor of a quantitative and repeatable assay. Such phenomena are often treated as a source of noise to be overcome, and, as the engineering of a platform is perfected towards a specific biodetection goal, the principles of these phenomena become obscured to those who employ it solely as a tool in pursuit of other matters.

This is a ubiquitous pattern in science, perhaps the best examples of which are two most ubiquitous biotransducers: the optical surface plasmon resonance (SPR), and the mechanical piezoelectric quartz crystal microbalance (QCM). These two devices, the subject of the present work, both possess novel modes of operation which extend their versatility to other bio-relevant sensing applications.

In the optical regime, surface plasmon polaritons (SPPs) excited evanescently by light are by far the most popular label-free affinity biotransducer for monitoring bulk refractive index changes. The sensitivity of SPR is primarily due to the field enhancement by SPPs on the sensor surface, however SPPs themselves also possess high spatial resolution beyond the diffraction limit; a property typically absent as specific feature of the SPR sensorgram. In this work, it is shown that by considering optical speckle from single and multiply scattered SPPs inherent in the SPR signal itself, an entirely new set of information can be obtained descriptive of the underlying scattering microstructure. Furthermore, it is demonstrated that the motion and addition of single nanoparticles can be resolved in an unmodified SPR setup, whereby the breadth of SPR experiments may be extended to encompass both bulk sensing and discrete events on the nanoscale.

Moving into the mechanical regime, the sensitivity, low cost, ease of use, and integrability have made the piezoelectric quartz crystal microbalance an ideal biotransducer for real time monitoring properties such as viscoelasticity, as well as an affinity sensor for mass adsorption. Naturally, these desirable features do not come without disadvantages: the underlying mechanical properties of the sample are often not revealed by the relative and stepwise changes in the QCM sensorgram, an issue complicated by choice of theoretical model. Here it is shown that application of controlled centrifugal forces in a QCM assay has a profound utility in revealing the underlying biomechanical properties of a sample. This *centrifugal force quartz crystal microbalance* concept works by modifying the QCM-sample coupling mechanism. Centrifugal force is demonstrated to be useful in not only to enhancing the sensitivity of a traditional QCM measurement, but also in obtaining the sample's complex biomechanical properties repeatedly *in situ* and in real time.

Contents

Overview and Organization	2
I Surface Plasmon Resonance	4
1 Introduction	5
1.1 Historical Perspective	6
2 Surface Plasmon Polaritons	8
2.1 Maxwell's Equations	8
2.1.1 The Wave Equation	9
2.1.2 Complex Permittivity	10
2.2 SPPs at a Metal-Dielectric Interface	11
2.2.1 Dispersion Relation	13
2.3 Multilayer Systems	14
2.3.1 Photonic Crystal Structures	16
2.4 Fresnel Relations	17
2.4.1 Prism Coupled Excitation	17
2.4.2 Near and Far Fields	19
2.5 Conically Scattered Light	20
3 Experimental	25
3.1 Setup	25
3.1.1 Imaging Sensor	27
3.2 Sputtering	28
3.3 Surface Modifications	29
3.3.1 Measurement of Surface Roughness	29
3.4 Nanoparticle Adsorption	31
3.5 Cytop	31
3.5.1 Spin Coating	33
3.6 Microfluidics	34
3.7 Image Processing	35
3.7.1 Coordinates of the Imaging Sensor	35
3.7.2 Extracting the Speckle Line	37
4 Interference	38

4.1	Theory	38
4.2	Experiment	39
4.2.1	Interference and Diffraction	42
5	Speckle	46
5.1	Introduction	46
5.1.1	Objective Speckles	47
5.2	Intensity Distribution and Contrast	47
5.3	Limiting Cases	48
5.3.1	A Small Number of Scatterers	49
5.3.2	A Strong Single Scatterer	49
5.3.3	PDF of the Cone Speckle	50
5.4	Size of a Speckle	50
5.4.1	Experiment	52
5.5	Bulk Refractive Index Sensitivity	53
5.5.1	Angular Interrogation	53
5.5.2	Intensity Interrogation	54
5.6	Refractive Index Effect On Speckle	55
6	Scattering Microstructure	61
6.1	Introduction	61
6.2	Scattering Model	61
6.2.1	Phase Accumulation and Extension to the Far Field	63
6.2.2	Transition from Single to Multiple Scattering	65
6.2.3	Sensitivity and Scattering Paths	66
6.3	Addition of a Single Scatterer	66
6.3.1	Motivation	66
6.3.2	Quantifying Changes in Speckle	67
6.3.3	Theoretical Sensitivity	67
6.3.4	Experiment	67
II	The Centrifugal Force Quartz Crystal Microbalance	72
1	Foundations	73
1.1	Introduction	73
1.2	Historical Perspective	74
1.3	Theory	75
1.3.1	Physical Manifestation	75
1.3.2	The Small Load Approximation	76
1.3.3	Mechanical Model	77
2	Experimental	78
2.1	Setup	78
2.2	Noise and Comparison to QCM-D	79
2.3	Environmental Effects and Noise	80

3 Load Situations	83
3.1 Air	84
3.2 Deionized Water	84
3.3 Free Particles	85
3.4 Oligo-Attached Particles	86
3.4.1 Verification of the Oligo Attachment	87
3.5 Lambda DNA	87
3.6 Tethered Particles	88
3.7 Particle Sizing	89
4 Simulation	92
4.1 Introduction	92
4.2 Finite Element Modeling	92
4.2.1 Extracting Shifts	94
4.2.2 Verification Examples	94
4.3 Analysis and Prediction	96
4.3.1 Particles	96
4.3.2 Sample Viscoelasticity	98
5 Conclusions	100
A Appendix	101
A.1 Bluestein's FFT Algorithm	101
A.2 Abeles Matrix Formalism	103
A.2.1 Matrix Formalism	103
A.3 Reference Data	104
A.4 Colophon	104
A.5 Dipole-Dipole Simulation	105
Declaration of Originality	118
Acknowledgements	119

List of Figures

2.1	Geometry and coordinate system for a single interface which can support SPPs. Domain D_1 has permittivity ϵ_1 , typically a dielectric, and domain D_2 a permittivity ϵ_2 , typically a conductive metal.	12
2.2	Dispersion relation for photons and plasmons for a single interface consisting of a dielectric ϵ_1 , fused silica, and a metal ϵ_2 , gold using the Lorentz-Drude model, also in Figure A.2. Conditions under which SPPs are excited are at the intersection between the photon line in a dielectric and corresponding SPP line.	14
2.3	Geometry and coordinate system for the multilayer system.	15
2.4	Dispersion relation for the multilayer interface system, shown as the difference between the right-hand side (RHS) and left-hand side (LHS) of Equation 2.56. SPP excitation occurs in the red areas. This specific system is also used in the experiment. Plot is for a three-layer interface system with $\epsilon_1 = 1.331$, ϵ_2 Au using the frequency-dependent Lorentz-Drude model, $\epsilon_3 = 1.332$, and the thickness of D_2 is 15 nm.	16
2.5	Prism coupled excitation of SPPs in the Kretschmann configuration, (a), a three-layer interface system, and (b), a four-layer interface system. . .	17
2.6	Fresnel reflection coefficient for p polarization, $ r^p ^2$, a function of angle and excitation wavelength for conventional (right) and long-range (left) SPP structures in a Kretschmann ATR configuration. Coupling of light into SPPs is possible in regions of low reflectivity to the right of the critical angle for total internal reflection (dashed line).	19
2.7	Near and far field intensities for excitation of conventional SPPs in a three-layer system. $\lambda_0 = 660$ nm, $n_1 = 1.5142$, $n_2 = 0.2843 + 3.3825i$, and $n_3 = 1.3310$. The thickness of the metal layer is 45 nm.	21
2.8	Near and far field intensities for excitation long-range SPPs in a symmetric layer system $\lambda_0 = 660$ nm, $n_1 = 1.5142$, $n_2 = 1.3489$, $n_3 = 0.2843 + 3.3825i$, and $n_4 = 1.3310$. The thickness of the metal layer is 16.97 nm.	22
2.9	Coordinates of the conically scattered light.	23
2.10	Comparison of the angular optical profile of the cone and notch. The cone signal has been inverted and normalized to the same range as the notch for comparison.	23
3.1	Image of the experimental setup with the functional components annotated.	25

3.2	Schematic of the experimental setup. Description in text.	26
3.3	The cone sensor, an IDS USB 2.0 8 bit CMOS sensor, removed from its housing allowing close positioning with respect to the prism.	27
3.4	Rest light measurements, the ratio of polarization intensities I_p/I_s , comparing an unmodified “smooth” silver film to a “rough” film sputtered using heat pretreatment technique. For comparison, Equation 3.1 shown as an example of theoretical perfect smoothness.	30
3.5	UV-Vis absorbance spectrum of 25, 50, 75, and 100 nm spherical gold nanoparticles used in nanoparticle adsorption experiments.	31
3.6	Reflectivity of a thin Cytop layer on BK7 at $\theta = 45^\circ$. Shown is the experimental data and the best-fit with Equation 3.3. Calculated layer thickness was 1150 nm.	33
3.7	Schematic of the microfluidic cell as integrated in the experiment.	35
3.8	Geometry for determining the sensor distance d	35
3.9	Illustration of the unwrapping procedure for the cone image. The spline region (highlighted in yellow) in the above image is converted to the rectangular region in the image below for further post-processing.	37
4.1	Section of the cone exhibiting one-sided interference fringes. System parameters: $\lambda_0 = 632.8 \text{ nm}$, $n_1 = 1.9961$ (LAH79), $n_2 = -14.48 + 1.09i$ (silver), $n_3 = 1.0$ (air), and $d_2 = 48 \text{ nm}$	38
4.2	Experimental setup. Light from a laser passes through beamsplitter BS passing p-polarized light and expanded by two lenses, f_1 and f_2 . Mirrors m_1 and m_2 steer the expanded beam to lens f_3 , focusing the light onto the hypotenuse of a hemispherical prism. Lens f_4 re-images the reflected field to a beam profiler where it is recorded.	40
4.3	Theoretical and experimental values of $ E_{\text{notch}}(x, z) ^2$ and $ E_{\text{cone}}(x, z) ^2$ obtained for three characteristic propagation distances. Theoretical values are solid lines, while experimental values are shown with points. Distances are approximate. Inset is the experimentally obtained optical intensity.	41
4.4	Predictions of the optical field made by BAIDA [1]. On the left is the field on the metal-glass (1–2) interface. On the right, the field on the metal-vacuum (2–3) interface. Compare with the near fields for the notch and cone in Figure 4.3.	42
4.5	Images of the optical field in the specular direction as the focal plane of f_4 is moved from (a), best focus, to (i), the far field. All images have been normalized relative to themselves.	43
4.6	Images of the optical field for the section of the conically scattered light as the focal plane of f_4 is moved from (a), best focus, to (f), the far field. All images have been normalized relative to themselves.	44
4.7	Photon scanning tunneling microscope image of the metal-vacuum (2–3) interface from DAWSON [2]. No scale was given except that the $1/e$ propagation length was $13.8 \mu\text{m}$. Compare with the near field cone image in Figure 4.3. The model of DAWSON assumes a 2.65 nm layer of Ag_2S on top of the silver layer, hence the reduced SPP propagation length.	45

4.8	Comparison of the propagated $\tilde{r}_{123}(k_x)$ versus $(\tilde{r}_{123}(k_x) - \tilde{r}_{12})$. Note that interference fringes occur in both cases.	45
5.1	A portion of the cone speckle, distorted by a lens and projected onto a piece of paper.	46
5.2	Experimental verification of the speckle intensity PDF for a strong scatterer (left) versus traditional Rayleigh speckle (right). Surface images are seen below their respective histograms.	50
5.3	Intensity PDF for light in the cone. Top: histogram. Bottom: unwrapped raw data on the sensor.	51
5.4	Illuminated spot size (left) and corresponding specklegram (right) for three different example spot sizes. Notice that the angular size of the speckles is not significantly different in the three cases.	56
5.5	Speckle size versus spot size for 57 nm AuNPs adsorbed onto a gold surface in a long-range surface plasmon (symmetric) structure.	57
5.6	Three sections of cone speckle taken for a conventional surface plasmon setup (Air-Ag-BK7) taken using the setup of Figure 4.2. The layer structure is described in Section 4.2. From left to right: defocused, tightly focused, tightly focused on a defect. The actual spot size was not measured in this specific experiment.	57
5.7	(top) Angular sensitivity of the notch and the cone for the Kretschmann three-layer (SP) system. $\lambda_0 = 660$ nm, $n_1 = 1.5142$, $n_2 = 0.2843 + 3.3825i$, and $n_3 = 1.3310 + \Delta n$. The thickness of the metal layer is 45 nm. (bottom) Angular sensitivity of the notch and the cone for the Kretschmann four-layer (LRSPP) system. $\lambda_0 = 660$ nm, $n_1 = 1.5142$, $n_2 = 1.3489$, $n_3 = 0.2843 + 3.3825i$, and $n_4 = 1.3310 + \Delta n$. The thickness of the metal layer is 16.97 nm.	58
5.8	Combined cone images of a sample without (top, $\Delta n = 0$) and with (bottom, $\Delta n = 0.01$) a refractive index perturbation.	58
5.9	Simulated speckle fields and PDF of the resulting intensities for the case of a small number of scatterers. Statistics are obtained from a single realization, which is shown to the left of the histogram. Relative locations of the scatterers are denoted by a circle.	59
5.10	Simulated speckle fields and PDF of the resulting intensities for the case of a single scatterer r times brighter than mean background intensity. . .	60
6.1	A simplified SPP scattering model. An SPP is excited within the illuminated region at its creation point and follows a scattering path amongst fixed point scatterers (numbered). The scattering path can include one (single scattering) or more (multiple scattering) scatterers. The beam creating the illuminated region is incident from the $+x$ direction.	63
6.2	Ensemble-averaged Monte Carlo simulation comparing the Pearson product-moment correlation C_I for the addition of a single scatterer in both single and multiple scattering systems.	68
6.3	Change in speckle measured through the PPMCC (top) before (bottom left) and after (bottom right) the adsorption of a nanoparticle.	69

6.4	Change in speckle measured through the PPMCC (top) before (bottom left) and after (bottom right) the adsorption of a nanoparticle.	69
6.5	Visual change in the specklegram upon the adsorption of a nanoparticle. This figure is taken from the same data and timeframe as a compliment to Figure 6.4.	70
6.6	Statistics of nanoparticle adsorption. Right: event frequency. Left: inter-event time. Adsorption statistics match well that of theoretical Poisson statistics.	71
1.1	A 25 mm 5 MHz quartz crystal microbalance.	73
1.2	Conceptual drawing of a transverse shear wave. An electric potential is applied along the y axis, causing the crystal to shear.	75
1.3	Mass-spring-dashpot mechanical model for a QCM under load. In the weak coupling regime the system experiences a positive frequency shift identified with inertial loading, while in the strong coupling regime the system experiences a negative frequency shift identified with mass loading. The fixed relationship between the shift in frequency Δf and bandwidth $\Delta\Gamma$ trace out a circle-like path as a parametric function of k_L	76
2.1	Annotated picture of the prototype CF-QCM from above. The centrifuge is a standard swinging bucket type.	78
2.2	Holder for the crystal, shown split into its two halves. The crystal is inside the holder on the right.	79
2.3	Parametric plot showing temperature drift during an experimental run from 0 to 90 g and back, taking 200 s.	82
3.1	Overview of the CF-QCM and its sensorgram. (a) Schematic of the experimental setup. (b) Example CF-QCM sensorgram for a sample consisting of $1 \mu\text{m}$ particles in water, $N_L = 1.58 \times 10^{11} \text{ particle m}^{-2}$, in the “loading” configuration (inset). The horizontal arrows indicate the motion of the QCM’s transverse shear mode.	83
3.2	Load situations. Change in frequency Δf and bandwidth $\Delta\Gamma$ (in hertz, inferred from motional resistance) of the CF-QCM under different load situations as the centripetal acceleration is directed into (<i>loading</i> , represented by circles with the top half colored) and out of (<i>unloading</i> , represented by circles with the bottom half colored) the plane of the crystal. The situations are (a) unloaded crystal in air, (b) deionized water, (c) free $1 \mu\text{m}$ diameter streptavidin-coated polystyrene particles, $N_L = 1.58 \times 10^{11} \text{ particle m}^{-2}$, (d) $2 \mu\text{m}$ diameter streptavidin-coated paramagnetic particles, $N_L = 1.65 \times 10^{10} \text{ particle m}^{-2}$, attached with 25 mer oligonucleotides, (e) lambda DNA only attached to the gold electrode, and (f) $25 \mu\text{m}$ diameter streptavidin coated polystyrene particles, $N_L = 3.25 \times 10^7 \text{ particle m}^{-2}$, tethered to the sensor surface with 48 kbp lambda DNAs. Error bars are derived from uncertainties (standard deviation) in the centrifuge both spinning up and spinning down in a single experimental run.	90

3.3	Free particles on the surface of the QCM. The particle number density N_L was determined by manually counting particles imaged in a microscope and dividing by the corresponding area.	91
3.4	Particle sizing. Method for sizing micron-sized particles using the CF-QCM. Δf versus $\Delta\Gamma$ is plotted parametrically as a function of g-force, and the data is fit to a circle. The point on the circle for which $\Delta\Gamma = 0$ and $\Delta f < 0$ provides an estimate of mass adsorption and thus particle size. Results for particles with diameters $\bar{d}_{\text{actual}} = 1, 2, 15$, and $25 \mu\text{m}$ are shown in Table 3.1. Fit circle has a radius of 55.77 Hz and a center of $(-37.83, 41.05) \text{ Hz}$	91
4.1	Two-dimensional computational domain for the finite element simulation.	92
4.2	Finite element prediction of a shear evanescent wave at 5 MHz in a liquid with $\rho = 1 \text{ g cm}^{-3}$ and $\eta = 1 \text{ mPa s}$, compared with theory (Equation 4.14).	95
4.3	Comparison of Δf and $\Delta\Gamma$ versus viscosity η for both the finite element simulation and Equation 4.12. (a) $\eta'' = 0$ and η' is swept (a Newtonian liquid). (b) $\eta' = 1 \text{ mPa s}$ and η'' is swept.	96
4.4	Simulation of the CF-QCM behavior. Finite element simulation for a $10 \mu\text{m}$ polystyrene sphere (cylinder in 2D) as a function of contact surface density A_c . Negative values of A_c indicate positive separation from the surface. Discussion in the text. (a-c): Density plot of the pressure P and velocity U distributions. Units are normalized. Note that in all situations with finite contact radius, stress is annularly distributed around the edge of the contact as per the Mindlin model [3]. (main plot): Shifts in Δf and $\Delta\Gamma$. Points on the plot are a best fit of the mechanical model, Equation 1.1, to the simulation.	97
4.5	Simulated response for different materials. Finite element simulation of normalized Δf and $\Delta\Gamma$ for three categories of samples as a function of contact surface density, A_c . Negative values of A_c indicate the sample has not made contact with the sensor surface. The samples are (a) cells, $G_L = (10 + 50i) \text{ kPa}$, (b) agarose microparticles, $G_L = (78 + 78i) \text{ kPa}$ and (c) lysozyme microcrystals, $G_L = (0.659 + 0.235i) \text{ GPa}$	99
A.1	Coordinates in the fast Fourier transform.	101
A.2	Comparison of the complex permittivity for gold calculated using the Drude ($\epsilon'_D + i\epsilon''_D$) and the Lorentz Drude ($\epsilon'_{LD} + i\epsilon''_{LD}$) model compared with experimental results by THÈYE [4]	105

List of Tables

2.1	Complex permittivity for select metals at $\lambda = 660$ nm calculated using the Lorentz-Drude model. Model parameters are from Refs. [5] and [6].	18
3.1	Standard deviation of the spin speed at nominal angular speeds for the hard disk spin coater.	34
5.1	Theoretical maximum angular sensitivity, $\Delta\theta/\Delta n$, in degrees per refractive index unit, for the configurations in Figure 5.7.	54
5.2	Theoretical maximum intensity sensitivity, $\Delta I/\Delta n$, for the configurations in Figure 5.1.	55
2.1	Environmental effects on the QCM resonance frequency.	81
3.1	Normalized frequency and bandwidth shifts (in Hz m^2) at 1 and 90 g for various particle sizes in water. The quoted diameter \bar{d} is the sample mean. <i>p</i> : polystyrene particles, <i>m</i> : magnetite-coated polystyrene.	86

Overview and Organization

Organization

This work is organized into two distinct parts: Part I, which contains the investigations regarding interference and scattering in surface plasmon resonance, and Part II which contains investigations regarding the centrifugal force quartz crystal microbalance.

Part I begins with Chapter 1, an introduction to the historical perspective motivating the work. Chapter 2 proceeds with a short mathematical derivation of the existence of SPPs and the conditions under which they may be excited. The derivation furthers the motivation for specific choices of materials and experimental configurations in Chapter 3. Accordingly, Chapter 3 describes the physical experiment: mechanical construction, protocols, and data analysis. Chapter 2 and Chapter 3 form the mathematical and physical basis for the remaining part of this work.

Discussion and analysis of new results for Part I are the subject of the remaining three chapters. Chapter 4 describes a newly discovered interference phenomena and its utility in the context of conventional SPR bulk refractive index sensing measurements.

Following, Chapter 5 describes one of the most significant properties of the experiment: cone speckle. A formalism for describing cone speckle is proposed, relating its properties to classical optical speckle fields using statistical properties, correlations, refractive index perturbations, and single and multiple scattering phenomena.

Finally, Chapter 6 describes investigations regarding the influence of cone speckle on the underlying scattering microstructure. It is demonstrated that in an unmodified conventional SPR setup, it is possible to resolve the motion and presence of single nanoparticles, extending the breadth of SPR experiments to encompass both bulk sensing and discrete events.

Moving from optical to mechanical biosensors, Part II describes experiments with a new type of instrument, the centrifugal force quartz crystal microbalance (CF-QCM), as a tool designed to investigate the mechanical properties of discrete and bulk samples interacting with a QCM under centrifugal force. Part II begins with Chapter 1, motivating the instrument and providing a historical context for its invention. Chapter 1 also describes the relevant physical model used allowing one to predict its response under different samples and load situations.

As in Chapter 3 of Part I, Chapter 2 of Part II details all experimental aspects of the

instrument: its construction, operation, and data acquisition circuitry. Inherent additions to the QCM sensorgram, environmental effects and noise, are also considered.

The experimental results of Part II are presented in Chapter 3, describing the behavior of the CF-QCM for a wide range of samples: bulk liquid, discrete microparticles, and viscoelastic layers of DNA. The different samples are investigated both free and, in the case of microparticles, attached to the surface with DNA.

Finally, predictions regarding CF-QCM behavior for samples which have not yet been subject to experiment are contained in Chapter 4, facilitated by a finite element simulation. Complimenting the experiment, the finite element simulation is used to predict the response of discrete biomolecules: cells, agarose microparticles, and lysozyme micro-crystals. These bioparticles and molecules are representative of the enormous range of viscoelastic material properties found in nature and highlight the potential uses of the CF-QCM sensing concept.

Part I

Surface Plasmon Resonance

1 | Introduction

Biosensors based on surface plasmon resonance (SPR) play a central role as a simple and remarkably responsive label-free method for characterizing and quantifying biomolecular interactions [7] [8]. Among the most popular of these sensor platforms are those which use the excitation of surface plasmon polaritons (SPPs) on thin metal films in prism-coupled configurations [9]. Such platforms, despite their ubiquity and commercial success, are host to an amazing depth of useful phenomena not yet explored in the context of biosensing. In addition to the high field enhancement responsible for their high sensitivity in bulk refractive index measurements, the SPPs themselves possess high spatial resolution beyond the diffraction limit; a property traditionally absent as a specific feature of an SPR sensorgram.

The high spatial resolution of SPPs is perhaps best exemplified by an instrument known as a scanning plasmon optical microscope [10] [11] (SPOM). In a SPOM, surface plasmons excited on a metal surface are scattered into a cone by a sharp tip, typically in the same class as those used for scanning tunneling microscopes (STMs) with single-atom sharpness [12]. By raster scanning the tip over a surface of interest where SPPs are excited, a sub-micron image of the scattering microstructure may be reconstructed from the tip-dependent intensity of the conically scattered light. Specific to the SPOM configuration, intensity of the conically scattered light has been shown to be specifically sensitive to defects or irregularities on the surface [11].

The present work is inspired by the SPOM concept, importing it into the heart of SPR biosensing. Instead of the tip used in the SPOM setup, nanoparticles introduced into a fluidic chamber in a typical SPR biosensor are used in conjunction with optical speckle in the conically scattered light signal to obtain information regarding the underlying scattering microstructure. Specifically, it is demonstrated that by monitoring speckle in the cone, the motion and addition of single nanoparticles can be detected, extending the breadth of SPR experiments to encompass both bulk sensing and discrete events. In addition, the present work investigates the optical structure of the conically scattered light, a field which contains additional bio-relevant features such as near field self-interference, speckle, and optical vortices. This completely novel sensing modality suggests several possible avenues for advancing the detection limits of surface plasmon based biosensors for both single particles and bulk refractive index measurements.

1.1 Historical Perspective

The theoretical groundwork for the existence of surface plasmon polaritons (SPPs) was first introduced by RICHIE in his seminal 1957 paper *Plasma Losses by Fast Electrons in Thin Films* [13]. Like any scientific work, Richie's was incremental and has its roots in earlier theoretical proposals by PINES and BOHM [14] [15]. Ultimately the work of RICHIE, PINE, and BOHM would explain a bulk SPP phenomena known as "Wood's anomaly" — a sharp and spectrally narrow energy loss observed in diffraction gratings by WOOD in 1902 [16] [17].

Optical excitation of surface plasmons was made accessible through pioneering work in the late 1960's by KRETSCHMANN [18], RAETHER [19] and OTTO [20]. These SPP experiments used the principle of attenuated total reflection (ATR) in a prism to excite surface plasmons evanescently. A great deal of research on the topic of surface plasmons took place in the subsequent decade, including an improved theoretical understanding based on the Fresnel relations [21] and investigation of conically scattered light in the presence of surface roughness [22]. A concise historical overview of prism-coupled SPP studies can be found in [23].

The introduction of surface plasmon resonance (SPR) as a biosensing platform began in the early 1980's with work by LIEDBERG, NYLANDER and LUNDSTROM [24] who described the extraordinary sensitivity of surface plasmon resonance to perturbations of the refractive index of a medium on one side of the metal film. The subsequent commercialization of SPR biosensors has largely been influenced by these authors and their spinoff company Pharmacia Biosensor AB (now Biacore) [25].

The commercial success of SPR biosensors brought about a knowledge gap between the biosensing community and their more theoretical predecessors from whom the field owes its genesis; i.e. the scope of SPR biosensing experiments is disproportionately narrower than the breadth of phenomena discovered since RICHIE. For example in 2005 and 2007, two papers [26] [27] based on theoretical work by CHUANG [28] and CHEN [21] reported a curious interference pattern occurring in the specularly reflected light for certain systems (among them, Kretschmann-Raether type) illuminated with a focused beam. The interference pattern was also independently reported a year later by SCHUMANN and GREGORY [29]. Observation of the interference required nothing more than the addition of a lens pair to an otherwise ubiquitous optical setup, but it somehow escaped attention during earlier research.

The thrust of this work is primarily inspired by experiments done at the University of Oregon in the laboratory of GREGORY, summarized in a 2009 thesis *Surface Plasmon Random Scattering and Related Phenomena* [30] by SCHUMANN. SCHUMANN describes a series of experiments using a scanning apertureless near-field probe in a Kretschmann-Raether type configuration [10]. The probe, composed of a sharp tungsten tip, was shown to elastically scatter SPPs in a way analogous to surface roughness, but in this case its location and interaction could be precisely determined. By controlling the location of a single scatterer among a fixed background, SCHUMANN showed the possibility of determining the entire surface scattering microstructure from the scattered light alone.

This work demonstrates that analogous experiments can be carried out in the context of biosensing using gold nanoparticles as scatterers.

The final important historical development was on correlations in elastic multiple scattering through disordered media. Most notable is a seminal paper by FENG, LEE, STONE, and DOUGLAS [31]. The authors showed that the seemingly random fluctuations in the output channel contain correlations which track the behavior of the input channel. In the optical regime such fluctuations are known as speckle. Statistical properties have been explored in depth by GOODMAN [32] [33]. Correlations in optical speckle patterns were explored in depth using theoretical methods by BERKOVITS and FENG [34], establishing that the multiple scattering regime is extraordinarily sensitive to both the position [35] and motion [36] of even a single scatterer. The motion of scattering locations in a multiple scattering system has important implications in many diverse fields of study: diffusive wave spectroscopy [37], tracking and identification of targets with radio waves (the “cruise missile” problem [38]), fluctuations in signal power in cellular telephone networks [39], and very recently in detecting stress fractures in aggregates such as concrete [40].

2 | Surface Plasmon Polaritons

2.1 Maxwell's Equations

The existence of SPPs and their excitation conditions can be derived from Maxwell's equations. Beginning here, the differential form of Maxwell's equations [41] [42] including external sources are

$$\nabla \cdot \mathbf{D} = \rho \quad \text{Gauss's law} \quad (2.1)$$

$$\nabla \cdot \mathbf{B} = 0 \quad \text{Gauss's law for magnetism} \quad (2.2)$$

$$\nabla \times \mathbf{E} = -\frac{\partial \mathbf{B}}{\partial t} \quad \text{Faraday's law of induction} \quad (2.3)$$

$$\nabla \times \mathbf{H} = \frac{\partial \mathbf{D}}{\partial t} + \mathbf{J} \quad \text{Ampere's law with Maxwell's correction,} \quad (2.4)$$

where \mathbf{E} is the electric field, \mathbf{B} is the magnetic field, \mathbf{D} is the electric displacement field with an external charge density ρ , and \mathbf{H} is the auxiliary magnetic field with current density \mathbf{J} .

In formulating Maxwell's equations it is assumed all electromagnetic propagation takes place in a *simple dielectric*, that is

1. The polarization density \mathbf{P} is linear with the electric field \mathbf{E} ,

$$\mathbf{P} = \epsilon_0 \chi_e \mathbf{E}. \quad (2.5)$$

with χ_e defined as the electric susceptibility. From Equation 2.5 and the definition of \mathbf{D} ,

$$\mathbf{D} = \epsilon_0 \mathbf{E} + \mathbf{P}, \quad (2.6)$$

with ϵ_0 is the permittivity of free space, one can simplify the \mathbf{D} -field as

$$\mathbf{D} = \epsilon_0 \mathbf{E} + \mathbf{P} \quad (2.7)$$

$$= \epsilon_0 (1 + \chi_e) \mathbf{E} \quad (2.8)$$

$$= \epsilon \mathbf{E}. \quad (2.9)$$

In Equation 2.9, ϵ is defined as the permittivity of the dielectric. The convention is taken that variables with a subscript 0 can always be assumed to be *in vacuo*, while material-dependent counterparts have no subscript.

2. The magnetization \mathbf{M} , related to the auxiliary magnetic field by

$$\mathbf{M} = \mu_0 \chi_m \mathbf{H}, \quad (2.10)$$

where χ_m is the volume magnetic susceptibility. Equation 2.10 allows the magnetic field to be rewritten as

$$\mathbf{B} = \mu_0 (\mathbf{H} + \mathbf{M}) \quad (2.11)$$

$$= \mu_0 (1 + \chi_m) \mathbf{H} \quad (2.12)$$

$$= \mu \mathbf{H}, \quad (2.13)$$

where μ_0 is the vacuum permeability of free space. In practice, most dielectrics have nearly zero magnetic response, so $\mathbf{M} = 0$ and $\mu_0 = \mu$ is a valid assumption. Nevertheless, for the sake of generality it is treated as a material-dependent parameter.

3. The material is homogeneous and isotropic.

4. Charge is conserved. $\mathbf{J} = \sigma \mathbf{E}$ (Ohm's law), where σ is the conductivity and

$$\frac{\partial \rho}{\partial t} \quad (2.14)$$

2.1.1 The Wave Equation

In the case of no charge or current densities, $\rho = 0$ and the propagation of disturbances in the electromagnetic field can be derived as plane wave solutions to Maxwell's equations. Beginning with Faraday's law

$$\nabla \times \mathbf{E} = -\frac{\partial \mathbf{B}}{\partial t} \quad (2.15)$$

and taking the curl of both sides

$$\nabla \times (\nabla \times \mathbf{E}) = \nabla \times \left(-\frac{\partial \mathbf{B}}{\partial t} \right) \quad (2.16)$$

$$= -\frac{\partial}{\partial t} (\nabla \times \mathbf{B}). \quad (2.17)$$

The left-hand side can be expanded and simplified using the vector identity

$$\nabla \times (\nabla \times \mathbf{A}) = \nabla (\nabla \cdot \mathbf{A}) - \nabla^2 \mathbf{A} \quad (2.18)$$

such that

$$\nabla (\nabla \cdot \mathbf{E}) - \nabla^2 \mathbf{E} = -\mu \frac{\partial}{\partial t} (\nabla \times \mathbf{H}) \quad (2.19)$$

$$-\nabla^2 \mathbf{E} = -\mu \frac{\partial}{\partial t} \left(\frac{\partial \mathbf{D}}{\partial t} + \mathbf{J} \right) \quad (2.20)$$

$$-\nabla^2 \mathbf{E} = -\mu \frac{\partial^2 \mathbf{D}}{\partial t^2} - \mu \frac{\partial \mathbf{J}}{\partial t} \quad (2.21)$$

$$\nabla^2 \mathbf{E} - \mu \epsilon \frac{\partial^2 \mathbf{E}}{\partial t^2} - \mu \sigma \frac{\partial \mathbf{E}}{\partial t} = \mathbf{0}. \quad (2.22)$$

Equation 2.22 is the electromagnetic wave equation in terms of the electric field. Given that excitation of SPPs in this work is accomplished using laser beams, the technique of separation of variables using a plane wave ansatz is used to solve Equation 2.22, resulting in

$$\mathbf{E}(\mathbf{r}, t) = \mathbf{E}_0 e^{i(\mathbf{k} \cdot \mathbf{r} - \omega t)}, \quad (2.23)$$

where

$$\mathbf{k}^2 = \mu\epsilon\omega^2 + i\mu\epsilon\omega = \omega^2\mu \left(\epsilon + i\frac{\sigma}{\omega} \right) \quad (2.24)$$

and $k = \omega/c = \omega\sqrt{\epsilon\mu}$. In Equation 2.23, \mathbf{k} is the material-specific vectorial wavenumber, \mathbf{r} is the spatial position, ω is angular frequency, t is the dimension of time, and c is the speed of light. The initial value is chosen with the vectorial constant \mathbf{E}_0 . The magnetic field follows the same form,

$$\mathbf{H}(\mathbf{r}, t) = \mathbf{H}_0 e^{i(\mathbf{k} \cdot \mathbf{r} - \omega t)}. \quad (2.25)$$

2.1.2 Complex Permittivity

In the derivation of the plane wave solutions to Maxwell's equations, Equations 2.23 and 2.25, the frequency-dependent permittivity is a complex parameter

$$\epsilon(\omega) = \epsilon' + i\frac{\sigma}{\omega} \quad (2.26)$$

$$= \epsilon' + i\epsilon''. \quad (2.27)$$

Physically, ϵ represents both the polarizability in Equations 2.5 and 2.6 and the phase delay δ between the scalar D_0 and E_0

$$\epsilon(\omega) = \frac{D_0}{E_0} |\epsilon| e^{i\delta}. \quad (2.28)$$

Equations 2.27 and 2.28 are consistent with a complex refractive index $\tilde{n} = n(1 + i\kappa) = \sqrt{\epsilon}$.

There are several models [6] from which the frequency-dependent complex permittivity for metals can be obtained. As such, it is relevant to be able to convert from one model to another. Theoretically, the most general expression simply describes $\epsilon(\omega)$ as a superposition of Lorentzian resonances plus a DC term,

$$\epsilon(\omega) = \epsilon_\infty + \sum_n \frac{\sigma_n \omega_n^2}{\omega_n^2 - \omega^2 - i\omega\Gamma_n}. \quad (2.29)$$

In Equation 2.29 ϵ_∞ is the low frequency dielectric response, describing the material's response to a static (DC) electric field, ω_n and Γ_n are material constants, and σ_n specifies the strength of the n th resonance. Equation 2.29 is dimensionless ($c = \hbar = 1$), and is usually encountered when working with numerical simulations of electromagnetic fields [43].

In most other areas, the Lorentz-Drude model is used. Formally, the Lorentz-Drude model is given by

$$\epsilon_{LD}(\omega) = \epsilon_D(\omega) + \epsilon_L(\omega), \quad (2.30)$$

where ϵ_D is contribution from the Drude model, representing free electron effects

$$\epsilon_D(\omega) = 1 - \frac{\sqrt{f_0} \omega_p'^2}{\omega(\omega - i\Gamma'_0)}, \quad (2.31)$$

and ϵ_L is the Lorentz contribution, representing the bound electron effects,

$$\epsilon_L(\omega) = \sum_{j=0}^k \frac{f_j \omega_p'^2}{\omega_j'^2 - \omega^2 + i\omega\Gamma'_j}. \quad (2.32)$$

In Equation 2.32, ω_p' is the plasma frequency of an electron gas. The third and perhaps more accurate [44] model is the Brendel-Bormann model, based instead on an infinite superposition of oscillators

$$\epsilon_{BB}(\omega) = \frac{1}{\sqrt{2\pi}\sigma_n} \int_{-\infty}^{\infty} \exp\left(-\frac{(x - \omega_n')}{2\sigma_n^2}\right) \frac{f_j \omega_p'^2}{(x^2 - \omega^2) + i\omega\Gamma'_n} dx. \quad (2.33)$$

Converting between Equation 2.29 and Equations 2.31, 2.32, and 2.33 is accomplished through the substitutions $\sigma_n = f_n \omega_p'^2 / \omega_n^2$, $\epsilon_\infty = 1$ and Γ'_n . To prevent numerical instability, in computer codes ω_0 , the DC term, should be a very small but nonzero value, e.g. $\omega_1 = 1 \times 10^{-20}$.

The Drude model considers only free electrons and thus has only a single pole in its expression, limiting its accuracy. The agreement with experiment is particularly bad for metals such as gold and silver [45] [44], with deviations of approximately 50% in the real part and 150% in the imaginary up to 650 μm . At higher frequencies the Drude model continues to diverge and is not applicable. Furthermore, the higher error in the imaginary part of ϵ gives narrower SPR resonances than are experimentally observed [44]. The simulations in this work all use the Lorentz-Drude model which falls within 5% of experimentally determined permittivities in the visible spectrum. A comparison between the models and experiment is shown in Figure A.2 of Section A.3.

2.2 SPPs at a Metal-Dielectric Interface

From the plane wave ansatz to Maxwell's equations, the derivation for the existence of surface plasmon polaritons proceeds by imposing boundary conditions consistent with a single interface. Since SPP modes are not supported with TE polarization, it is convenient to restrict the problem to TM polarization in two dimensions. Consider the geometry in Figure 2.1. If a TM wave is incident at an angle on the D_1 - D_2 interface, $\mathbf{k} = (k_x, 0, k_z)$, $\mathbf{r} \cdot \mathbf{k} = k_x x + k_z z$ and $\mathbf{E}_0 = (E_x, 0, E_z)$. The electric field is then

$$\mathbf{E}(\mathbf{r}, t) = \mathbf{E}_0 e^{i(\mathbf{k} \cdot \mathbf{r} - \omega t)} \quad (2.34)$$

$$\mathbf{E}(x, z, t) = \begin{pmatrix} E_x \\ 0 \\ E_z \end{pmatrix} e^{i(k_{x,i}x + k_{z,i}z - \omega t)}. \quad (2.35)$$

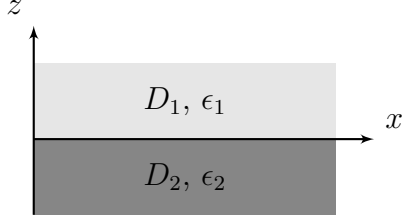


Figure 2.1: Geometry and coordinate system for a single interface which can support SPPs. Domain D_1 has permittivity ϵ_1 , typically a dielectric, and domain D_2 a permittivity ϵ_2 , typically a conductive metal.

Similarly, for the magnetic field,

$$\mathbf{H}(\mathbf{r}, t) = \mathbf{H}_0 e^{i(\mathbf{k} \cdot \mathbf{r} - \omega t)} \quad (2.36)$$

$$\mathbf{H}(x, z, t) = \begin{pmatrix} 0 \\ H_y \\ 0 \end{pmatrix} e^{i(k_{x,i}x + k_{z,i}z - \omega t)}. \quad (2.37)$$

At the interface between D_1 and D_2 there are two values for the permittivity, ϵ_1 and ϵ_2 . Consequently there are two sets of plane wave solutions,

$$\left. \begin{aligned} \mathbf{H}_1(x, z, t) &= \begin{pmatrix} 0 \\ H_{y,1} \\ 0 \end{pmatrix} e^{i(k_{x,1}x + k_{z,1}z - \omega t)} \\ \mathbf{E}_1(x, z, t) &= \begin{pmatrix} E_{x,1} \\ 0 \\ E_{z,1} \end{pmatrix} e^{i(k_{x,1}x + k_{z,1}z - \omega t)} \end{aligned} \right\} D_1 \quad (2.38)$$

$$\left. \begin{aligned} \mathbf{H}_2(x, z, t) &= \begin{pmatrix} 0 \\ H_{y,2} \\ 0 \end{pmatrix} e^{i(k_{x,2}x + k_{z,2}z - \omega t)} \\ \mathbf{E}_2(x, z, t) &= \begin{pmatrix} E_{x,2} \\ 0 \\ E_{z,2} \end{pmatrix} e^{i(k_{x,2}x + k_{z,2}z - \omega t)} \end{aligned} \right\} D_2, \quad (2.39)$$

where the subscript designates which material the wave equation refers to, e.g. \mathbf{E}_1 is the electric field in D_1 , \mathbf{H}_2 the magnetic field in D_2 , etc. Continuity at the boundary requires

$$E_{x,2} = E_{x,1} \quad (2.40)$$

$$H_{y,2} = H_{y,1} \quad (2.41)$$

$$\epsilon_2 E_{z,2} = \epsilon_1 E_{z,1}. \quad (2.42)$$

Applying Ampere's law (Equation 2.4) to the field on each boundary and relating the vector components gives

$$-ik_{z,i}H_{y,i} = -i\omega\epsilon_iE_{x,i} \quad (2.43)$$

$$k_{z,1}H_{y,1} = \omega\epsilon_1E_{x,1} \quad (2.44)$$

$$k_{z,2}H_{y,2} = \omega\epsilon_2E_{x,2}. \quad (2.45)$$

Since $E_{x,i}$ and $H_{y,i}$ are continuous, by substitution of $E_{x,i}$, Equation 2.45 becomes

$$\frac{k_{z,1}}{\epsilon_1} H_{y,1} = \frac{k_{z,2}}{\epsilon_2} H_{y,2} \quad (2.46)$$

$$\frac{k_{z,1}}{\epsilon_1} = \frac{k_{z,2}}{\epsilon_2}. \quad (2.47)$$

Equation 2.47 is the surface plasmon resonance condition for a single interface. Note an important aspect of Equation 2.47: due to the way the geometry was defined (Figure 2.1), $k_{z,1}$ must be positive and $k_{z,2}$ negative to avoid unphysical diverging solutions. For Equation 2.47 to hold, this implies the real part of ϵ_1 and ϵ_2 are opposite in sign. For natural materials, Equation 2.47 is fulfilled if ϵ_1 is a dielectric and ϵ_2 is a metal.

2.2.1 Dispersion Relation

Equation 2.47 can be solved analytically to find the SPP dispersion relation $k_x(\omega)$. First, in terms of its vector components, the following holds in general for electromagnetic waves with $k_y = 0$,

$$\mathbf{k}^2 = \epsilon_i \left(\frac{\omega}{c} \right)^2 = k_x^2 + k_{z,i}^2 \quad (2.48)$$

$$\epsilon_i k_0^2 = k_x^2 + k_{z,i}^2, \quad (2.49)$$

where i is the medium index. Substitution of Equation 2.47 with the relation $k_{x,1} = k_{x,2}$ into Equation 2.49 allows k_x and $k_{z,i}$ to be rewritten as

$$k_x = k_0 \sqrt{\frac{\epsilon_1 \epsilon_2}{\epsilon_1 + \epsilon_2}} = \frac{\omega}{c} \sqrt{\frac{\epsilon_1 \epsilon_2}{\epsilon_1 + \epsilon_2}} \quad (2.50)$$

$$k_{z,i} = k_0 \frac{\epsilon_i}{\sqrt{\epsilon_1 + \epsilon_2}} = \frac{\omega}{c} \frac{\epsilon_i}{\sqrt{\epsilon_1 + \epsilon_2}}. \quad (2.51)$$

where ϵ_i is always assumed to be a function of ω , $\epsilon_i \equiv \epsilon_i(\omega)$. The dispersion relation, Equation 2.49, plotted in Figure 2.2, is useful because it describes the condition under which the momentum of the incident light is matched to an SPP at a particular frequency. For a photon in a dielectric, the “light line” is defined as $\omega = ck/\sqrt{\epsilon_i}$ for $i = 1, 2$. The SPP dispersion relation, Equation 2.49, always lies below the light line, asymptotically $\omega_p/\sqrt{1 + \epsilon_i}$ as $k_x \rightarrow \infty$. However, if light is incident from a dielectric ϵ_1 at an angle θ , the slope of $\omega(k_x)$ is modified to $ck \sin \theta / \sqrt{\epsilon_1}$ and the momentum of light can be matched to excite SPPs. The momentum matching property of light incident from a dielectric at an angle was the principle exploited by Kretschmann [18] to excite SPPs with prisms, known as the Kretschmann Attenuated Total Reflection (ATR) configuration. There exist a multitude of different excitation strategies beyond ATR, however in this work only ATR will be considered. The restriction to ATR is guided primarily by ease of fabrication with facilities on hand (a sputtering machine and a metal target, see Chapter 3).

There are several regions of interest in Figure 2.2, depending on the relative value of ϵ_1 and ϵ_2 . It is first assumed that ϵ_1 is a dielectric with $\epsilon_1 \in \mathbb{R}$ and that $\epsilon_1 > 0$, an

assumption true for most if not all glasses. In this case, for $\Re(\epsilon_2) > 0$, both k_x and k_z are real and the mode is radiative: an SPP mode is supported normal to the interface but it is not bound. For $-\epsilon_1 < \Re(\epsilon_2) < 0$, k_z is real and k_x imaginary, resulting in a quasi-bound mode where the SPP is not confined to the interface and decays evanescently. However, for $\Re(\epsilon_2) < -\epsilon_1$, k_x is real and k_z is imaginary, resulting in a bound mode. In the bound mode, the SPP is localized at the interface in z while having a propagating solution in x and is precisely the condition which must be matched to excite SPPs.

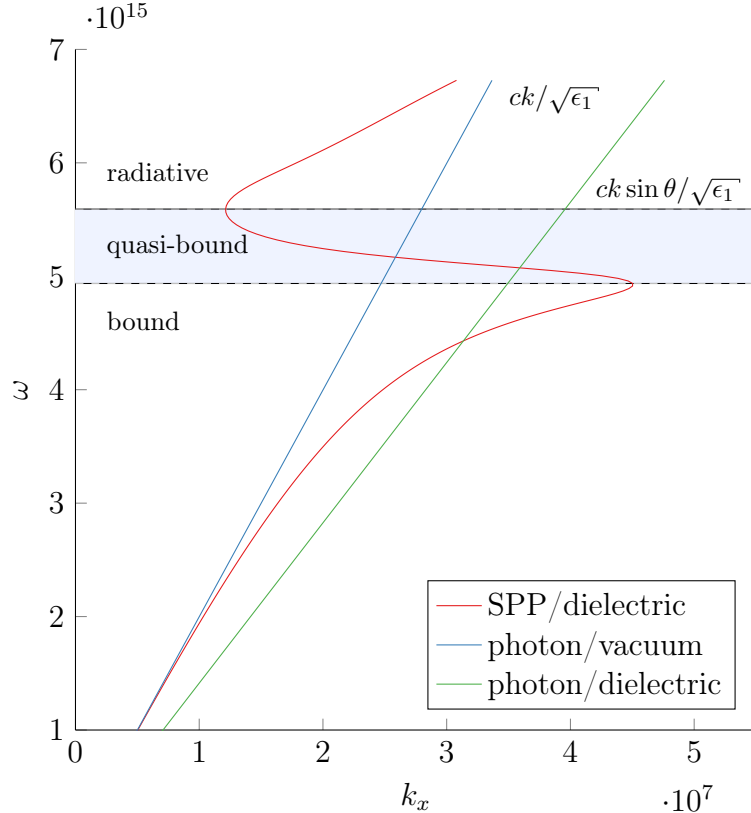


Figure 2.2: Dispersion relation for photons and plasmons for a single interface consisting of a dielectric ϵ_1 , fused silica, and a metal ϵ_2 , gold using the Lorentz-Drude model, also in Figure A.2. Conditions under which SPPs are excited are at the intersection between the photon line in a dielectric and corresponding SPP line.

2.3 Multilayer Systems

The single metal-dielectric interface is the principle under which most laboratory and commercial SPR biosensors operate. Apart from this, certain multilayer interface geometries, such as the one shown in Figure 2.3, have attractive features relevant to the present work. In particular, it will be shown that multilayer interface geometries support SPP propagation lengths more than an order of magnitude greater than the single-layer interface. For example, symmetric multilayer interface with 10 nm gold layers at 632.8 nm see enhancements of 10-60, with propagation lengths up to 250 μm [46] [47].

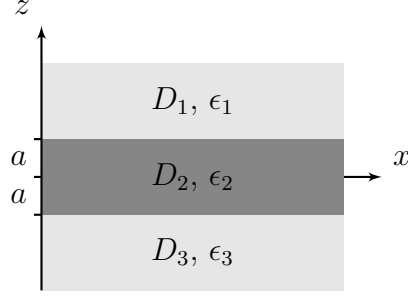


Figure 2.3: Geometry and coordinate system for the multilayer system.

For layers D_1 and D_3 , the equations are the same as for the single-layer system

$$\left. \begin{aligned} \mathbf{H}_1(x, z, t) &= \begin{pmatrix} 0 \\ H_{y,1} \\ 0 \end{pmatrix} e^{i(k_{x,1}x + k_{z,1}z - \omega t)} \\ \mathbf{E}_1(x, z, t) &= \begin{pmatrix} E_{x,1} \\ 0 \\ E_{z,1} \end{pmatrix} e^{i(k_{x,1}x + k_{z,1}z - \omega t)} \end{aligned} \right\} D_1 \quad (2.52)$$

$$\left. \begin{aligned} \mathbf{H}_3(x, z, t) &= \begin{pmatrix} 0 \\ H_{y,3} \\ 0 \end{pmatrix} e^{i(k_{x,3}x + k_{z,3}z - \omega t)} \\ \mathbf{E}_3(x, z, t) &= \begin{pmatrix} E_{x,3} \\ 0 \\ E_{z,3} \end{pmatrix} e^{i(k_{x,3}x + k_{z,3}z - \omega t)} \end{aligned} \right\} D_3. \quad (2.53)$$

If the half-thickness of D_2 , a , is sufficiently small, D_2 will act as a waveguide for SPPs. In D_2 there are two interfaces, the D_2 - D_1 interface at $+a$ and the D_2 - D_3 interface at $-a$, leading to

$$\mathbf{H}_2(x, z, t) = \begin{pmatrix} 0 \\ H_{y,2}^+ \\ 0 \end{pmatrix} e^{i(k_{x,2}x + k_{z,2}z - \omega t)} + \begin{pmatrix} 0 \\ H_{y,2}^- \\ 0 \end{pmatrix} e^{i(k_{x,2}x - k_{z,2}z - \omega t)} \quad (2.54)$$

$$\mathbf{E}_2(x, z, t) = \begin{pmatrix} iE_{x,2}^+ \\ 0 \\ E_{z,2}^+ \end{pmatrix} e^{i(k_{x,2}x + k_{z,2}z - \omega t)} + \begin{pmatrix} iE_{x,2}^- \\ 0 \\ E_{z,2}^- \end{pmatrix} e^{i(k_{x,2}x - k_{z,2}z - \omega t)}. \quad (2.55)$$

Taking Equations 2.54 and 2.55 and applying continuity of H_y and E_x at the boundaries, the dispersion relation is expressed as

$$e^{-4ik_{x,1}a} = \frac{k_{x,1}/\epsilon_1 + k_{x,2}/\epsilon_2}{k_{x,1}/\epsilon_1 - k_{x,2}/\epsilon_2} \frac{k_{x,1}/\epsilon_1 + k_{x,3}/\epsilon_3}{k_{x,1}/\epsilon_1 - k_{x,3}/\epsilon_3}. \quad (2.56)$$

Equation 2.56 is transcendental, but it can still be visualized by plotting the difference between the left-hand side (LHS) and right-hand side (RHS) of the equation, $\log(\Re(|\text{RHS} - \text{LHS}|))$. The result is plotted in Figure 2.4, with the negative values representing regions where SPP modes are supported.

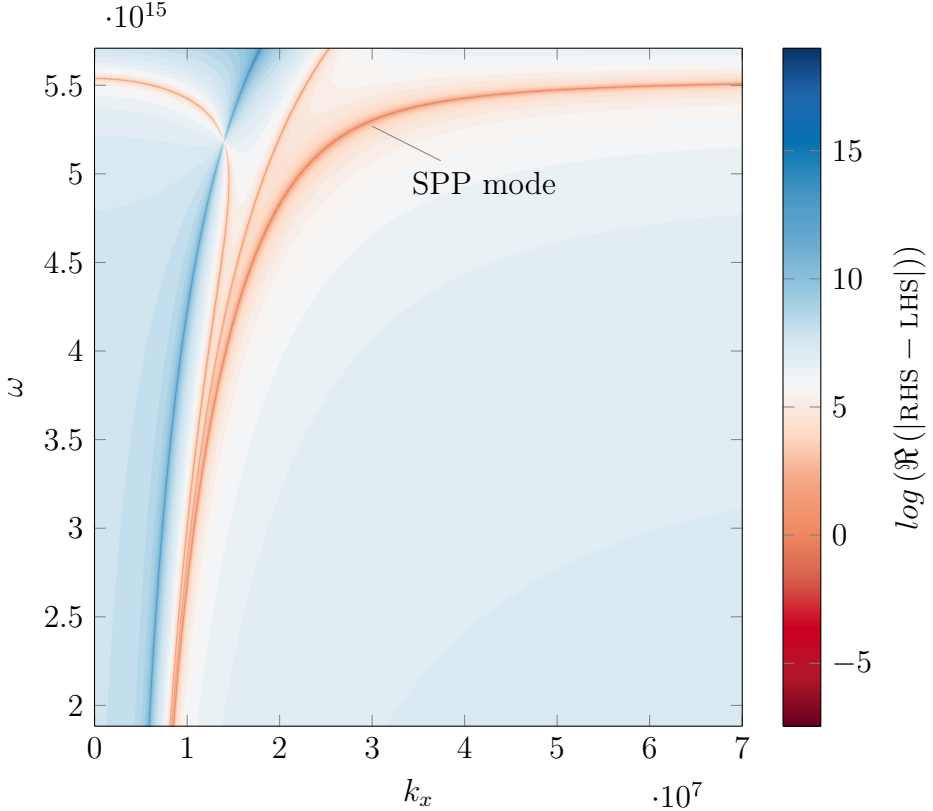


Figure 2.4: Dispersion relation for the multilayer interface system, shown as the difference between the right-hand side (RHS) and left-hand side (LHS) of Equation 2.56. SPP excitation occurs in the red areas. This specific system is also used in the experiment. Plot is for a three-layer interface system with $\epsilon_1 = 1.331$, ϵ_2 Au using the frequency-dependent Lorentz-Drude model, $\epsilon_3 = 1.332$, and the thickness of D_2 is 15 nm.

2.3.1 Photonic Crystal Structures

The layer systems in Figures 2.1 and 2.3 are the most popular layer configurations for SPR biosensing. There is however a very intriguing geometry based on a multilayer stack with which one can obtain SPP propagation lengths in the *millimeter* range. A typical three-layer system in the Kretschmann ATR configuration will exhibit SPP propagation lengths on the order of 8 μm for gold. The symmetric configuration has been experimentally reported to increase the propagation length by a factor of 10-60 [46] [47], and the photonic crystal structure has been reported to further increase the propagation length by a factor of 100 [48].

Currently, much of the work on photonic crystal structures is being carried out by KONOPSKY [49] [48]. The working principle is akin to a Bragg mirror; a one-dimensional stack of layers with varying refractive index is built-up on the surface of a prism, ultimately depositing a metal as the final layer. The multilayer stack works to minimize the tangential component of the electric field in the metal, reducing SPP attenuation. Reduction of SPP attenuation has several advantages to ATR configurations; specifically, it is possible to use lossy metals with more interesting surface chemistries (Pd and Pt), and it becomes

possible to study long-range surface plasmons with near field probes, which the liquid phase would otherwise make difficult.

2.4 Fresnel Relations

Having shown the existence of SPPs under the momentum-matching conditions of Equations 2.47 and 2.56, it is now relevant to predict how SPP excitation would manifest in a physical experiment. To do this, the Fresnel equations are used to calculate the coupling conditions and properties of the excited field and the profiles of the reflected, transmitted, and scattered optical fields.

2.4.1 Prism Coupled Excitation

According to the dispersion relation, Equation 2.49, SPPs are excited on a metal-dielectric interface if an optical field is incident at an angle $ck/\sqrt{\epsilon} \rightarrow ck \sin \theta/\sqrt{\epsilon}$. Furthermore, the following conditions must also be true:

1. SPPs are excited with evanescent waves. The incident light must be at an angle greater than the critical angle, i.e. $\theta > \arcsin(n_1/n_2)$.
2. The metal layer must
 - (a) be thin enough to be at least partially optically transparent at the excitation wavelength
 - (b) have small enough damping, set by its permittivity, such that SPPs can propagate

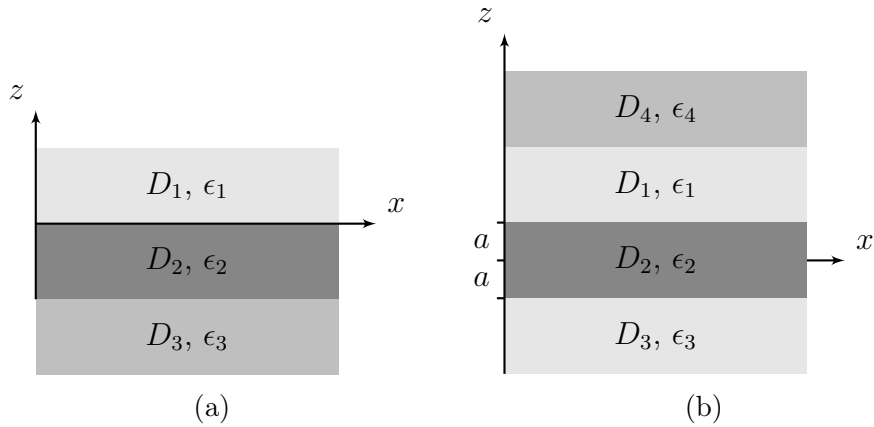


Figure 2.5: Prism coupled excitation of SPPs in the Kretschmann configuration, (a), a three-layer interface system, and (b), a four-layer interface system.

The above conditions are satisfied when using the Kretschmann ATR configuration to excite SPPs. In the Kretschmann ATR configuration, light incident at an angle from a dielectric prism is totally reflected from a surface with the aforementioned multilayer

structure. The incident angle is tuned such that the momentum of evanescent light on the surface matches that of an SPP, i.e. the intersection of the SPP and light line for a dielectric in Figure 2.2.

The Kretschmann ATR configuration is perhaps the most popular amongst many different strategies capable of exciting SPPs. Apart from ATR, the next most commonly encountered strategy matches the SPP momentum using diffractive gratings [7], though the grating coupler's refractive index sensitivity is not as high as ATR [50].

Consider the single interface system, first shown in Figure 2.1. The single interface system is modified into a two interface, three-layer system by adding another layer, D_3 , as shown in Figure 2.5(a). In the three-layer system, light is incident from the bulk media D_1 where $\epsilon_1 > \epsilon_3$, both satisfying $\epsilon'_1 > \epsilon'_3 > 1$ as per the first constraint. D_2 is a metal. Since the real part of the metal permittivity, ϵ'_2 , is a measure of its ability to store energy, and the imaginary part, ϵ''_2 , is a measure of its dissipation, a metal is desired for D_2 with a large negative real part and a small imaginary part.

metal	ϵ'	ϵ''
Ag	-16.065	1.185
Al	-55.075	22.226
Au	-11.361	1.923
Cu	-14.186	2.334
Cr	-6.045	31.219
Ni	-10.164	15.878
W	5.670	21.508
Ti	-5.859	13.680
Be	1.618	22.035
Pd	-15.153	16.245
Pt	-12.778	20.673

Table 2.1: Complex permittivity for select metals at $\lambda = 660\text{ nm}$ calculated using the Lorentz-Drude model. Model parameters are from Refs. [5] and [6].

Table 2.1 shows the complex permittivity for several metals at $\lambda = 660\text{ nm}$, from which it is straightforward to select an appropriate metal: silver, gold, or copper, with silver having the smallest value for ϵ'' . Since ϵ'' is related to energy lost in the medium, a small value suggests longer SPP propagation lengths (indeed, silver is more electrically conductive than copper which is more electrically conductive than gold). From these three gold is chosen and the parameter space is restricted to this metal. Among the metals listed, gold has the second lowest loss, does not oxidize, and most importantly has the most compatibility with existing biochemical protocols. Furthermore, the Fresnel equations predict for a three-layer interface system, D_2 gold, the thickness must be below 100 nm to maintain transparency. The multilayer system is modified as in Figure 2.5(b), with the prism being a supporting layer D_4 with permittivity ϵ_4 , such that $\epsilon'_4 > \epsilon'_{1,3} > 1$ where $\epsilon_1 = \epsilon_3$ (in practice, $\epsilon_1 \approx \epsilon_3$).

For a fixed incident wavelength of $\lambda_0 = 660\text{ nm}$, layer D_1 $\epsilon_1 = 1.5142$ (BK7), layer

$D_2 \epsilon_2 = -11.361 + 1.923i$ (gold), layer $D_3 \epsilon_3 = 1.33$ (water [51]), and $D_4 \epsilon_4 = 1.33$, simultaneous optimization of the incident angle θ and thicknesses of D_2 and optionally D_4 was carried out using a nonlinear minimization [52] of the Fresnel reflectivity. A minimum in the Fresnel reflectivity is commensurate with optimal coupling of light into SPPs. For the three-layer interface system in Figure 2.5(a), optimal coupling occurs for a D_2 thickness of approximately 50 nm. For the four-layer interface system in Figure 2.5(b), optimal coupling occurs for a D_2 thickness of 16 nm and a D_1 thickness of 1150 nm.

The Fresnel reflectivity for p -polarization in the three- and four-layer interface systems of Figure 2.5 are shown graphically in Figure 2.6 as a function of both excitation wavelength and coupling angle. In particular, note the broad range of conditions for which SPP excitation is possible (though not necessarily optimal), corresponding to regions to the right of the critical angle for total internal reflection with a minimum in $|r_p|^2$.

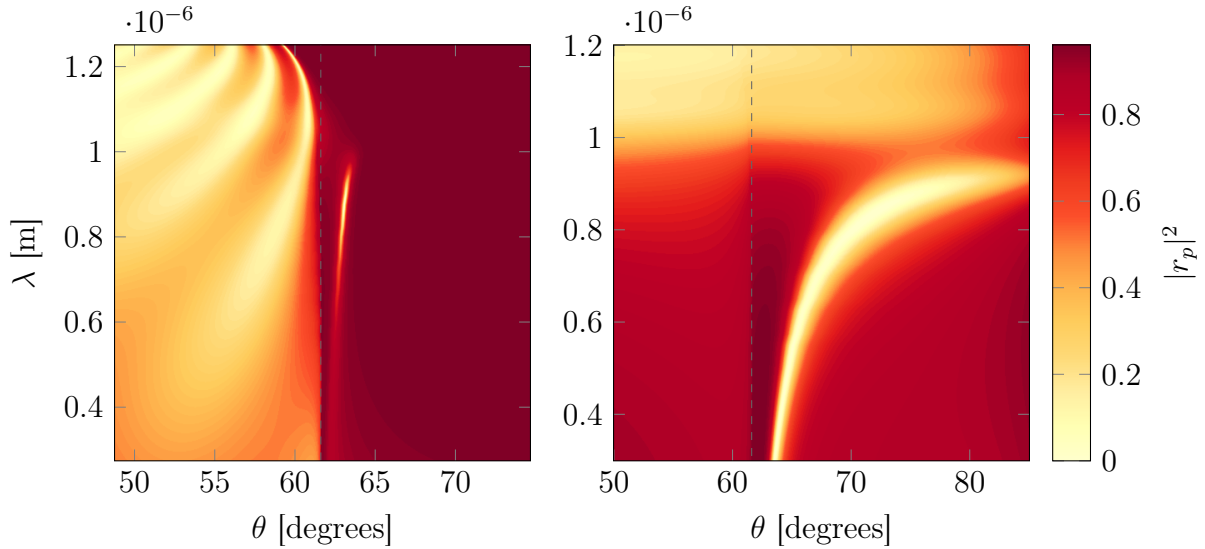


Figure 2.6: Fresnel reflection coefficient for p polarization, $|r_p|^2$, a function of angle and excitation wavelength for conventional (right) and long-range (left) SPP structures in a Kretschmann ATR configuration. Coupling of light into SPPs is possible in regions of low reflectivity to the right of the critical angle for total internal reflection (dashed line).

2.4.2 Near and Far Fields

The Fresnel equations have been used to predict the conditions for optimal SPP excitation, manifest as a minimum in the Fresnel reflectivity for light incident at a particular angle and wavelength for a given layer geometry. In addition to the coupling conditions, the Fresnel equations can also be used to predict the complete near and far optical fields, taking into account effects from SPPs.

Evaluation of the near and far fields is carried out by taking advantage of the shift theorem using the standard Fourier transform recipe,

$$\mathbf{E}(\mathbf{r}) = \int_{-\infty}^{\infty} \tilde{\mathbf{E}}(\mathbf{k}) e^{i\mathbf{k}\cdot\mathbf{r}} e^{i\mathbf{k}\cdot\mathbf{z}'} d\mathbf{k}, \quad (2.57)$$

where $\tilde{\mathbf{E}}(\mathbf{k})$ is the k -space electric field at the surface ($z' = 0$) given by Fresnel equations, taking into account the distribution of the exciting field, and $\exp(i\mathbf{k} \cdot \mathbf{z}')$ is the free-space transfer function along the propagation direction \mathbf{z}' which includes the evanescent wave due to the domain of integration. The mathematical details of the computation are further elaborated in Section 4.1 and Section A.5. Even though the Fresnel equations provide an angular spectrum, the far field is not simply given by multiplying $\tilde{\mathbf{E}}(\mathbf{k})$ by the angular spectrum of the exciting field; a small lateral shift of the beam is introduced in certain cases [28].

The Fourier transform recipe was used to generate plots of the incident, reflected, and near field intensities, shown in Figure 2.7 for the three-layer structure, designated “conventional SPPs”, and in Figure 2.8 for the four-layer structure, designated “long-range SPPs” (LRSPPs). The use of this terminology is motivated by the respective propagation lengths, though physically the SPPs are identical. Figures 2.7 and 2.8 were computed using an excitation wavelength of 660 nm and a Gaussian incident beam of numerical aperture NA = 0.2.

As evidenced from the coupling conditions predicted by the Fresnel equations, the most prominent optical feature of SPP excitation is a minimum, or “notch” in the specularly reflected light at the surface plasmon resonance angle θ_{sp} . The angular location of the minimum is highly sensitive to the refractive index in which the SPP propagates; this is the mechanism most commonly exploited for biosensing. In prism-coupled setups, the notch is always found close to the critical angle for total internal reflection, with sharper resonances being closer than broader ones. Regarding the notch, owing to their greater attenuation, excitation of conventional SPPs displays a relatively broader notch compared with long-range SPPs.

In the near field x - y plots, both Figure 2.7 and Figure 2.8 show a diffraction limited focal spot at the origin, as a small $3 \mu\text{m} \times 5 \mu\text{m}$ ellipse with SPPs propagating along the metal interface at $z = 0$ in the positive x direction. The multilayer structure (LRSPPs) exhibits a propagation length nearly 10 times that of the single layer (conventional SPPs). Such increased propagation lengths aren’t necessarily connected to the system’s inherent bulk refractive index sensitivity, though in practice physical instrumentation provides a better signal with sharper optical resonances compared with broad ones.

2.5 Conically Scattered Light

The notch in the angular intensity of light reflected in the specular direction arises due to interference between the specularly reflected beam and the re-radiated SPP field anti-phase at the excitation angle, θ_{sp} . As most of the incident light is specularly reflected into this direction, the notch is the most obvious spatial signature of surface plasmon resonance in a prism-coupled configuration. Much less obvious, but equally important for the present discussion, is an additional optical feature observable in the same half-space.

As first shown in SPOM experiments with near field probes, during propagation roughness

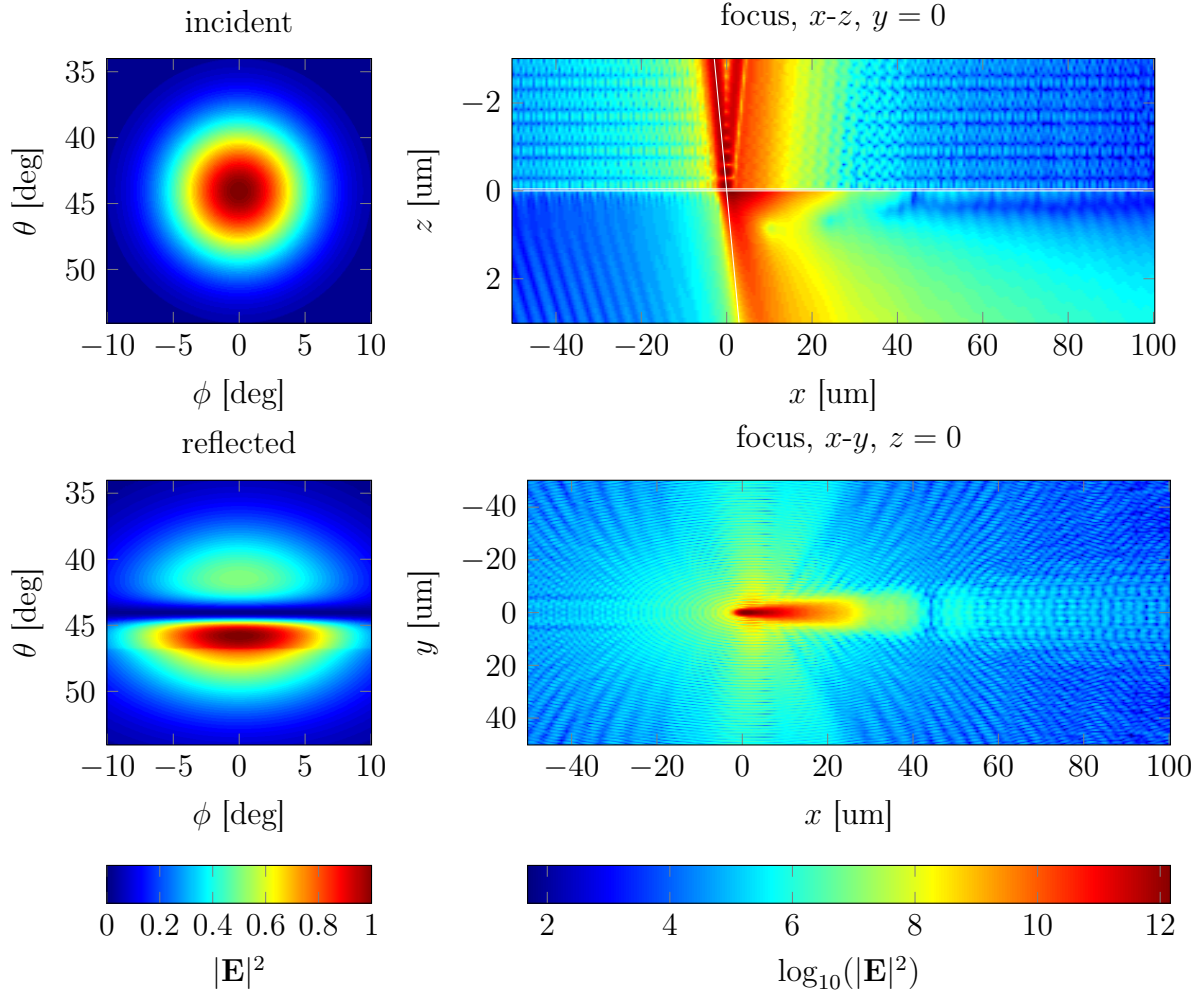


Figure 2.7: Near and far field intensities for excitation of conventional SPPs in a three-layer system. $\lambda_0 = 660 \text{ nm}$, $n_1 = 1.5142$, $n_2 = 0.2843 + 3.3825i$, and $n_3 = 1.3310$. The thickness of the metal layer is 45 nm.

or other surface inhomogeneities can elastically modify the in-plane momentum of an SPP. This phenomena is known as “directional scattering”, the signature of which is a annular “cone” of light at θ_{sp} along an azimuthal coordinate ϕ (Figure 2.9). Though light in the cone is far less intense than in the specular direction, it can be readily observed with the naked eye with a visible laser of only a few milliwatts (e.g. a 5 mW HeNe at 632.8 nm [30]).

The physical process responsible for directionally scattered light begins with the transmission of the incident light at θ_{sp} through the layer structure, evanescently exciting SPPs. This first transmission is identified by the Fresnel *forward* transmission coefficient, t_+^p (e.g. for a three-layer system with layers 0, 1, and 2, $t_+^p \equiv t_{012}^p$). Upon SPP re-radiation as a photon, light will take the transmitted path in reverse, back through the layer structure into the prism, which is identified by the Fresnel *reverse* transmission, t_-^p (e.g. $t_-^p \equiv t_{210}^p$). The intensity in the cone I_{cone} is proportional to the product t_+^p and

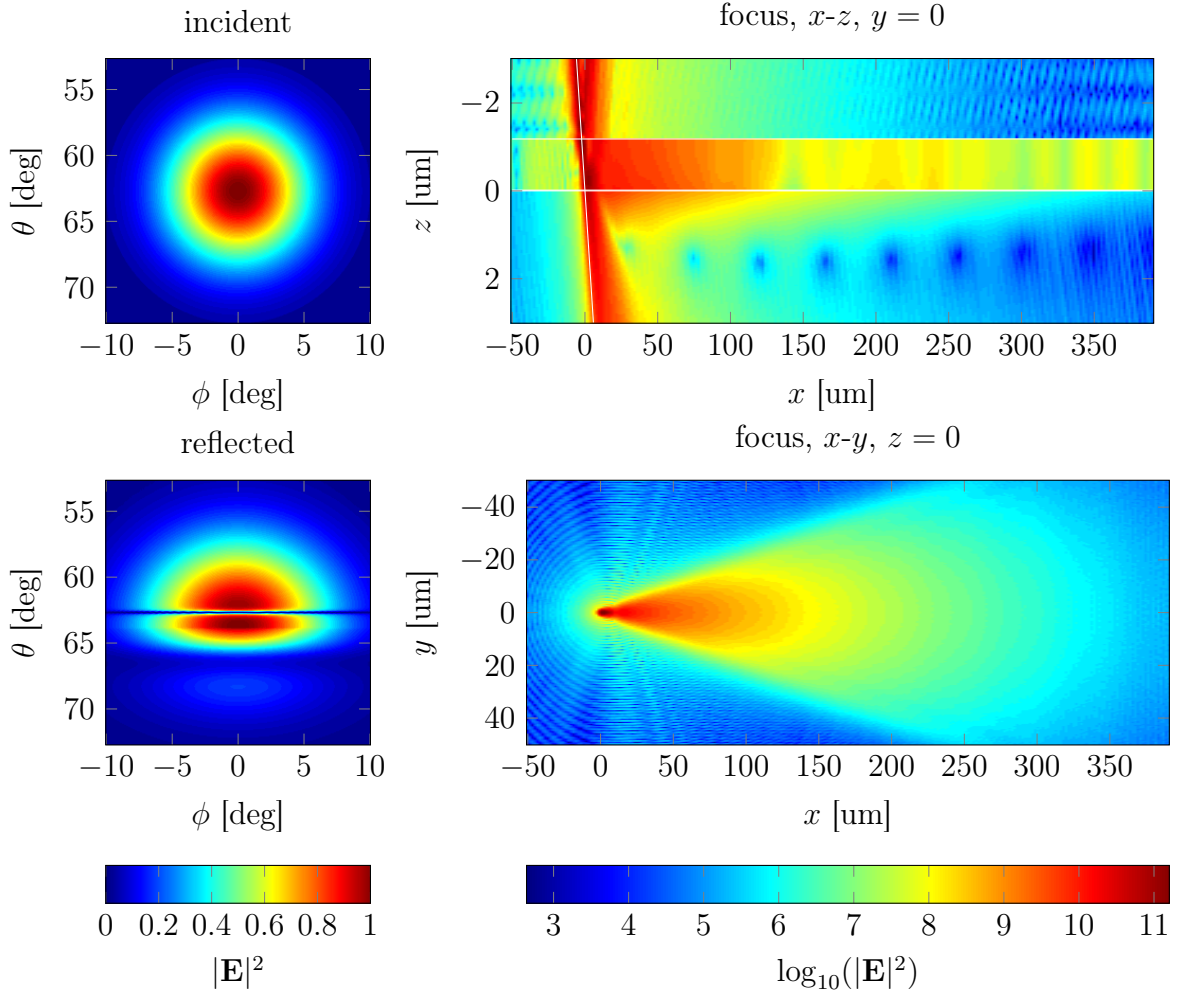


Figure 2.8: Near and far field intensities for excitation long-range SPPs in a symmetric layer system $\lambda_0 = 660\text{ nm}$, $n_1 = 1.5142$, $n_2 = 1.3489$, $n_3 = 0.2843 + 3.3825i$, and $n_4 = 1.3310$. The thickness of the metal layer is 16.97 nm.

t_-^p [22],

$$I_{\text{cone}} = \frac{1}{I_0} \frac{dI}{d\Omega} = 4 \left(\frac{\omega}{c} \right)^4 |t_+^p|^2 |t_-^p|^2 W(\theta_i, \theta_s, \phi) |s(\Delta k)|^2, \quad (2.58)$$

where I_0 is the incident optical power and $dI/d\Omega$ is the scattered power per solid angle. $s(\Delta k)$ is the surface roughness spectrum given by the Fourier transform of the surface autocorrelation function,

$$|s(\Delta k)|^2 = \frac{\sigma^2}{4\pi} \langle S^2 \rangle e^{-(\Delta k^2 \sigma^2)/4}. \quad (2.59)$$

The final term, $W(\theta_i, \theta_s, \phi)$, is a dipole function describing the interference of two roughness-induced currents on the surface [23].

For practical purposes, $W(\theta_i, \theta_s, \phi)$ and $s(\Delta k)$ can be treated as constants if the incident Gaussian beam is within a small angular range [53]. The angular width of the cone is

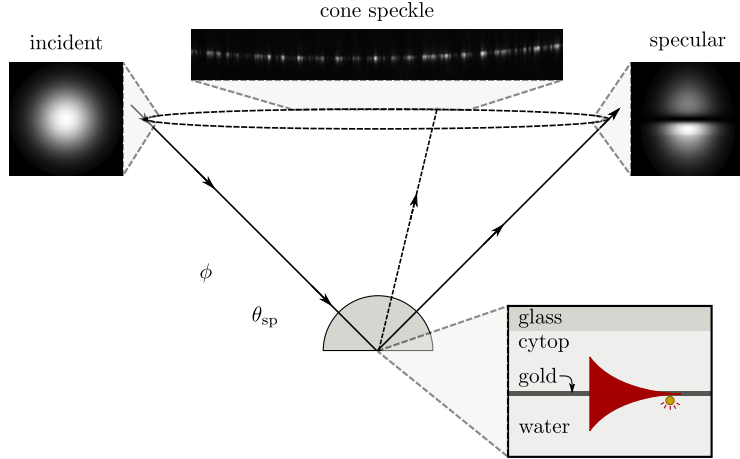


Figure 2.9: Coordinates of the conically scattered light.

approximately

$$\theta_{1/2} = 2k'' \frac{c}{\omega \cos \theta}, \quad (2.60)$$

on the order of 0.2° for LRSPPs and 4° for conventional SPs. In this regard, $W(\theta_i, \theta_s, \phi)$ and $s(\Delta k)$ will be neglected except in a limited scope in Chapter 6, such that

$$|E_{\text{cone}}|^2 \propto |t_+^p|^2 |t_-^p|^2. \quad (2.61)$$

Due to the *double* plasmonic enhancement in Equation 2.58, light in the cone has a smaller angular width than its specular counterpart in the notch, shown in Figure 2.10 for a three-layer system ($n_1 = 1.5142$, $n_2 = 0.2843 + 3.3825i$, $n_3 = 1.331$ and $d_2 = 45 \text{ nm}$). In Figure 2.10, the cone signal has been inverted and normalized to the same range as the notch to facilitate this comparison.

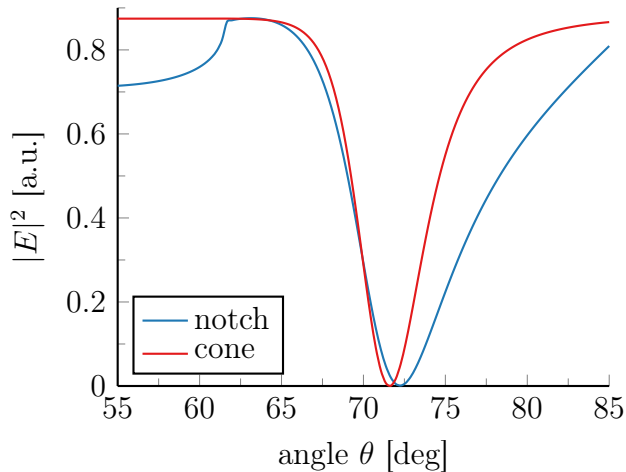


Figure 2.10: Comparison of the angular optical profile of the cone and notch. The cone signal has been inverted and normalized to the same range as the notch for comparison.

The notch is the prime spatial feature of SPR biosensing in prism-coupled setups and, as a result of the significant academic and commercial interest in the field, it is very

well understood. Furthermore, advancements in the engineering and implementation of such devices already achieved shot-noise limited performance [54]. In contrast, very little information is available about the cone apart from a few material-science oriented papers showing the utility of its integrated intensity in SPOM measurements [10], connection with surface roughness [22], and angular polarization distribution [55]. The present work attempts to address this deficiency in the context of biosensing with new investigations into the influence of the spatial intensity distribution in the cone on both changes in bulk refractive index (Section 5.5) as well as perturbations in the underlying scattering microstructure (Chapter 6). In particular, it will be shown that under certain conditions the cone contains optical speckle, which can be used to great utility to sense discrete binding events which perturb the scattering microstructure.

3 | Experimental

3.1 Setup

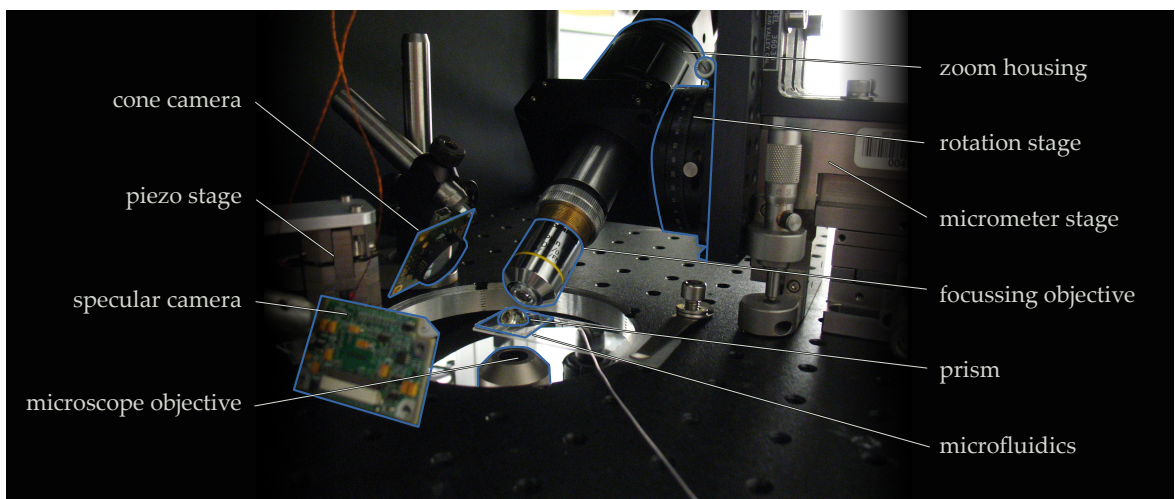


Figure 3.1: Image of the experimental setup with the functional components annotated.

Excitation of surface plasmon polaritions was carried out using a modified Kretschmann attenuated total reflection (ATR) setup configuration, shown annotated in Figure 3.1 and schematically in Figure 3.2. Light from a 50 mW 660 nm diode laser (Ingis 660, Laser Quantum Ltd.) with a bandwidth of 30 GHz is first coupled into a single mode optical fiber via an integrated air-spaced doublet fiber collimator. The fiber guides the laser light to an optical breadboard mounted on an inverted microscope. All primary functions of the experimental setup take place on the breadboard. At the breadboard stage, the Gaussian beam from the single mode fiber is collimated by an output coupler to a beam waist of $w_0 = 5$ mm and proceeds through a polarizing beamsplitter, passing p polarized light. The light is focused by a 10X microscope objective (Olympus plan achromat, NA = 0.25, 10.6 mm working distance) onto the hypotenuse of a hemispherical prism of diameter $d = 10$ mm. The beamsplitter and microscope objective are mounted on a rotation stage which itself is mounted on a micrometer stage. The objective itself is mounted on a zoom housing enabling linear travel along the optical axis, greatly simplifying the task of focussing. When the rotation stage is at the surface plasmon resonance angle, the micrometer z axis is fixed with a near-diffraction limited spot at the center of the prism's hypotenuse. The spot size is modified via the zoom housing, and its transverse location

on the surface by the x and y lead screws on the micrometer stage.

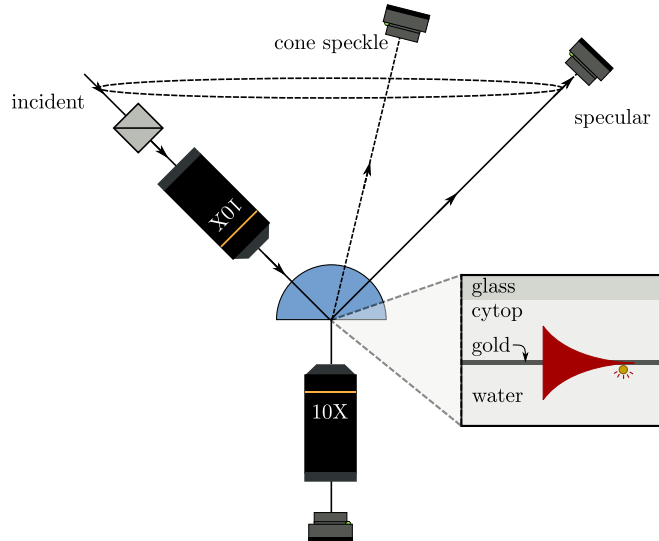


Figure 3.2: Schematic of the experimental setup. Description in text.

The hemispherical prism is mounted on a planar structure supporting either traditional or long-range SPPs. A microfluidic flow cell permitting the introduction of samples is integrated into the setup. Both the microfluidics and the substructure supporting the prism are thin and optically transparent. In this way, the sensing surface may be imaged with the objective on the inverted microscope. The breadboard containing the experiment was fixed to the optical table with its own micrometer stage, permitting translation of the entire experiment in the plane of the optical table, and thus creating a way to position the inverted microscope objective without disturbing the rest of the setup.

The hemispherical prism affords a useful optical feature in the setup. If the focal spot is positioned at the central point of the hemispherical prism's hypotenuse and the focussing optic obeys the sine condition, a minimum amount of aberration will be introduced by the presence of the hemispherical prism. To take advantage of this feature, a microscope objective was chosen to act as the focussing optic. The use of a microscope objective and hemispherical prism is not strictly necessary; previous versions of the experimental setup made use of an $f = 25$ mm aspheric lens for focussing and a 25 mm diameter, $f = 20$ mm aspheric condenser lens as an ersatz hemispherical prism. The aspheric focussing and condenser lens does distort the incident and reflected light precluding a diffraction limited spot, however for the present purposes the performance difference is not important.

Extra attention was not given to mechanical stability. Though the quality of the optomechanical components was acceptable, the mounting of the imaging sensors and the prism extended on its glass slide were less than what would typically be considered optically rigid. Despite this, no effects were observed on the specular or cone sensor which could be attributed to mechanical instability, however the image from the inverted microscope objective exhibited low frequency (< 5 Hz, measured by imaging) displacements coincident with transient events in the laboratory: footsteps, opening and shutting of doors, etc. When present, such artifacts were corrected for in a post-processing step using stabilization functions from the software program Fiji [56].

3.1.1 Imaging Sensor

Three identical IDS USB 2.0 8 bit CMOS sensors with a spatial resolution of 1280×1024 pixels operated in parallel to acquire data. The sensors included a reduced “area of interest” (AOI) capture mode, allowing a subset of the available pixel region to be transmitted via the serial bus to the host computer. Under this mode the cone, specular, and surface images were captured at approximately 100 fps and a minimum of 1280×250 pixels.

To allow the cone sensor to capture the largest angular region of the cone possible, the sensor was removed from its housing and its naked PCB used as a mount support (Figure 3.3). Removing the housing allowed the cone sensor to be positioned approximately 10 mm from the focal spot and to capture an angular region of approximately 37° .

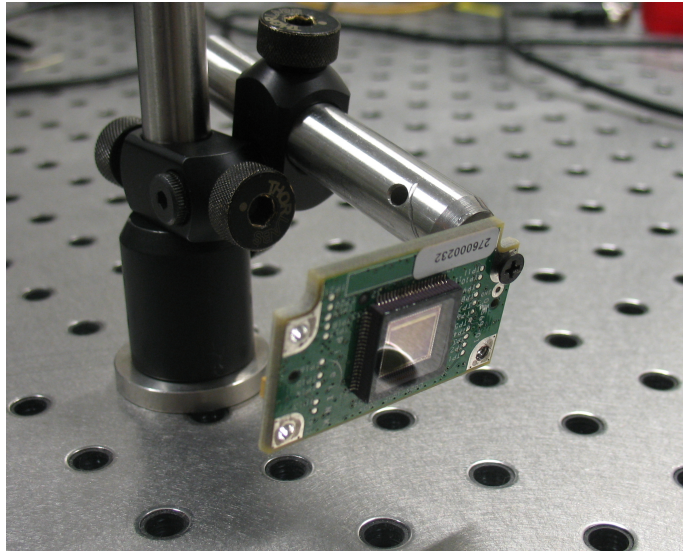


Figure 3.3: The cone sensor, an IDS USB 2.0 8bit CMOS sensor, removed from its housing allowing close positioning with respect to the prism.

A custom software, written in c and utilizing the IDS UEye SDK version 3.82, was used to read the raw sensor data directly from memory and write it to a single binary file on the disk of the host computer. The modifications increased the data acquisition speed significantly compared with the stock software included with the IDS sensors. This was accomplished by first suppressing all calls image or video library calls by removing the need to transcode the pixel data, instead writing raw pixel data directly to disk. Second, the raw pixel data was saved to a single file, eliminating seeking of the computer’s physical disk read/write head during both file creation and updating the disk’s filesystem journal when acquiring data as an image sequence.

On the hardware side, each imaging sensor was given its own dedicated USB bus, maximizing the USB polling frequency and avoiding other bus traffic which would otherwise retard the sensor datastream.

3.2 Sputtering

Metal films were fabricated using a standard top-down plasma sputtering process in Argon at a pressure of 1 mtorr and a mass flow rate of 12 STP. The deposition was 6.60 \AA s^{-1} for gold and 5.88 \AA s^{-1} for silver at 150 and 66 W DC, respectively. During sputtering, the samples were rotated at 50 RPM. Though adhesion of the metal films to both glass and fluoropolymer substrates was poor, instances of in-situ film-substrate separation were rare (observed five times over the course of approximately fifty experiments). It was observed that film-substrate separation was instigated by stresses caused by pressure differentials in the microfluidic flow cell. The majority of such stresses were mitigated by employing a natural siphon effect to flow liquids at low rates through the microfluidic cell in lieu of mechanically forced flow.

The substrate material consisted of a 12 mm diameter BK7 № 1 glass coverslip. Coverslips were cleaned in a hot base bath. A 2 % solution of Hellmanex II was first prepared in a pyrex beaker with a volume of 25 mL and heated to a temperature of 60 °C on a hot plate. The BK7 coverslips were immersed for 300 s. The beaker was then removed from the hot plate and put in a sonicator for 300 s. After sonication, the coverslips were removed from the solution and washed liberally with distilled water and dried under a dry nitrogen stream. Cleaned coverslips were stored individually on top of a small 1 mm^3 piece of PDMS plasma bonded to a microscope coverslip, and prepared batches were kept in a dark box until use. Coverslips sputtered with metal films were always used within one or two days to forestall contamination or possible oxidation in the case of silver films.

For the scattering experiments discussed in Chapters 5 and 6, the substrate was bonded to a hemispherical prism using NOA89 UV-cured optical adhesive. NOA89 is well characterized for optical applications with a high spectral transmission and a refractive index of approximately 1.51 across the visible and near IR. The prism material consisted of either BK7 or NOA89 cast in a hemispherical mould made from BK7 prisms cast in PDMS. Once the BK7 prism was removed from the PDMS, the void was filled with NOA89 and cured under a 15 W UV lamp at a distance of 5 cm for 12 h. To remove bubbles, the UV adhesive was first centrifuged in an opaque microcentrifuge tube at 15 000 RPM for 30 min. As the substrate construction is independent of the prism material and both NOA89 and BK7 have nearly the same refractive index (approximately 1.51 at 660 nm), the two cases are not distinguished except to note that the NOA89 prisms are easier to fabricate in bulk.

For the interference experiments discussed Chapter 4, prisms of either LAH79 or BK7 were used with the metal film sputtered directly onto the prism's hypotenuse. Such glass prisms were prepared by first removing any existing metal film. Silver films were removed by immersion in 70 % HNO_3 for 60 s. Gold films were removed similarly by immersion in freshly prepared aqua regia, composed of a 1:3 ratio of HNO_3 to HCl. The glass prisms were sonicated in acetone to remove any organic contaminants and rinsed in ultra-pure dry acetone with a final cleaning with methanol and lens tissue using the drag and drop method.

3.3 Surface Modifications

The width of the SPR resonance and the structure of speckle in the cone are fundamentally related to the underlying scattering microstructure. In this respect it is important to note that for a perfectly smooth film, SPPs are non-radiative and do not couple with the exciting field [57] [20], and none of the aforementioned physical manifestations of surface plasmon resonance (e.g. the notch and the cone) can be observed. Surface roughness of some degree is therefore required. Fortunately, creation of perfectly smooth films is rather difficult to achieve, and some degree of roughness will almost always be present. In the present case where films are fabricated using plasma sputtering, surface roughness is unavoidable. Notwithstanding, several procedures were investigated to introduce increased amounts of surface roughness, motivated by the desire to better understand the nature of the scattering processes.

3.3.1 Measurement of Surface Roughness

To quantify the amount of surface roughness, polarization measurements were conducted to determine the so-called “rest light intensity” [58] of the system. The rest light intensity is determined by measuring the angular dependence of the *p*- to *s*-polarization components of light emitted from the components of light which is emitted from the *back* of the prism [59] [60]. For surface scattering processes, the angular-dependent ratio is given by [61]

$$\frac{I_p}{I_s} = \frac{\tan^2 \theta}{1 + (\tan^2 \theta)/|\epsilon|} \quad (3.1)$$

and for volume scattering by

$$\frac{I'_p}{I'_s} = \frac{1}{|\epsilon|^2} I_p I_s \quad (3.2)$$

where I_p and I_s are the intensities of *p* and *s* polarized light, respectively.

The incident light and the excited SPPs are strictly *p*-polarized; polarization mixing cannot arise from a first order scattering process. In this way, the degree of polarization mixing measures the degree of higher-order (multiple) scattering.

The volume scattering components in Equation 3.2 are not taken into account, as its value is too low to be determined with the present apparatus, and furthermore it is expected not to be a contributing factor [59]. The increased rest light at $\theta = 0^\circ$ fits the model well, suggestive of increased surface roughness.

Heat Pretreatment

During sputtering, heat applied to the substrate can be used to enhance surface roughness. Following HORSTMANN [58], the hypotenuse of a 25 mm hemispherical BK7 glass prism was used as a substrate and heated in an oven to 300 °C immediately prior to entering

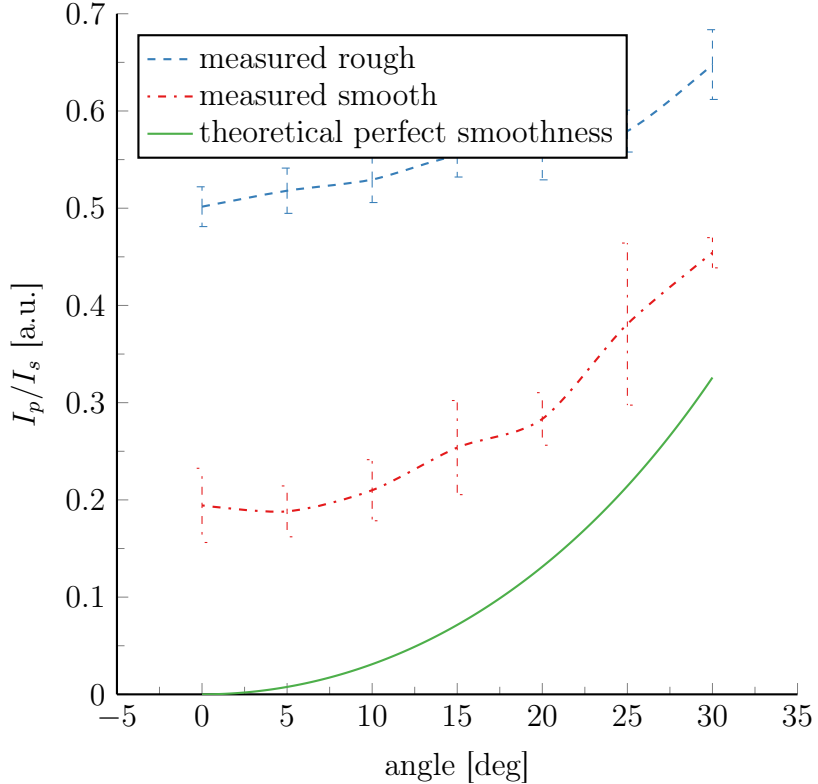


Figure 3.4: Rest light measurements, the ratio of polarization intensities I_p/I_s , comparing an unmodified “smooth” silver film to a “rough” film sputtered using heat pretreatment technique. For comparison, Equation 3.1 shown as an example of theoretical perfect smoothness.

the vacuum chamber for sputtering. After sputtering, the prism was allowed to cool to room temperature.

Figure 3.4 shows rest light intensity measurements conducted for an unmodified silver film, “measured smooth”, and a film roughened with heat pretreatment, “measured rough”, along with the theoretical prediction of Equation 3.1 for a film with no multiple scattering film, ‘theoretical perfect smoothness’. The p- and s-polarization components were measured separately with a polarizing beamsplitter and two cameras whose pixel intensities were integrated to obtain an intensity value. These ersatz photodiodes were positioned on a rotation stage on the bottom halfspace of the hemisphere, and measurements were taken in 5° increments.

The film for which heat pretreatment was applied, “measured rough”, in Figure 3.4, has a much higher I_p/I_s ratio than the film without, “measured smooth”. Comparing these values with those of HORSTMANN and the first order theory of KROGER [62] [58] gives an estimated RMS roughnesses of $\sim 7 \text{ \AA}$ for the unmodified film and $\sim 40 \text{ \AA}$ for the heat pretreatment.

Enhancing the surface roughness through heat pretreatment was also observed to have a deleterious effect on the quality of light on the cone, precluding measurements of optical speckle presented in Chapter 5. As such, this method was not used except as presented

in Figure 3.4. A detailed explanation is given in Section 5.4.

3.4 Nanoparticle Adsorption

The most fruitful technique for surface modification was based on adsorption of spherical gold nanoparticles onto a gold substrate. The presence of a nanoparticle is conceptually similar to the presence of a tip in SPOM experiments (Section 2.5); both function as in-plane scatterers of SPPs. Using nanoparticles this way was observed to carry the additional advantage of preserving the structure of optical speckle in the cone (Section 5.4).

Citrate-capped spherical gold nanoparticles (AuNPs) with diameters in the range of 20 nm to 100 nm were used for the modification. These specific particles were chosen for two reasons: first, gold has a significant amount of established bio-relevant chemistry protocols, and second, the localized surface plasmon resonance of these particles is not coincident with the laser frequency. A UV-Vis spectrum for the particles, shown in Figure 3.5, confirms the second assumption. Though it would be perhaps interesting at some point to look at the effects of matched resonances, it was desired to narrow the range of physical principles in play in order to simplify interpretation of results during the investigation.

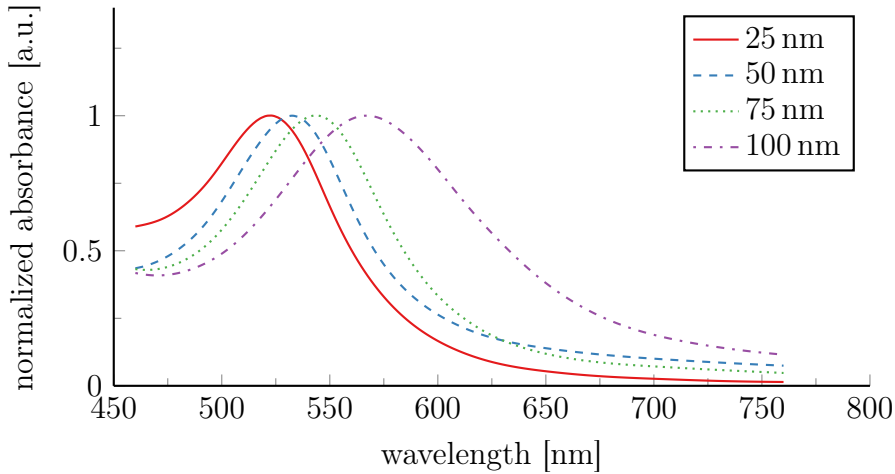


Figure 3.5: UV-Vis absorbance spectrum of 25, 50, 75, and 100 nm spherical gold nanoparticles used in nanoparticle adsorption experiments.

3.5 Cytop

A fluoropolymer, poly(1,1,2,4,4,5,5,6,7,7-decafluoro-3-oxa-1,6-heptadiene), more commonly referred to by its commercial name Cytop, was employed to make multilayer substrates supporting long-range surface plasmons.

At an operating wavelength of 660 nm and at 20 °C, the refractive index of Cytop is very close to water — 1.341 for Cytop [63] versus 1.331 for distilled water [51]. The similar refractive index allows a near-symmetric refractive index profile required for long-range surface plasmons as described in Section 2.4.2.

Cytop was purchased from AGC Chemicals as item number CTX-809A. The last letter “A” in the item number designates it is intended for use on amorphous (glass) applications, and the subsequent number designates the concentration. For example, CTX-809A is 9 % cytop and 91 % solvent, and likewise CTX-803A is 3 % cytop and 97 % solvent. Atachi manufactures another item with an “M” designation designed for metals, but in either case the multilayer structure would have one side in contact with a non-optimal material. Similar to the metal layers described in Section 3.2, the adhesion of the cytop to both metals and glass was poor, as such careful handling combined with a low pressure differentials in the microfluidic stage was employed to prevent separation.

Thin films were made following a spin-coating procedure. A small drop of CTX-809A was placed directly on a clean 12 mm round glass coverslip and the coverslip spun at 3000 RPM for 30 s. Immediately after spinning, the coverslip was removed and placed on a hot plate at 50 °C for 30 min. The temperature of the hot plate was then increased to 200 °C and the Cytop allowed to cure for 12 h to assure all solvents had evaporated. After cooling, the metal films were sputtered directly on the Cytop layer without any further surface modification.

The resultant film thicknesses were determined with a spectrometer by measuring its broadband reflectance at $\theta = 45^\circ$ and using a nonlinear least squares routine [64] to fit the Fresnel intensity reflection coefficient for a single-layer film R [65]

$$R = \frac{n_1^2(n_i - n_s)^2 \cos^2 \delta + (n_i n_s - n_1^2)^2 \sin^2 \delta}{n_1^2(n_i + n_s)^2 \cos^2 \delta + (n_i n_s + n_1^2)^2 \sin^2 \delta} \quad (3.3)$$

where

$$\delta = \frac{2\pi}{\lambda_0} n_i d_i \cos \theta \quad (3.4)$$

and the Cytop layer has a refractive index n_i and thickness d_i , the substrate a refractive index n_s , and the system in the presence of refractive index n_1 (air). Equation 3.3 assumes the reflection coefficient for TE polarization, of which Equation 3.3 has only one free parameter: d_i . The thickness d_i was solved for using a linear least squares fitting algorithm. An example of the raw spectrometer data and its best fit is shown in Figure 3.6.

The surface roughness of the Cytop films was not measured, but the experiments suggest the surface roughness must be very small. The intensity of light scattered into the cone is too low to be observed when exciting SPPs in an unmodified cytop-gold-water setup — additional surface features must be added before the cone becomes visible. In comparison to metal films sputtered directly on BK7 glass substrates with a typical surface roughness of 0.3 nm within 1 μm^2 [66] [67], the cone is always found to be visible.

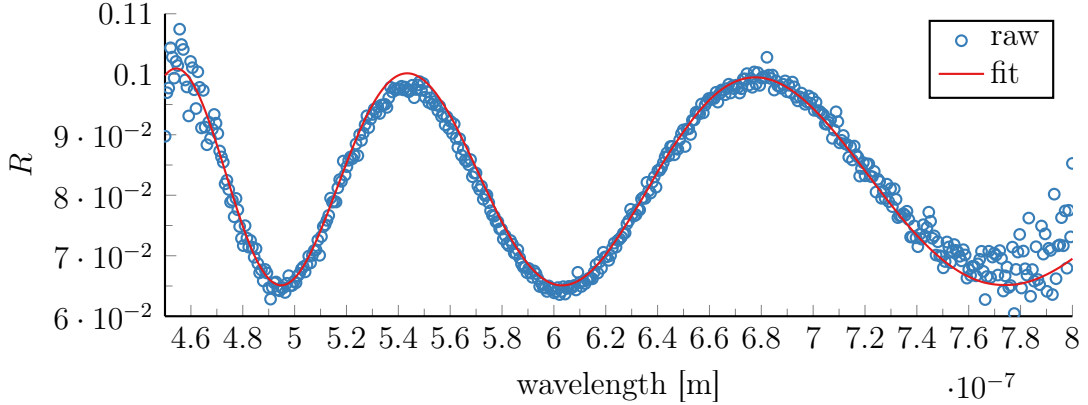


Figure 3.6: Reflectivity of a thin Cytop layer on BK7 at $\theta = 45^\circ$. Shown is the experimental data and the best-fit with Equation 3.3. Calculated layer thickness was 1150 nm.

3.5.1 Spin Coating

During the course of the present experimental work, a standard programmable spin coater was not available. Being a rather expensive piece of equipment, a ersatz spin coater was made using a spinning platter type hard disk drive. Spin coaters built in this fashion have been reported before [68], but herein is described a much simpler and economic implementation using off-the-shelf components.

The cover from all internal components except for the motor are first removed. A solid aluminum plate is affixed to the top of the motor using the existing screw taps. The three leads of the hard disk's three phase motor are connected directly to a programmable electronic speed controller (ESC). The ESC itself is a standard component found in most land and air based radio controlled drones. Once configured, the ESC accepts a pulse width modulated (PWM) input with pulse widths varying from 1000 μs (off) to 2000 μs (full speed). The PWM signal for the ESC is generated by an Arduino Uno platform, based on the Atmel ATMega128 8 bit microcontroller. The Arduino is programmed for several preset spin sequences which are initialized by pressing a button. Finally, a small flange connected to the motor spindle is used in conjunctino with an optical interrupter switch to monitor the spin speed.

The spin speed of the motor was recorded as a function of PWM signal and the relationship fit to a second order polynomial. The fit parameters were then used to set the PWM output given a desired spin speed without feedback.

The stability of the spin coater and the range of speeds it offers is shown in Table 3.1. Perhaps the most obvious downside of the ESC is that it does not operate very well in the low RPM limit, particularly at around 2800 RPM.

The reproducibility of Cytop layers obtained in this way was found to be on average approximately 70 nm across the entire spin speed range. The is greater than the fit error of the Fresnel reflectivity, which was always found to be on the order of or less than 1 nm.

spin speed (RPM)	standard deviation
1269.889	1.140
2107.532	1.865
2812.920	79.321
3471.170	0.880
4075.631	1.714
4598.686	0.878
5152.030	0.455
5683.387	0.892
6176.233	0.733
6691.978	1.617

Table 3.1: Standard deviation of the spin speed at nominal angular speeds for the hard disk spin coater.

3.6 Microfluidics

Microfluidic flow cells made of polydimethylsiloxane (PDMS) were used to introduce analytes into the sensing volume. PDMS is a bio-compatible organosilicon compound obtained as a two part elastomer kit¹. The two part liquid is combined in a 10:1 ratio by mass in a small plastic mixing cup. The correct proportions are determined by an analytical balance to a precision of 0.01 g. They are then combined and mixed using a magnetic stir paddle for 5 min. The mixture is poured onto a polished silicon wafer in a shallow glass dish and evacuated in a vacuum bell jar until all dissolved gas has been removed. The PDMS is then baked for 20 min at 120 °C. Once removed, the cured PDMS is cut free from the mold using a scalpel and transferred to a clean glass slide where it is stored in a dust free environment until use.

The PDMS is cast into 1 mm thick layers which are cut into 25 mm × 25 mm squares. Horizontally embedded and centered in the PDMS layer was a length of 0.6 mm outside diameter silicone tubing. A circular biopsy punch was used to extract a 6 mm hole from the center, which cut the tubing in its center. The hypotenuse of the prism with its complete layer substructure was then placed over the remaining side of the central hole; the surface attraction between the PDMS and the prism substrate was sufficient to prevent leakage. A siphon was set up between the input and output channels in the PDMS and the experiment run with a flow rate of 1.85 $\mu\text{L s}^{-1}$. The microfluidic flow cell as integrated into the experiment is shown schematically in Figure 3.7.

As a cursory note, when handling PDMS or anything PDMS comes into contact with, a clean pair of nitrile gloves should be used. It was observed that surfaces which had been touched with powder-free latex gloves could no longer be directly bonded. The present anecdote seems to be prevalent in the literature, but no description of the underlying mechanism is known.

¹Dow Corning Sylgard®184

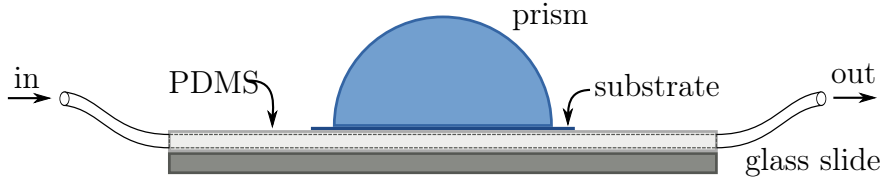


Figure 3.7: Schematic of the microfluidic cell as integrated in the experiment.

3.7 Image Processing

Analysis of the light in the cone requires designation of the spatial coordinates of each pixel in the imaging sensor relative to the scattering spot. This section describes our post-processing technique and determination of sensor coordinates.

3.7.1 Coordinates of the Imaging Sensor

The relative two-dimensional spatial coordinates in the plane of the imaging sensor are known given the size and number of its pixels. The absolute three-dimensional coordinates with respect to the scattering spot are more difficult to assess. The way in which the experiment is constructed makes it difficult to accurately measure the distance between the imaging sensor and the focal spot. However, with knowledge of the angle in which the sensor is tilted, the focal spot-sensor distance can be extracted *a posteriori* from measuring the shape of the light falling on the sensor.

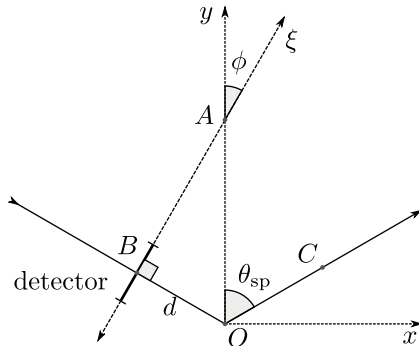


Figure 3.8: Geometry for determining the sensor distance d .

Consider the experimental geometry shown in Figure 3.2. Light from scattered SPPs emanates as a cone and is imaged by a planar sensor. The light pattern on the sensor is by definition a conic section, with the re-radiated SPP light as the cone and the sensor as the cutting plane. Consequently, the shape of the light on the sensor will be either a circle, an ellipse, a parabola, or a hyperbola. In the experimental setup, the sensor is accordingly fixed orthogonal to the SPP cone.

The geometrical situation is depicted in Figure 3.8. SPPs scatter into the far field from point O at an angle θ_{sp} . The detector, which has a finite transverse length, is at B and

is orthogonal to \overline{OB} at an angle $\phi = \pi/2 - \theta_{\text{sp}}$ with respect to the normal vector from the prism surface \overline{OA} . Because $\phi < \theta_{\text{sp}}$ and $\theta_{\text{sp}} > \pi/2$, lines \overline{BA} and \overline{OC} never intersect. The resulting light pattern on the sensor is a hyperbola. It is then relevant to determine, given the parameters of the hyperbolic section, the distance between the focal spot and the sensor, the line \overline{OB} with length d .

The coordinates of the sensor are represented as (ξ, y) , with the following relationships

$$x = \xi \cos \theta_{\text{sp}} \quad (3.5)$$

$$r = (d \sec \theta_{\text{sp}} + \xi \sin \theta_{\text{sp}}) \tan \theta_{\text{sp}} \quad (3.6)$$

and

$$x^2 + y^2 = r^2. \quad (3.7)$$

Note $d \sec \theta_{\text{sp}}$ is the length of \overline{OA} . Equation 3.6 and Equation 3.7 can be combined to obtain

$$\xi^2 (\cos^2 \theta_{\text{sp}} - \sin^2 \theta_{\text{sp}} \tan^2 \theta_{\text{sp}}) + 2\xi d \tan^3 \theta_{\text{sp}} + y^2 = d^2 \tan^2 \theta_{\text{sp}} \sec^2 \theta_{\text{sp}}, \quad (3.8)$$

which, after a bit of algebra, can be solved for ξ , taking the positive root

$$\xi(y) = \frac{4\sqrt{2} \sqrt{-2y^2 \cos 2\theta_{\text{sp}} \cos^6 \theta_{\text{sp}} + d^2 \cos^6 \theta_{\text{sp}} - d^2 \cos 2\theta_{\text{sp}} \cos^6 \theta_{\text{sp}}} - 2d \sin 2\theta_{\text{sp}} + d \sin 4\theta_{\text{sp}}}{2(2 \cos 2\theta_{\text{sp}} + \cos 4\theta_{\text{sp}} + 1)} \quad (3.9)$$

To find the offset, the above minimum is solved to find $\xi(y = 0) = 4d \sec \theta_{\text{sp}}$, and subtracted from Equation 3.9. The remaining equation is then solved for d ,

$$\begin{aligned} d = & \left(-4\sqrt{2} \left(\delta^2 \sin^2 \theta_{\text{sp}} \cos^4 \theta_{\text{sp}} + \delta^2 \sin^2 \theta_{\text{sp}} \cos \theta_{\text{sp}} \cos^4 \theta_{\text{sp}} - 4y^2 \right. \right. \\ & \left. \sin^2 \theta_{\text{sp}} \cos^5 \theta_{\text{sp}} - 6y^2 \sin^2 \theta_{\text{sp}} \cos^4 \theta_{\text{sp}} - 16y^2 \sin^2 \theta_{\text{sp}} \cos \theta_{\text{sp}} \right. \\ & \left. \cos^4 \theta_{\text{sp}} + 4y^2 \sin^2 \theta_{\text{sp}} \cos \theta_{\text{sp}} \cos^4 \theta_{\text{sp}} - 8y^2 \sin^2 \theta_{\text{sp}} \cos \theta_{\text{sp}} \cos^4 \theta_{\text{sp}} \right)^{1/2} \\ & \left. - 2\delta \sin \theta_{\text{sp}} - 4\delta \sin 3\theta_{\text{sp}} + \delta \sin \theta_{\text{sp}} - 4\delta \sin \theta_{\text{sp}} \right) \\ & \cdot \left(4(2 \cos \theta_{\text{sp}} + 3 \cos \theta_{\text{sp}} - 3 \cos \theta_{\text{sp}} + \cos 5\theta_{\text{sp}} - 2 \cos \theta_{\text{sp}} - 1) \right)^{-1}. \end{aligned} \quad (3.10)$$

where δ is the distance the cone extends at the coordinate y . By following the aforementioned procedure, given the dimensions of the pixels on the imaging sensor, d can be determined. Once d is known, the absolute coordinates (x, y, z) of the sensor are given by

$$\begin{pmatrix} x \\ y \\ z \end{pmatrix} = \begin{pmatrix} x' \cos \theta_{\text{sp}} + d \sin \theta_{\text{sp}} \\ y' \\ d \cos \theta_{\text{sp}} - x' \sin \theta_{\text{sp}} \end{pmatrix} \quad (3.11)$$

where x' and y' are the local coordinates of the sensor with $(0, 0)$ as its origin.

3.7.2 Extracting the Speckle Line

To prepare the camera data for data analysis, the next step in the post-processing workflow involves “unwrapping” the cone image; transforming the hyperbolic shape on the image sensor into a straight one. The unwrapping step is accomplished using the software program Fiji [56] and a straightening algorithm based on cubic spline interpolation [69]. The procedure is depicted in Figure 3.9.

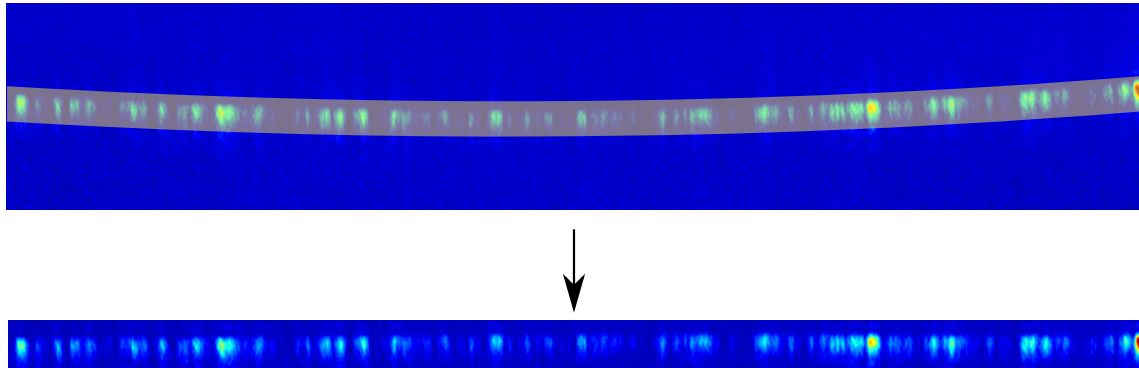


Figure 3.9: Illustration of the unwrapping procedure for the cone image. The spline region (highlighted in yellow) in the above image is converted to the rectangular region in the image below for further post-processing.

4 | Interference

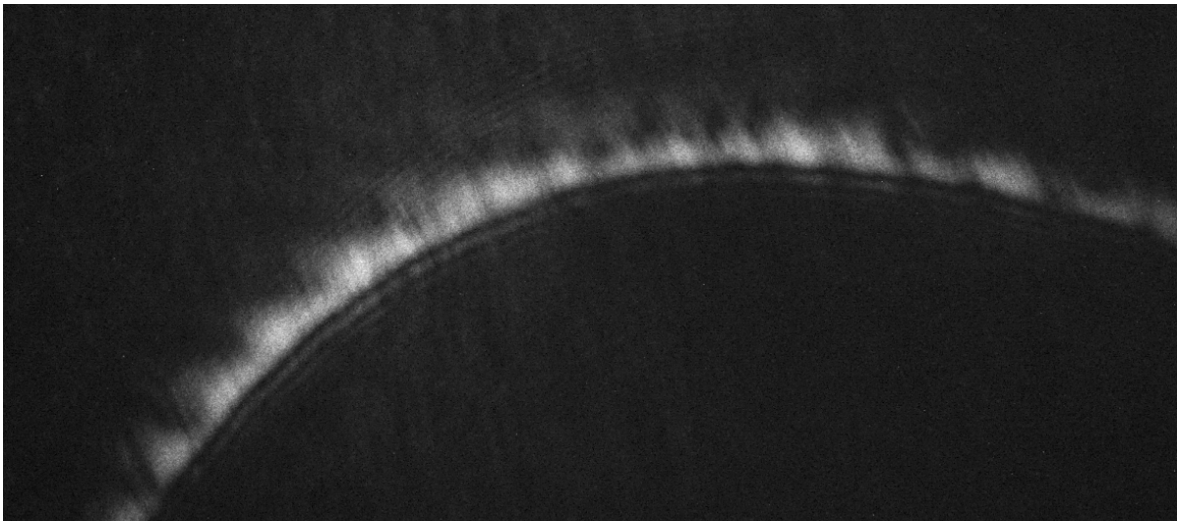


Figure 4.1: Section of the cone exhibiting one-sided interference fringes. System parameters: $\lambda_0 = 632.8 \text{ nm}$, $n_1 = 1.9961$ (LAH79), $n_2 = -14.48 + 1.09i$ (silver), $n_3 = 1.0$ (air), and $d_2 = 48 \text{ nm}$.

When SPPs are excited in a prism-coupled setup using a focused beam, it is possible to observe a fringed spatial interference in either the specular or conically scattered light [70]. Surprisingly, despite the popularity of SPR as a biosensing tool, the phenomena went unreported until 2005 [29] [26], and has since then only been reported in a handful of limited cases [71] [27]. An example of the pattern in the cone is shown in Figure 4.1 for a silver film on high refractive index glass (LAH79) in air. In the present chapter it is shown that, in contradiction to previous explanations [29] [26], the interference phenomena may be observed without any contribution from specular reflection.

4.1 Theory

For simplicity the problem is restricted to the x - z plane. Consider an incident p -polarized Gaussian beam passing through a prism evanescently exciting either normal or long-range SPPs on a metal film. On the film, the Gaussian beam may be represented in k -space as

$\tilde{g}(k_x)$, where

$$\tilde{g}(k_x) = \frac{w_0}{\sqrt{2}} \exp\left(\frac{1}{4}w_0(k_x - k_{\text{sp}})\right) \quad (4.1)$$

$$= \int_{-\infty}^{\infty} g(x) e^{ik_x x} dx \quad (4.2)$$

and

$$g(x) = \exp\left(-\frac{x^2}{w_0^2} + ik_{\text{sp}}x\right), \quad (4.3)$$

where w_0 denotes the Gaussian beam waist parameter at the focus. In the specular direction, the field $\tilde{E}_{\text{notch}}(k_x)$ is given by its Fresnel reflectivity $\tilde{r}^p(k_x)$ multiplied by $\tilde{g}(k_x)$,

$$\tilde{E}_{\text{notch}}(k_x) = \tilde{g}(k_x) \tilde{r}^p(k_x). \quad (4.4)$$

Consider the spatial evolution of the light as it propagates away from the surface. The complete field in both x and z can be obtained by computing the Fourier transform of $\tilde{E}_{\text{notch}}(k_x)$ multiplied by a free space transfer function $e^{ik_z z}$

$$E_{\text{notch}}(x, z) = \int_{-\infty}^{\infty} \tilde{E}_{\text{notch}} e^{ik_z z} e^{ik_x x} dk_x \quad (4.5)$$

$$= \int_{-\infty}^{\infty} \tilde{g}(k_x) \tilde{r}^p(k_x) e^{i\sqrt{k_0^2 \epsilon_1 - k_x^2} z} e^{ik_x x} dk_x \quad (4.6)$$

Likewise, the conically scattered field may be found using the same treatment yielding

$$E_{\text{cone}}(x, z) = \int_{-\infty}^{\infty} \tilde{g}(k_x) \tilde{t}_+^p(k_x) \tilde{t}_-^p(k_x) e^{ik_z z} e^{ik_x x} dk_x. \quad (4.7)$$

Though the integral seems to have no analytic solution, its evaluation is nonetheless straightforward on a computer. The same Fourier transform recipe may be used to find fields in three dimensions, as was done in Section 2.4.2.

4.2 Experiment

Experimental verification of the predictions of Equations 4.6 and 4.7 was performed with the setup shown in Figure 4.2. Light from an unpolarized 30 mW 632.8 nm helium-neon laser first passes through the polarizing beamsplitter BS. It is then expanded and recollimated by lenses f_1 and f_2 as an approximately Gaussian beam with a $1/e^2$ beam waist of 3 mm. The light is steered by mirrors m_1 and m_2 to lens f_3 , antireflection-coated aspherical lens with a focal length of 20 mm, which focuses the light to the central point of the hypotenuse of a 10 mm diameter LAH79 hemispherical prism ($n(632.8 \text{ nm}) \approx 1.98$). The beam makes a central angle of $\theta_{\text{sp}} \approx 32^\circ$ with the hypotenuse. On the hypotenuse of the prism is a 49.8 nm silver film obtained through a sputtering process (See Section 3.2). The specific thickness was chosen to optimizes the far field ATR

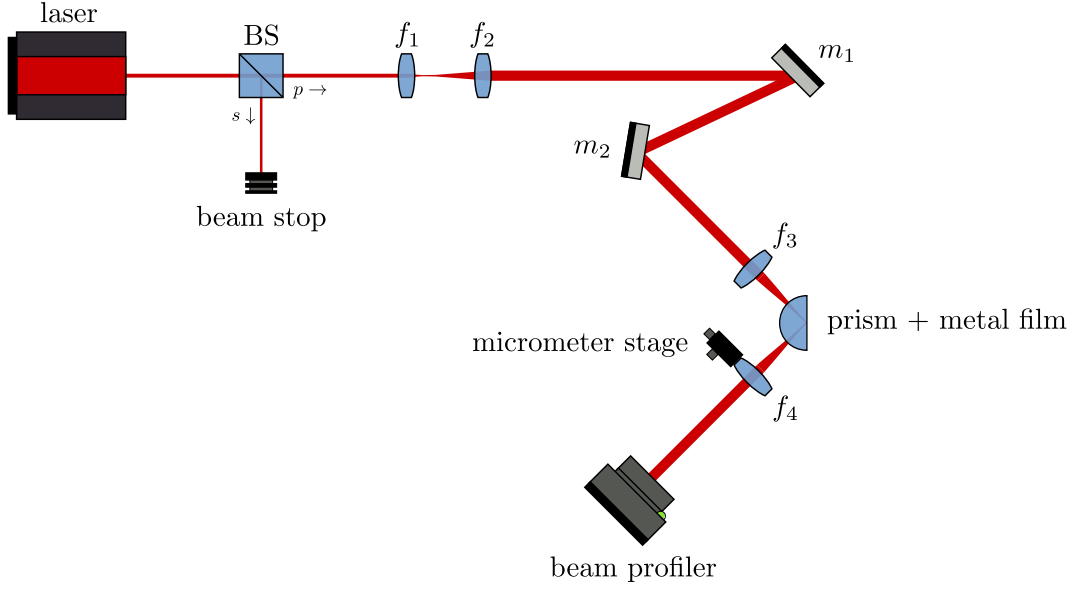


Figure 4.2: Experimental setup. Light from a laser passes through beamsplitter BS passing p-polarized light and expanded by two lenses, f_1 and f_2 . Mirrors m_1 and m_2 steer the expanded beam to lens f_3 , focusing the light onto the hypotenuse of a hemispherical prism. Lens f_4 re-images the reflected field to a beam profiler where it is recorded.

minimum in the specularly reflected direction. Silver was used because it has the longest SPP propagation length of all readily available sputtering targets. Consistent with the Fourier optics perspective, a longer SPP propagation length on the interface results in a narrower resonance linewidth in the far field and vice versa. An LAH79 hemispherical prism was used because of its high refractive index ($n \approx 1.98$ at 632.8 nm) and because its hemispherical shape permits observation of scattered light with minor distortion. The totally internally reflected or scattered light is optionally imaged at this point by the lens f_4 , which is identical to lens f_3 . The optical fields are observed by direct projection on a 10-bit CCD sensor (beam profiler). Since most of the interesting spatial structure of the reflected beam occurs in a small spatial range, Lens f_4 is mounted on a micrometer stage. As the stage is translated, different focal planes can be imaged.

Verification of the optical fields were obtained using a beam profiler for an optimally focused lens f_3 while the focal plane of lens f_4 was moved normal to the direction of radiation. Images at increasing distances from the surface were taken of light in both the notch ($\phi = 0$) and the cone at an angle $\phi = 90^\circ$. Since the cone is more or less radially isotropic, the choice of ϕ in this experiment is arbitrary as long as it is far enough away from the incident or specular beam. The data is shown in Figure 4.3 along with theoretical calculations based on Equations 4.6 and 4.7. Linear (2D) sections of the experimentally obtained results for three different characteristic propagation distances are also shown. The $z = 10 \mu\text{m}$ and $z = 100 \text{ mm}$ distances are representative of the near and far field; their optical fields related by a Fourier transform. The intermediate propagation distance $z = 0.1 \text{ mm}$ was chosen because of the high visibility of the interference fringes. As is evident from the figures, as the field propagates it diffracts, exhibiting an evolving asymmetric fringe structure between the near and far fields. The experimentally obtained

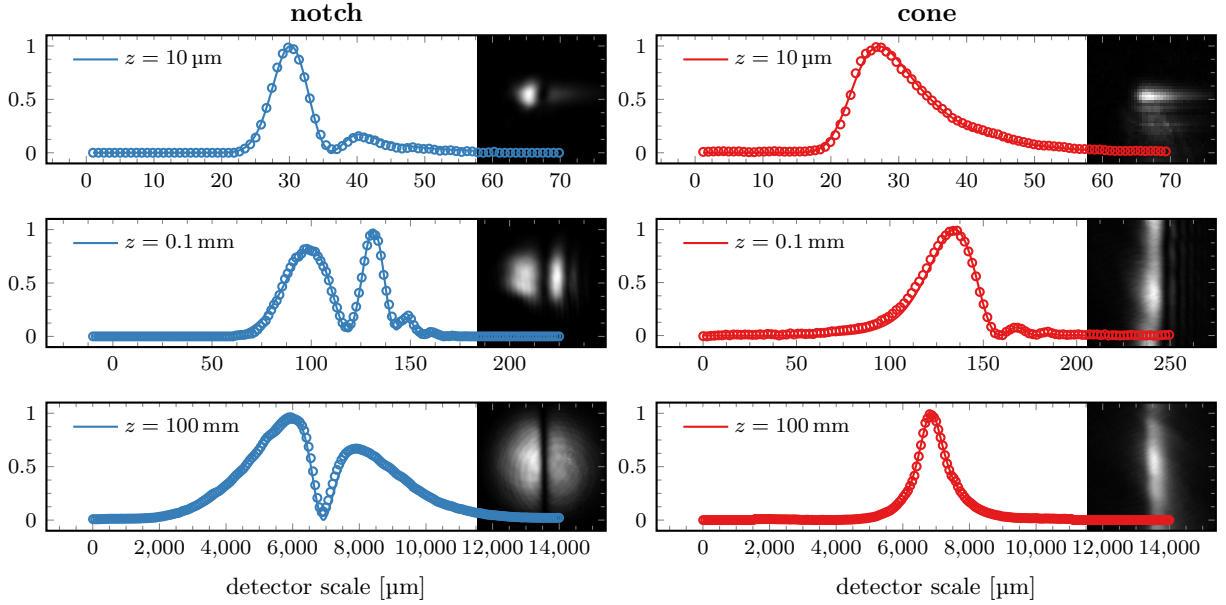


Figure 4.3: Theoretical and experimental values of $|E_{\text{notch}}(x, z)|^2$ and $|E_{\text{cone}}(x, z)|^2$ obtained for three characteristic propagation distances. Theoretical values are solid lines, while experimental values are shown with points. Distances are approximate. Inset is the experimentally obtained optical intensity.

field matches well with theoretical calculations using an unmodified Drude model for silver.

The far field is often defined as $z \gg 2D^2/\lambda$, where D is the spatial width of the source. For silver at 632.8 nm, the Lorentz-Drude model permittivity is $\epsilon = -14.48 + 1.09i$ and the 1/e SPP propagation distance normal to the interface $D = 1/(2k_x) \approx 17 \mu\text{m}$ and the resulting far field limit is $2D^2/\lambda \approx 10 \text{ mm}$. This seems to be consistent with both the simulated and experimental results, as it is approximately the distance in Figure 4.3 for which the interference fringes disappear.

At $z = 0$, $|E_{\text{notch}}(x, z = 0)|^2$ matches the near field theoretically predicted via a similar method by CHUANG [28], or through vector Gaussian beam decomposition [1], shown in Figure 4.4 for comparison. It has also been experimentally verified through near field optical measurements [2], though this only permits observation of the field on the 2–3 interface, or $|E_{\text{cone}}(x, z = 0)|^2$. Near field measurements of the 1–2 interface are not possible due to the presence of the prism. It is interesting that both fields have been obtained using optical-only methods; both SPP propagation and re-radiation are obtained simultaneously. The results by BAIDA (Figure 4.4) are very similar to what was obtained in Figure 4.3. In this sense, $|E_{\text{cone}}(x, z = 10 \mu\text{m})|^2$ approximates the field on the metal-vacuum/air (2–3) interface and $|E_{\text{notch}}(x, z = 10 \mu\text{m})|^2$ the metal-glass (1–2) interface. The SPP propagation distance is greater for BAIDA due to a difference in the value chosen for the permittivity of silver: $-17.9 + 0.7i$ versus the value of $-14.48 + 1.09i$ used for the calculation of Figure 4.3.

As a final comparison, Figure 4.7 shows a near-field measurement of the optical field on the metal-air (2–3) surface made by DAWSON [2] using a photon scanning tunneling

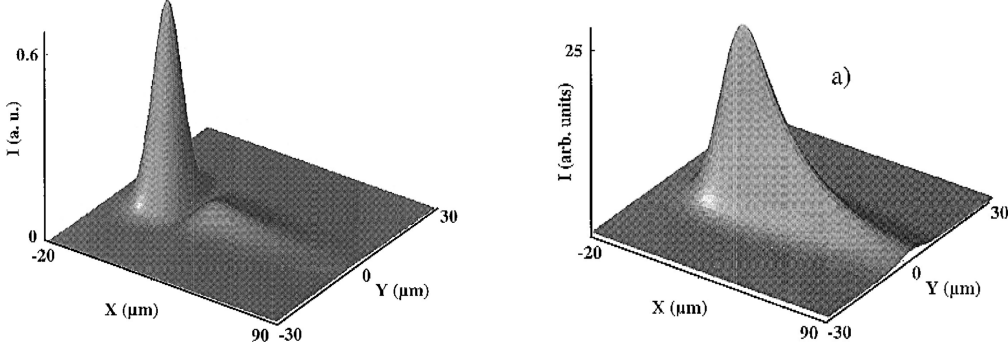


Figure 4.4: Predictions of the optical field made by BAIDA [1]. On the left is the field on the metal-glass (1–2) interface. On the right, the field on the metal-vacuum (2–3) interface. Compare with the near fields for the notch and cone in Figure 4.3.

microscope (PSTM). As mentioned, this method only permits measurements on one side of the metal film. Again, except for the differing values of the dielectric function for silver (determining the propagation length), the results match BAIDA and Figure 4.3.

4.2.1 Interference and Diffraction

Previous reports of the spatial interference fringes in the specular direction for long-range [27] and conventional surface plasmons [29] have described it as arising due to interference between the specular reflection of the Gaussian beam from the 1–2 interface and the re-radiated plasmon field from the 2–3 interface. These components can be identified by the two peaks in the near field specular signal (Figure 4.3, $z = 10 \mu\text{m}$). While it is true that the field in the specular direction contains both components, and that \tilde{r}_{12} and \tilde{r}_{23} are indeed antiphas e at k_{sp} , the fringes do not require a specular component to be observed.

In Figure 4.8, the contribution of the 1–2 interface has been removed by propagating $\tilde{r}_{123} - \tilde{r}_{12}$ to $z = 1.17 \text{ mm}$. Nevertheless, the fringes persist despite the absence of \tilde{r}_{12} . In terms of the experiment, removing \tilde{r}_{12} , the specular reflection, is equivalent to what is found in the cone (itself containing fringes).

In light of these observations, it is more correct to ascribe the fringe structure as being a diffraction, rather than a two component interference phenomena motivated by phase alone (although there are two components in the specular direction). Note that similar behavior is found in almost any causal function propagated by a free space transfer term, for example the Fourier transformed Lorentzian absorption $\tilde{f}(k) = 1/(1 + ik)$.

The asymmetry of the interference results from the causality of the system. Assume a complex function $\chi(\omega) = \chi'(\omega) + i\chi''(\omega)$ whose real and imaginary parts are related by Kramers-Kronig relations

$$\chi(\omega) = i\mathcal{H}^+(\chi(\omega)) \quad (4.8)$$

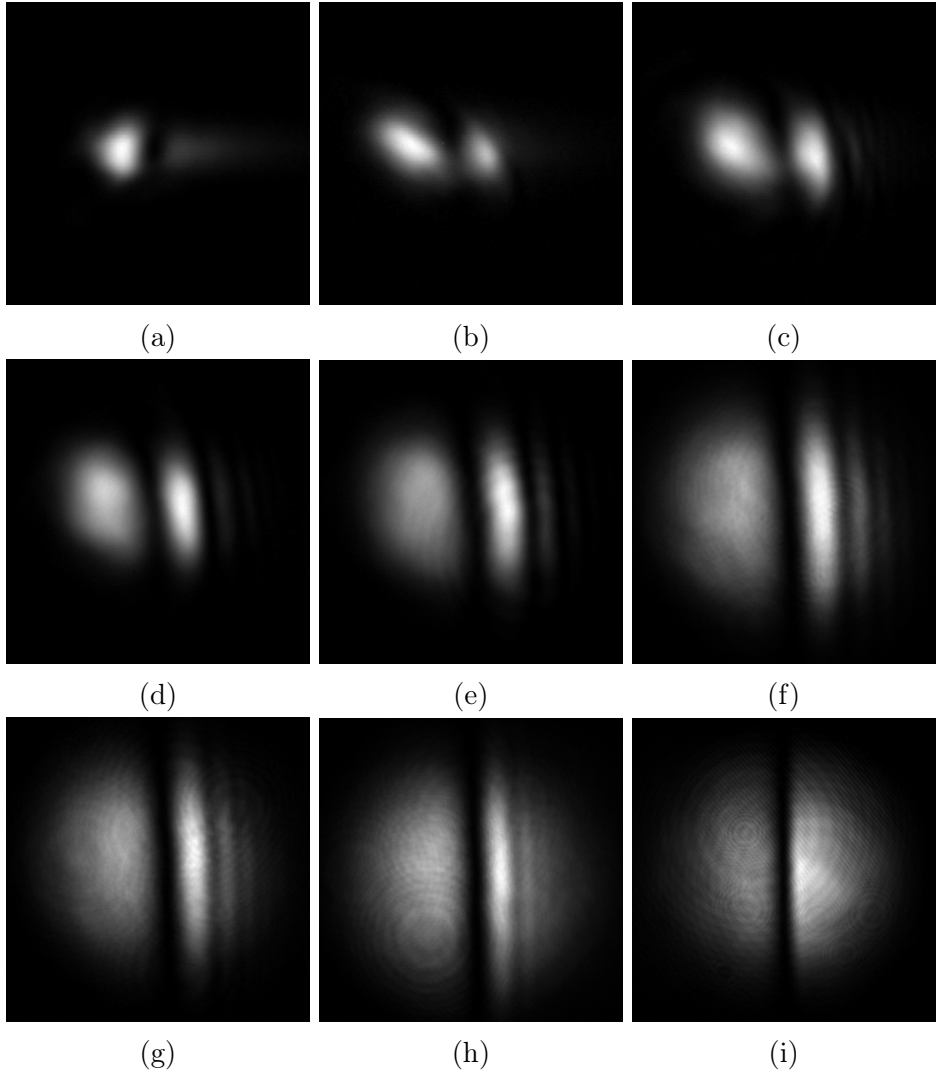


Figure 4.5: Images of the optical field in the specular direction as the focal plane of f_4 is moved from (a), best focus, to (i), the far field. All images have been normalized relative to themselves.

with

$$\chi'(\omega) = \mathcal{H}^+(\chi''(\omega)) \quad (4.9)$$

$$\chi''(\omega) = -\mathcal{H}^+(\chi'(\omega)) \quad (4.10)$$

where $\mathcal{H}^+(\chi(\omega))$ is the Hilbert transform of $\chi(\omega)$. The Fourier transform of $\chi(\omega)$ is

$$\chi(\omega) = \chi'(\omega) + i\chi''(\omega) \quad (4.11)$$

$$\mathcal{F}^+(\chi(\omega)) = \mathcal{F}^+(\chi'(\omega) + i\chi''(\omega)) \quad (4.12)$$

$$= \mathcal{F}^+(\chi'(\omega)) + \mathcal{F}^+(i\chi''(\omega)) \quad (4.13)$$

$$= \mathcal{F}^+(\chi'(\omega)) + \mathcal{F}^+(i\mathcal{H}^+(\chi'(\omega))) \quad (4.14)$$

$$= \mathcal{F}^+(\chi'(\omega)) + \text{sgn}(\omega)\mathcal{F}^+(\chi'(\omega)) \quad (4.15)$$

$$(4.16)$$

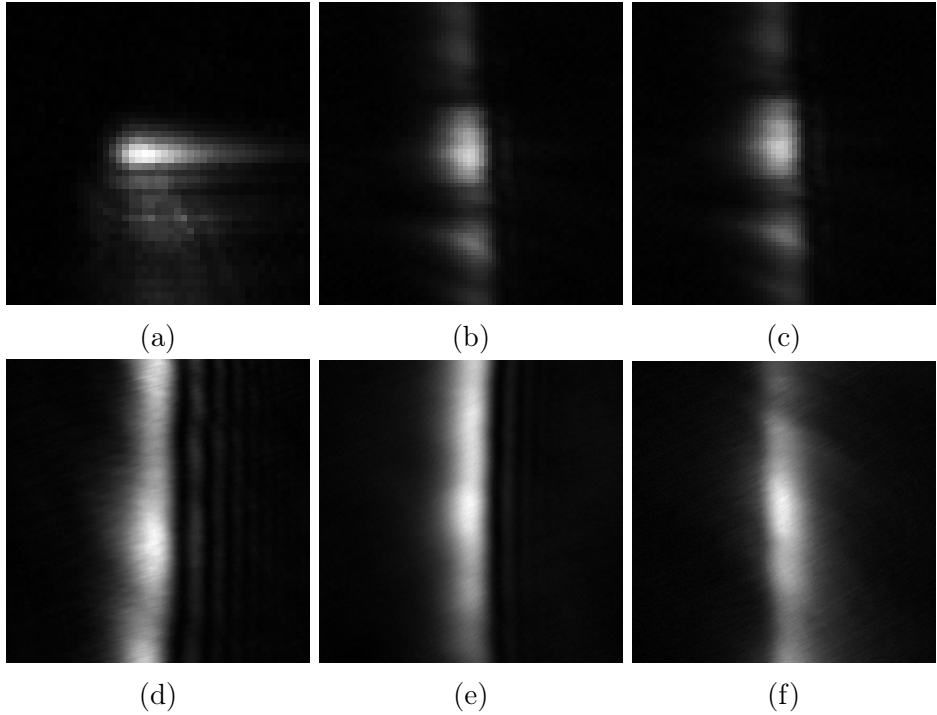


Figure 4.6: Images of the optical field for the section of the conically scattered light as the focal plane of f_4 is moved from (a), best focus, to (f), the far field. All images have been normalized relative to themselves.

Or succinctly,

$$\mathcal{F}^+(\mathcal{H}^+(\chi(\omega))) = (-i \operatorname{sgn}(\omega)) \mathcal{F}^+(\chi(\omega)) \quad (4.17)$$

In other words, the Fourier transform of any function which satisfies Kramers-Kronig relations is asymmetric (“one-sided”) as a necessary condition of causality. This condition is also known as Gibb’s phenomena. Since no physical system can respond infinitely fast to an input signal, high frequency components are lost. In the case of SPR occurring at the focus of an incident Gaussian beam, it can be seen as a spatial filter which modifies the local k -vectors to produce the resulting far field optical pattern. If the SPR resonance condition is sharp, the Fourier integral (Equation 4.6) is truncated and the plasmon resonance acts as a low pass filter for light.

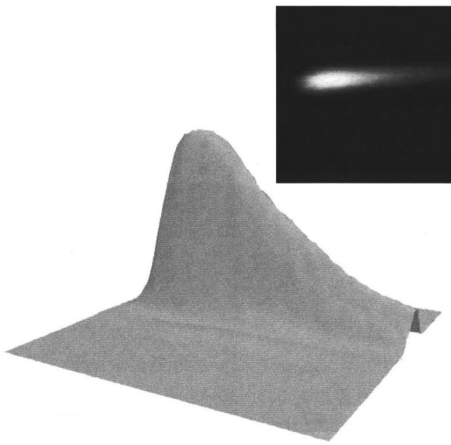


Figure 4.7: Photon scanning tunneling microscope image of the metal-vacuum (2–3) interface from DAWSON [2]. No scale was given except that the 1/e propagation length was 13.8 μm . Compare with the near field cone image in Figure 4.3. The model of DAWSON assumes a 2.65 nm layer of Ag_2S on top of the silver layer, hence the reduced SPP propagation length.

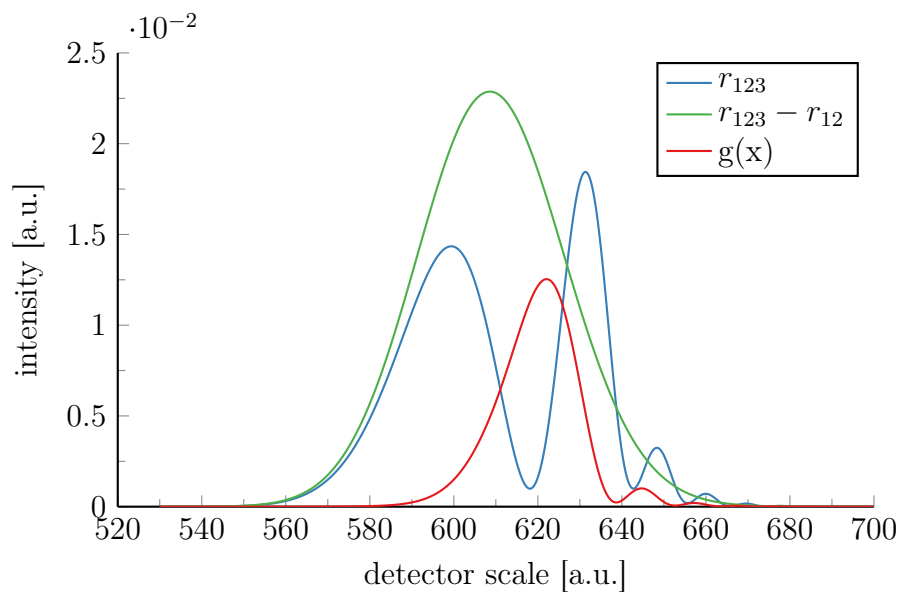


Figure 4.8: Comparison of the propagated $\tilde{r}_{123}(k_x)$ versus $(\tilde{r}_{123}(k_x) - \tilde{r}_{12})$. Note that interference fringes occur in both cases.

5 | Speckle

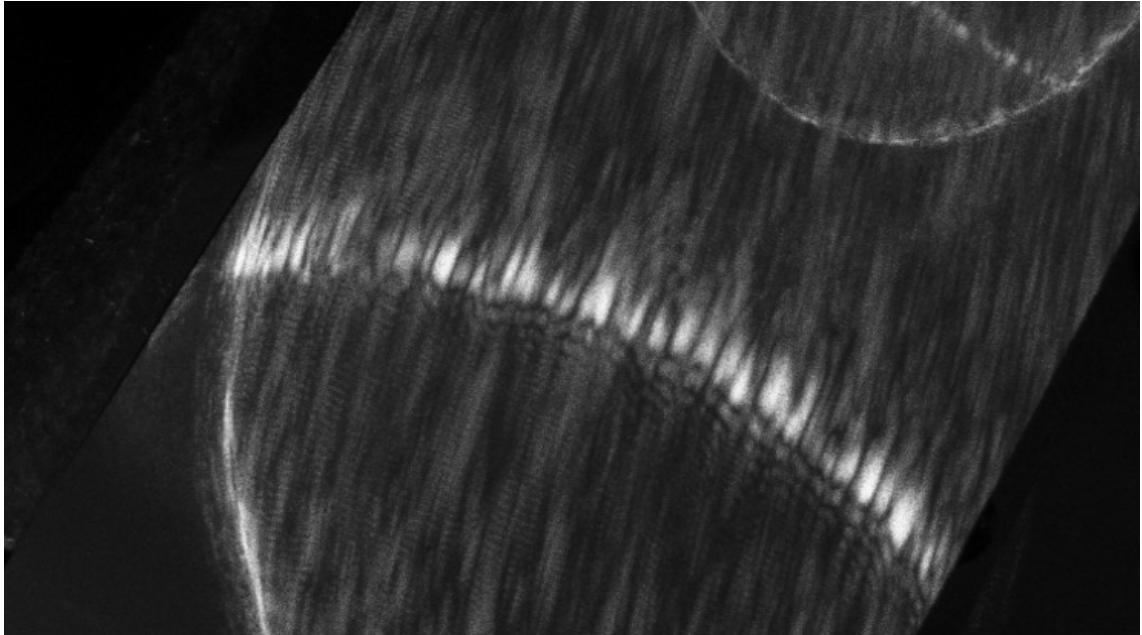


Figure 5.1: A portion of the cone speckle, distorted by a lens and projected onto a piece of paper.

5.1 Introduction

Under most circumstances, light in the cone is not spatially homogeneous but exhibits distinctive intensity fluctuations known as *speckle*, which arise from the interference of multiple coherent waves with statistically random amplitudes and phases. In optics, speckle is closely related to the mesoscopic phenomena of universal conductance fluctuations [72] and it likewise exhibits many of the same physical phenomena such as coherent backscattering [73] and the memory effect [74].

Speckle is also known to host a wealth of interesting properties [33] [75], particularly in the multiple scattering regime [76] where it has been shown to be extraordinarily sensitive to both the position and motion [34] of its underlying scatterers. Indeed, in this way speckle may be seen as a unique fingerprint [77] of the underlying scattering

microstructure. Such principles have already been exploited in a diverse set of applications such as diffusing wave spectroscopy [37] and dynamic light scattering [78] in the time domain. Furthermore, speckle has been shown to be sensitive to the sub-wavelength motions [36] or inclusions [35] of even single scatterers.

As there is no prior work related to cone speckle, the present chapter begins with the mathematical and statistical properties of generalized speckle fields, and how well the speckle in the cone can be described by them. In particular, two important characteristic properties of speckle, size and contrast, will be measured and compared with the theory. Any specific influence regarding dynamic changes in the underlying scattering microstructure are reserved for Chapter 6.

5.1.1 Objective Speckles

Speckle produced by the SPP scattering geometry in Figure 3.2, when measured by an imaging sensor in the far field (Fraunhofer regime), is known as *objective speckle*. Features of objective speckle are typically not applicable to speckle obtained in e.g. the near field regime. Most pertinent, the mean speckle size is approximately given by $\lambda z/d$, where λ is the wavelength, z is the propagation distance, and d is the transverse dimension of the scattering spot[79].

5.2 Intensity Distribution and Contrast

Consider an SPP excited by a focused beam in a prism-coupled setup. Without loss of generality, the center of the focused beam is defined as the origin of a three-dimensional Cartesian coordinate system (x, y, z) . If the beam is incident in the x - z plane, the SPP has an initial phase of $\exp(i k_{\text{sp}} x)$. In the present analysis, the out of plane components of the Gaussian beam are neglected.

As mentioned in Section 2.5, surface roughness or other inhomogeneities can elastically scatter an SPP during propagation. SPP scattering on the surface changes the direction, but not the magnitude, of the in-plane k -vector. Upon re-radiation as a photon, the phase to a point (x', y', z') in the far field is

$$\exp\left(ik_0\sqrt{(x-x')^2 + (y-y')^2 + (z-z')^2}\right). \quad (5.1)$$

In the present coordinate system, $z = 0$ is the plane of scattering and the contribution to the field by a single scattering event is

$$\mathbf{E}(x', y', z') = \exp(i k_{\text{sp}} x) \exp\left(ik_0\sqrt{(x-x')^2 + (y-y')^2 + (z-z')^2}\right). \quad (5.2)$$

Equation 5.2 assumes single scattering: an SPP is scattered only once during its propagation.

It is further assumed that the $(x, y, z = 0)$ coordinates from which an SPP is re-radiated as a photon are randomly distributed following the treatment of GOODMAN [32] for random phasor sums. To wit, the field at each detector position $\mathbf{E}(\mathbf{r})$ is due to the coherent linear superposition of N random phasors

$$\mathbf{E}(\mathbf{r}) = \frac{1}{\sqrt{N}} \sum_{n=1}^N a_n e^{i\varphi_n}, \quad (5.3)$$

where a_n and φ_n is the amplitude and phase of the n th phasor and φ is randomly distributed on the interval $(-\pi, \pi)$. For SPP scattering, φ is the phase of Equation 5.2. In reality these conditions may be loosened by the physics of the actual experiment, which we describe shortly.

By the central limit theorem, as $N \rightarrow \infty$, the resultant probability distribution function (PDF) $p_{\mathbf{E}}(\mathbf{E})$ of $\mathbf{E}(\mathbf{r})$ is Rayleigh distributed and the corresponding probability distribution function $p_I(I)$ of the intensity $I(\mathbf{r}) = |\mathbf{E}(\mathbf{r})|^2$ is an exponential

$$p_I(I) = \frac{1}{2\sigma_I^2} \exp\left(-\frac{I}{2\sigma_I^2}\right). \quad (5.4)$$

Given that the q th moment of $p_I(I)$ is

$$\bar{I}^q = (2\sigma_I^2)^q q! \quad (5.5)$$

$$= \bar{I}^q q!, \quad (5.6)$$

the standard deviation is equal to the mean, $\sigma_I = \bar{I}$. Equation 5.4 can then be rewritten as

$$p_I(I) = \frac{1}{\bar{I}} \exp\left(-\frac{I}{\bar{I}}\right). \quad (5.7)$$

As a convienient measure, the *contrast*, C , is defined as the ratio of the standard deviation to the mean of the intensity

$$C = \frac{\sigma_I}{\bar{I}} \quad (\text{speckle contrast}). \quad (5.8)$$

The exponential PDF and unity contrast are often mentioned as the reason for the discincitive “speckled” appearance of speckle [32].

5.3 Limiting Cases

There are two important cases for which the statistical properties of a random phasor sum break down: a small number of scatterers and a single scatterer whose intensity dominates amongst many. These two cases can easily occur in the physical experiment, and it is therefore important to identify their features.

5.3.1 A Small Number of Scatterers

For a small number of scatterers [80] N of intensity a , $\rho_I(I)$ becomes [32]

$$p_I(I) = 2\pi^2 \int_0^\infty \rho J_0\left(\frac{2\pi a\rho}{\sqrt{N}}\right)^N J_0\left(2\pi\sqrt{I}\rho\right) d\rho, \quad \rho_I^2 = (1 - 1/N)a^4. \quad (5.9)$$

Equation 5.9 is shown in Figure 5.9 for $N = 2, \dots, 5$ along with a histogram for a single simulated realization of a 2D speckle pattern generated using Equation 5.3. That the simulated speckle pattern is in two dimensions instead of three is not significant; in each case the notion of a random phasor sum holds. No ensemble averaging was used, though is typically required to produce reasonable statistics [32].

From Figure 5.9 it is apparent that, for speckle described by a random phasor sum with a low number of scatterers, Equation 5.9 converges to Equation 5.7 rapidly as N increases. At $N = 6$, the sum squared error as compared with $N \rightarrow \infty$ is only 4.75×10^{-5} . In terms of physical SPP scattering, random phasor sum statistics can be used to a good approximation to describe the resulting distribution, even down to a fairly low number of scatterers.

5.3.2 A Strong Single Scatterer

The next edge case is that of a strong single scatterer, shown in Figure 5.10. The intensity PDF is modified from a Rayleigh distribution to a Rician [32]

$$p_I(I) = \frac{1}{\bar{I}_n} \exp\left(-\frac{I}{\bar{I}_n} - r\right) 2I_0\sqrt{\frac{I}{\bar{I}_n}r}, \quad (5.10)$$

where r is the relative scattering strength of the dominant scatterer compared to the mean intensity, $r = I_0/\bar{I}_n$ where I_0 is the intensity of the single scatterer. Modifying the intensity of a single scatterer is equivalent to a random phasor sum plus a constant background. Unfortunately, in an experiment, failure to completely account for background light using dark frames results in speckle statistics indistinguishable from the presence of a marginally strong single scatterer. In experimentally acquiring images of speckle, dark frames have been used in an attempt to keep background noise to a minimum, though some is unavoidable.

In Figure 5.2, experimental speckle intensity PDFs along with surface images are shown for a typical experiment compared with the case of a “strong single scatterer” — the incident beam focused directly on a surface feature which strongly scatters light. The strongly scattering surface feature is readily apparent in its corresponding surface image. 57 nm citrate-capped gold nanoparticles were used in this experiment as scatterers. It is unknown whether the surface feature causing light to scatter strongly is a nanoparticle or nanoparticle aggregation, or simply a surface defect. Plotted along with the speckle intensity PDFs is Equation 5.10 for $r = 0$, typical Rayleigh scattering, and $r = 10$, which fits the observed distribution.

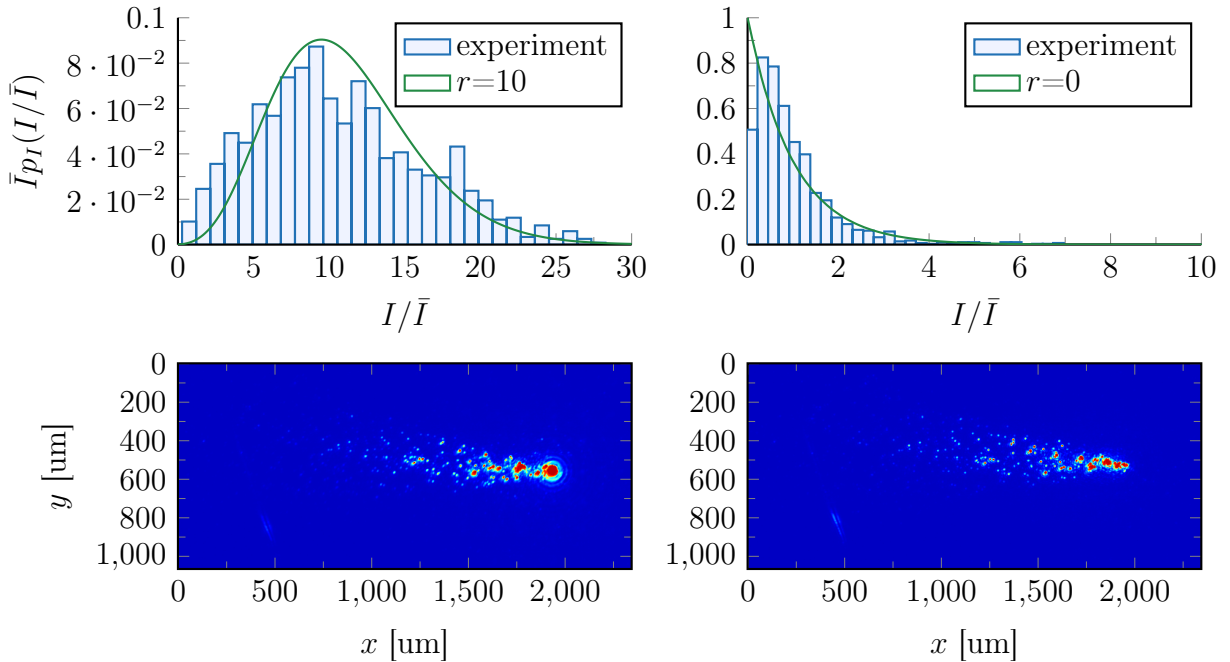


Figure 5.2: Experimental verification of the speckle intensity PDF for a strong scatterer (left) versus traditional Rayleigh speckle (right). Surface images are seen below their respective histograms.

5.3.3 PDF of the Cone Speckle

The intensity PDF of the cone is shown in Figure 5.3 for a single speckle realization at an azimuthal angle of $\phi = 90^\circ$. From a theoretical point of view, the choice of $\phi = 90^\circ$ is arbitrary; the speckle intensity about the cone is homogeneous [30]. However, it is experimentally convenient to observe at this location due to its non-coincidence with the focussing optics. Again, it is usually required to ensemble average over many different realizations, however useful statistics emerge for a single realization when averaging over many speckles, the same strategy employed in multispeckle diffusing wave spectroscopy [81]. The PDF was taken for pixel values along the transverse (azimuthal) speckle coordinate and ensemble averaged over all available pixel ranges.

The observed PDF is well described by the Rayleigh distribution of Equation 5.7. There is a small deviation from Rayleigh statistics to Rician likely attributed to an imperfect background subtraction. The contrast is near unity, with a value of $C = 1.0637$. Averaging over many speckle realizations in addition to the one shown in Figure 5.3 gives the same result of a near unity contrast.

5.4 Size of a Speckle

Together with the contrast [82], the mean size of a speckle is an important figure of merit for a speckle pattern, being connected to the underlying scattering microstructure

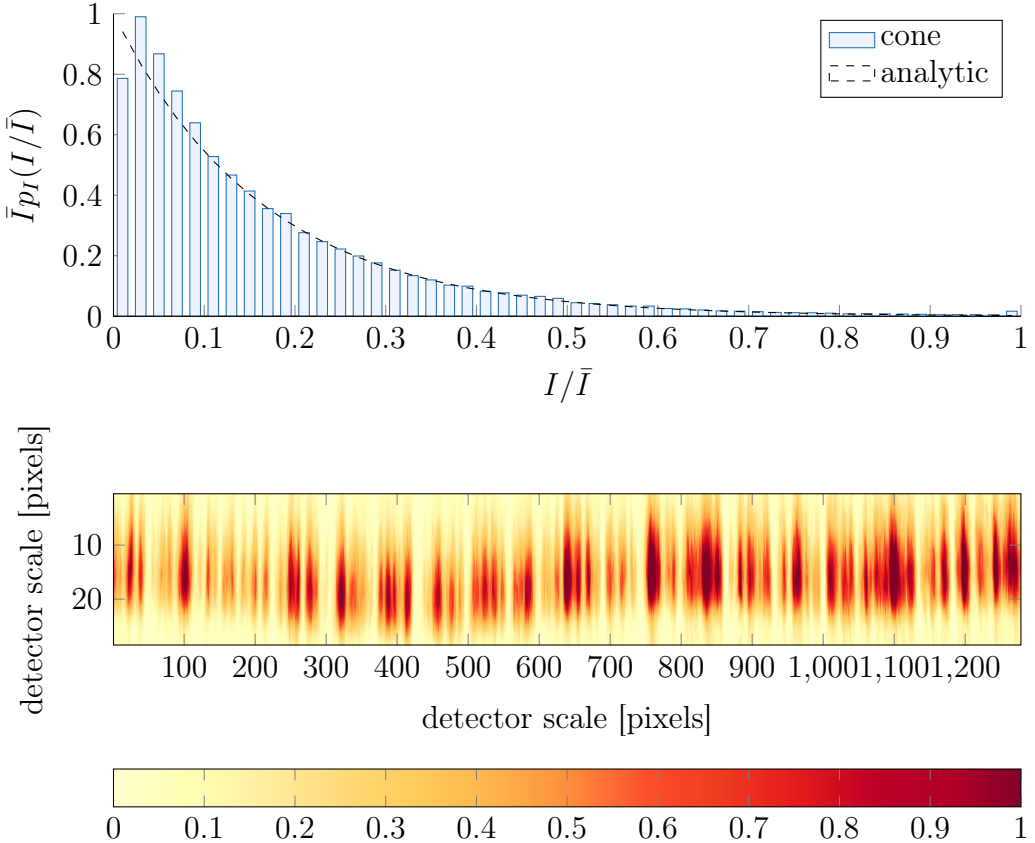


Figure 5.3: Intensity PDF for light in the cone. Top: histogram. Bottom: unwrapped raw data on the sensor.

(surface roughness) and, in the present case, the SPP transport therein.

As discussed earlier, a measurement of the speckle spot size yields the transverse dimension of the coherent source on the scattering surface. Following GOODMAN [33] and DAINTY [79], the size of a speckle is defined in terms of the area of the normalized autocovariance function of the speckle intensity pattern, $c_I(\Delta x, \Delta y)$. The normalized autocovariance function is likewise defined in terms of the autocorrelation $\Gamma_I(\Delta x, \Delta y)$ by

$$c_I(\Delta x, \Delta y) = \frac{\Gamma_I(\Delta x, \Delta y) - \bar{I}^2}{\bar{I}^2}, \quad (5.11)$$

and the autocorrelation is defined as

$$\Gamma_I(\Delta x, \Delta y) = \int_{-\infty}^{\infty} \int_{-\infty}^{\infty} I(x, y) \tilde{I}(x + \Delta x, y + \Delta y) dx dy. \quad (5.12)$$

For computation on real images, the integral is replaced by a sum. Taking advantage of the Wiener–Khinchin theorem, the autocorrelation is simply the Fourier transform of the power spectral density, vis.

$$\Gamma_I(\Delta x, \Delta y) = \mathcal{F}^+ (|I(x, y)|^2)(\Delta x, \Delta y) \quad (5.13)$$

and thus $c_I(\Delta x, \Delta y)$ can be efficiently calculated on a computer¹.

The expected autocovariance for a given specklegram is, via the diffraction limit, the Fourier transform of geometry of the illuminated spot. For a circular spot, c_I is given as a function of angle $\Delta\theta$ by

$$c_I(\Delta\theta) = 1 + \left(\frac{2J_1(u)}{u} \right)^2; \quad u = \frac{d\Delta\theta}{\lambda}. \quad (5.14)$$

Where d is the diameter of the scattering spot and λ is the scattering wavelength. Likewise, the area of a speckle is the integral over c_I in the appropriate coordinate system. Discussion and analysis of the experiment in this regard is found in Chapter 6.

5.4.1 Experiment

To further investigate the nature of speckle in the cone, an experiment was conducted using long-range surface plasmons excited in the Kretschmann ATR geometry. The incident Gaussian beam with wavelength $\lambda = 660\text{ nm}$ was focused on the hypotenuse of the prism using a microscope objective attached to a zoom lens housing, as Figures 3.1 and 3.2. To prepare the scattering surface, 57 nm citrate-capped spherical gold nanoparticles at a concentration of 0.0717 nM were flowed over the sensor for 15 min, and then flushed with distilled water.

Two imaging sensors were employed in the experiment. The first was positioned to capture a section of the cone and its embedded speckle. The second was on the inverted microscope and provided a rough estimate of the spot size of the focused beam.

The angular size of the speckle was computed from the cone images using Equation 5.11, first converting the sensor coordinates from $I(x, y)$ to $I(\theta)$ as described in Section 3.7.2. An approximation of the scattering spot size was also made by computing the 1/e width for a Gaussian fit to the averaged spot profile on the surface image taken by the inverted microscope camera. The results of the experiment are shown in Figures 5.5 and 5.4.

Figure 5.4 shows an example of the raw data from which the data for Figure 5.5 was derived. In the left column, Figure 5.4 shows three example spot sizes measured at 102, 365, and $599\text{ }\mu\text{m}$. To the right of each spot image is its corresponding specklegram. It is difficult to distinguish the difference in speckle sizes between these images.

In Figure 5.5 the angular size of speckles was computed for spot sizes in the range of 100 to $450\text{ }\mu\text{m}$ by ensemble averaging the normalized autocovariance function across different realizations of the same speckle pattern at the same spot size. Surprisingly, the results show a speckle size which is independent of spot size within this range. The intersection of the theoretical prediction from Equation 5.14 and the experimental data occurs at a spot size of $250\text{ }\mu\text{m}$.

This phenomena is *not* present when exciting conventional surface plasmons in a similar setup (Figure 4.2), as evidenced in Figure 5.6 for an Air-Ag-BK7 three-layer setup (see

¹For example in MATLAB this is implemented with `xcov(I, 'coeff')`

Section 4.2). From left to right, each image shows the cone with a progressively tighter focal spot: on the left, a defocused spot, center, a tightly focused spot, and right, a spot focused on a single defect producing a ring without speckle. Although neither the actual spot size nor the camera position was recorded in this particular experiment, the behavior is clearly qualitatively described by Equation 5.14; the size of the speckle is inversely proportional to the spot size.

Equation 5.14 describes an inverse relationship between speckle size and the size of the scattering spot which is in accord with the approximation given by DAINTY [79] of $\lambda z/d$.

5.5 Bulk Refractive Index Sensitivity

Surface plasmon resonance is remarkably sensitive to perturbations in the bulk refractive index of the medium in which SPPs propagate. By monitoring properties of the notch in the specular direction, sensitivities of up to 1×10^{-8} RIU (refractive index units) have been reported in some applications [83], shot noise limited. Bulk refractive index sensing and its limits are particularly well understood [54], so this section focuses on similar types of measurements in the cone. Effects from speckle are not considered.

In a prism-coupled setup, there are three main methods used to monitor changes in the SPR resonance condition. All three of these interrogation methods are equivalent in terms of their real-world resolution and detection limit [8].

Angular The change in the angle of the SPR minimum as a function of refractive index is monitored. In the angular modulation method, the prism may be scanned through a range of angles or the angular spectrum may be obtained simultaneously using a focused beam and sensor array.

Wavelength The prism is fixed in place and its reflectivity at a single angle is monitored as a function of wavelength.

Intensity For a fixed wavelength and incident angle, the intensity of the signal at a certain angular or spatial point is monitored as the experiment progresses.

This section is restricted to analysis in the angular and intensity interrogation methods. The experimental setup does not possess the means to carry out wavelength interrogation, though this is in many ways equivalent to sweeping the SPR angle.

5.5.1 Angular Interrogation

To study the sensitivity in the angular interrogation method, the angular response of the system was simulated using the Fresnel equations with ($\Delta n = 0$) and without ($\Delta n \neq 0$) a refractive index perturbation of the sensing layer. An example is shown in Figure 5.7 for both conventional and long-range SPPs. The choice of $\Delta n = 0.01$ is somewhat arbitrary

and was made to illustrate the change of the resonance line. Notwithstanding, the SPR resonance shifts in response to a refractive index perturbation.

In the simulation, the minimum of the SPR resonance was determined using nonlinear minimization [52] and optimizing the function as $\Delta n \rightarrow 0$. In this way, the maximum theoretical sensitivity for angular sensitivity, $\Delta\theta/\Delta n$ is determined. This theoretical sensitivity should not be confused with real world sensitivity; sources of noise in the experiment and detector are not taken into account. Nor is the present analysis concerned with optimization of sensitivity, rather it is most relevant to ascertain the difference between angular response to refractive index perturbations in the cone and the notch. In compliment to Figure 5.7, the maximum obtainable sensitivities for these configurations are tabulated in Table 5.1. The tabulated data supports the hypothesis that there is no readily apparent sensitivity benefit to the cone versus the notch in angular interrogation. Though the angle of the SPR minima (notch) and maxima (cone) are at slightly different angles, approximately 0.006° , their responses track each other very well.

configuration	notch [deg/RIU]	cone [deg/RIU]
SP	145.231	145.367
LRSPP	39.431	39.381

Table 5.1: Theoretical maximum angular sensitivity, $\Delta\theta/\Delta n$, in degrees per refractive index unit, for the configurations in Figure 5.7.

5.5.2 Intensity Interrogation

In contrast to angular interrogation, intensity interrogation shows differences between the notch and the cone, most likely due to both the sharper resonance and narrower linewidth in the cone. For the systems under discussion, the angular width of the notch was determined to be $\theta_{1/2} = 8.0708^\circ$ for conventional surface plasmons, with the cone being nearly twice as narrow at $\theta_{1/2} = 4.7795^\circ$. Long-range surface plasmons show the same trend, but the discrepancy is not nearly as large with $\theta_{1/2} = 0.2349^\circ$ for the notch and $\theta_{1/2} = 0.2325^\circ$ for the cone. The theoretically predicted maximum sensitivities for both cases are shown in Table 5.2. The tabulated data was obtained using the same nonlinear minimization method as for angular case, but the calculation instead sought the angular location where the difference in Fresnel coefficients is maximized as $\Delta n \rightarrow 0$. Specifically, for an N layer system with refractive indices (n_1, n_2, \dots, n_N) ,

$$\lim_{\Delta n \rightarrow 0} \frac{| |r^p(n_N = n_N)|^2 - |r^p(n_N = n_N + \Delta n)|^2 |_{\max}}{\Delta n}. \quad (5.15)$$

For the cone, the same approach was used but instead of the Fresnel reflectivity, Equation 2.61, $|t_+^p|^2 |t_-^p|^2$. In both cases the signal is normalized to $[0, 1]$ within the same angular range for comparison.

The results of are summarized in Table 5.2. In both cases it is observed $\Delta I/\Delta n$ is higher for the cone as compared with the notch, though the increase is only marginal. In terms

of SPR biosensors, the difference suggests an avenue for sensitivity enhancement, though whether implementing such a strategy is warranted in commercial systems remains to be seen.

configuration	notch [1/RIU]	cone [1/RIU]
SP	32.166	42.305
LRSPP	203.537	251.977

Table 5.2: Theoretical maximum intensity sensitivity, $\Delta I / \Delta n$, for the configurations in Figure 5.1.

5.6 Refractive Index Effect On Speckle

To gauge the effect of a refractive index perturbation on cone speckle, glucose solutions of varying concentrations were introduced into the microfluidic flow cell after 57 μm AuNPs had been adsorbed on to the sensor as in Section 5.4.1.

A 10 % glucose solution was prepared and small amounts of water added until its refractive index as measured by a water-cooled Abbe refractometer was $n = 1.341$ at 20 °C. The refractive index of deionized water was likewise measured at $n = 1.331$. The combination of these two liquids amounted to a refractive index perturbation of $\Delta n = 0.01$. The liquids were introduced into the microfluidic flow cell, deionized water first, and the resulting speckle patterns measured as the experiment progressed.

The primary results of this investigation are depicted in Figure 5.8. Here, two subsequent cone images without (top cone, $\Delta n = 0$, deionized water) and with (bottom cone, $\Delta n = 0.01$, glucose) a refractive index perturbation are shown as one — the images have been added together. The addition of the two images is straightforward as the position of the cone on the sensor shifts along with the perturbation, as is expected. As can be seen without numerical analysis, the structure of the speckle is not appreciably different between the two cases.

The cone images were unwrapped as described in Section 3.7.2 and compared using a one-dimensional average of their azimuthal speckle intensity. At the extreme of $\Delta n = 0.01$, the Pearson product moment correlation coefficient, (see Equation 6.14 and surrounding discussion) which has a value of 1 for perfectly correlated signals, reached a minimum value of 0.9262, and was naturally higher during the transition from $\Delta n = 0$ to $\Delta n = 0.01$.

From the measurements it is apparent that small refractive index perturbations have little effect on the structure of speckle in this setup. In the next chapter it will be seen that the underlying scattering microstructure, not refractive index, is the most sensitive and determining factor concerning speckle. In terms of speckle, decorrelation is expected to occur when the average SPP scattering path undergoes a phase shift of 2π — difficult to realize at this level.

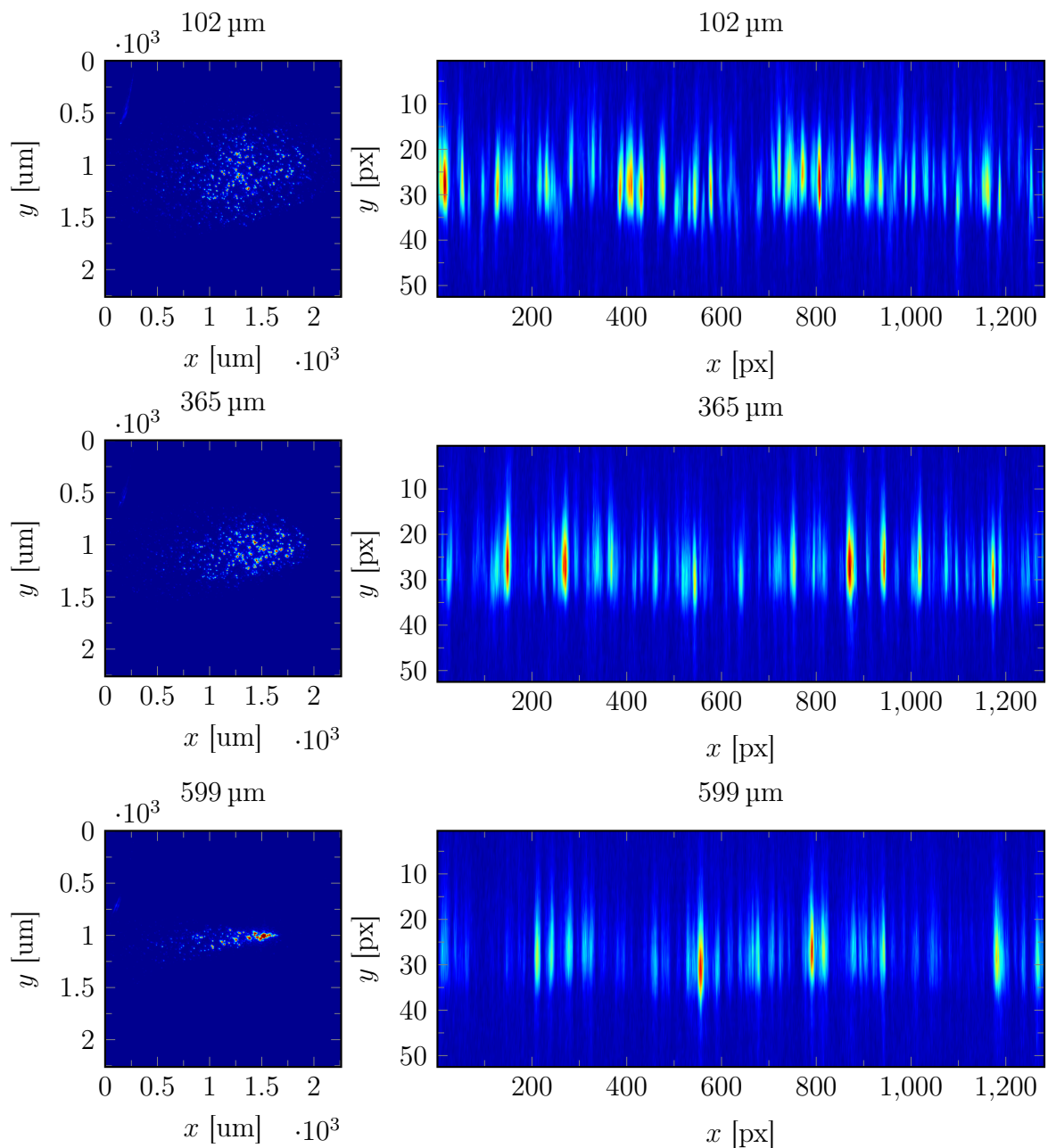


Figure 5.4: Illuminated spot size (left) and corresponding specklegram (right) for three different example spot sizes. Notice that the angular size of the speckles is not significantly different in the three cases.

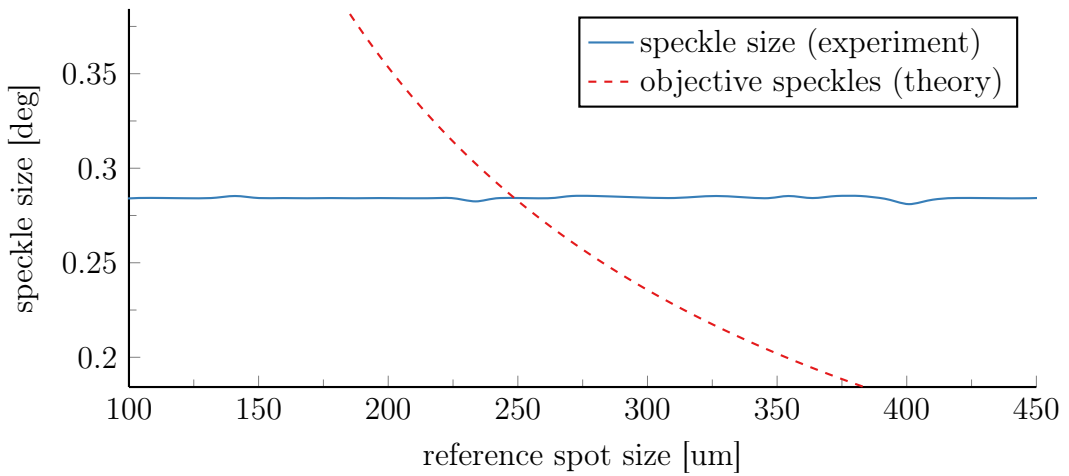


Figure 5.5: Speckle size versus spot size for 57 nm AuNPs adsorbed onto a gold surface in a long-range surface plasmon (symmetric) structure.

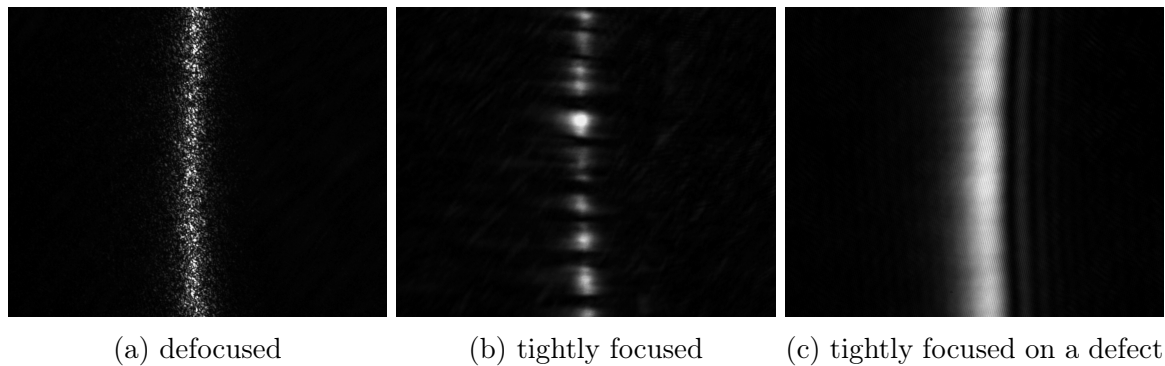


Figure 5.6: Three sections of cone speckle taken for a conventional surface plasmon setup (Air-Ag-BK7) taken using the setup of Figure 4.2. The layer structure is described in Section 4.2. From left to right: defocused, tightly focused, tightly focused on a defect. The actual spot size was not measured in this specific experiment.

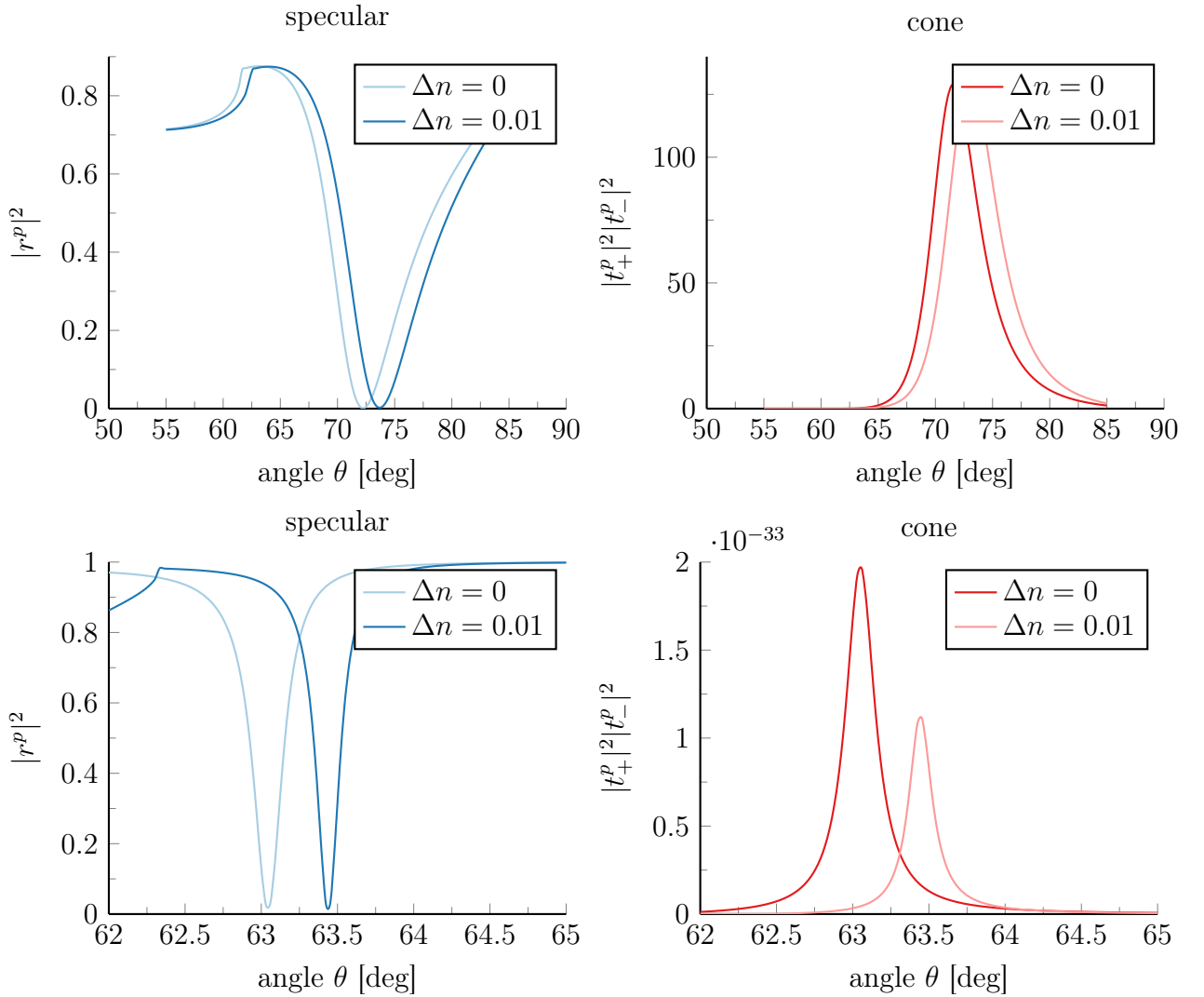


Figure 5.7: (top) Angular sensitivity of the notch and the cone for the Kretschmann three-layer (SP) system. $\lambda_0 = 660 \text{ nm}$, $n_1 = 1.5142$, $n_2 = 0.2843 + 3.3825i$, and $n_3 = 1.3310 + \Delta n$. The thickness of the metal layer is 45 nm. (bottom) Angular sensitivity of the notch and the cone for the Kretschmann four-layer (LRSPP) system. $\lambda_0 = 660 \text{ nm}$, $n_1 = 1.5142$, $n_2 = 1.3489$, $n_3 = 0.2843 + 3.3825i$, and $n_4 = 1.3310 + \Delta n$. The thickness of the metal layer is 16.97 nm.

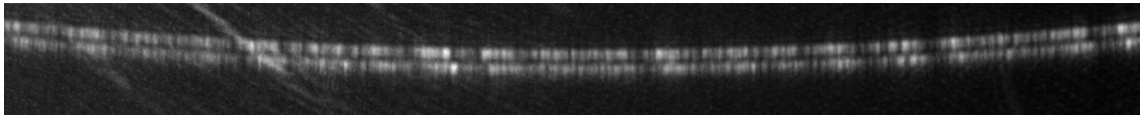


Figure 5.8: Combined cone images of a sample without (top, $\Delta n = 0$) and with (bottom, $\Delta n = 0.01$) a refractive index perturbation.

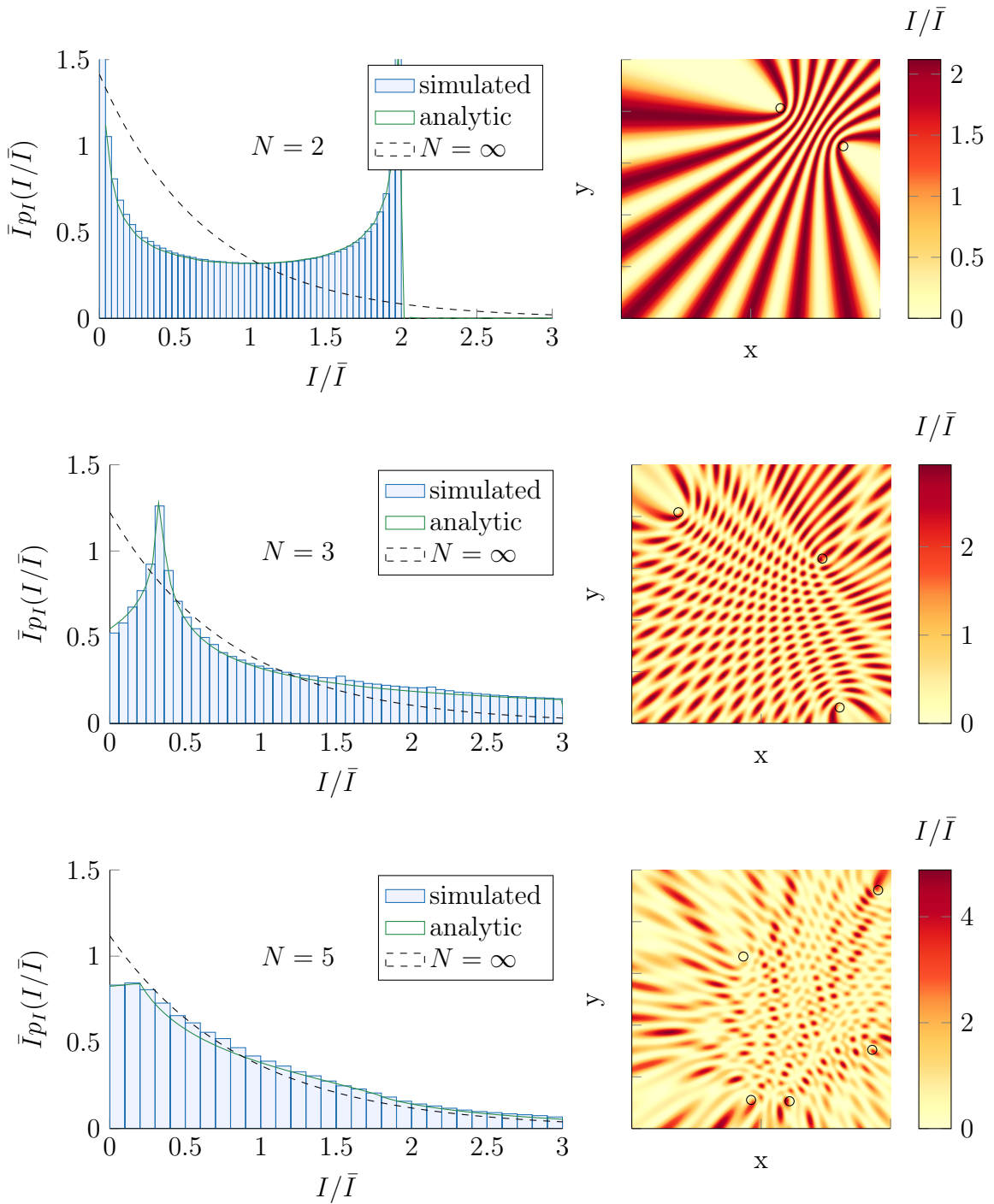


Figure 5.9: Simulated speckle fields and PDF of the resulting intensities for the case of a small number of scatterers. Statistics are obtained from a single realization, which is shown to the left of the histogram. Relative locations of the scatterers are denoted by a circle.

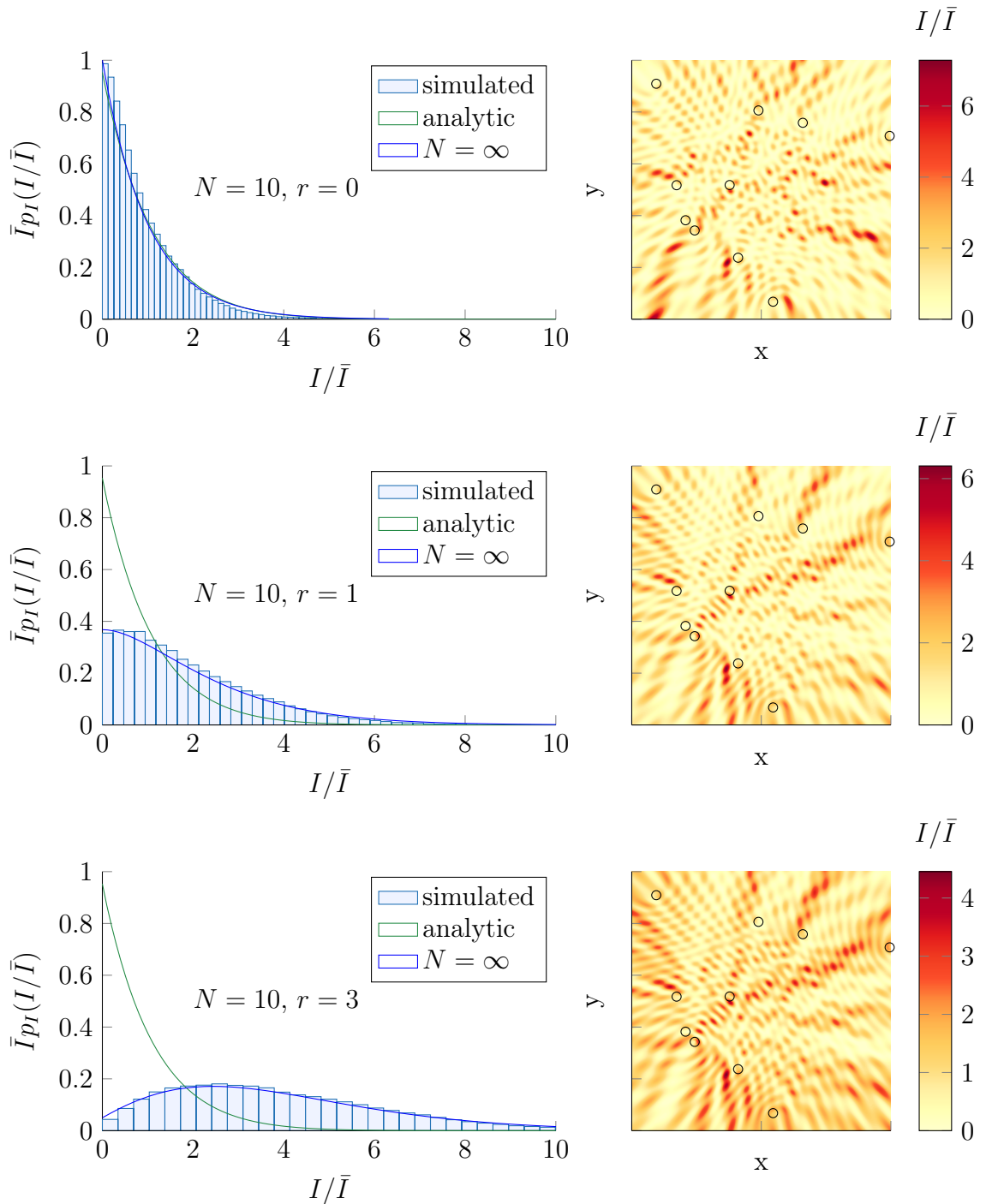


Figure 5.10: Simulated speckle fields and PDF of the resulting intensities for the case of a single scatterer r times brighter than mean background intensity.

6 | Scattering Microstructure

6.1 Introduction

SPR-based biosensors have all but reached their fundamental limits in terms of bulk refractive index sensitivity [54], but as biodetection goals have moved from bulk sensing into the single molecule regime, new techniques for the detection of discrete events are desired. To this end, nanoparticle-based amplification strategies [84] [85] have seen increasing popularity for enhancing SPR measurements, and reports of attomolar resolution are becoming mainstream [86] [87] [88] [89]. Impressive as this is, such measurements still constitute bulk sensing; the presence of a specific nanoparticle is not in and of itself a specific feature of the SPR sensorgram.

As mentioned in the beginning of Chapter 5, speckle can be viewed as a unique fingerprint [77] of the underlying scattering microstructure. Indeed, even a small change in the number or configuration of a system’s scatterers can have a profound influence on the resultant speckle [34] [76]. The effect is particularly significant in the multiple scattering regime, where speckle has been shown to be sensitive to sub-wavelength motions [36] or inclusions [35] of even single scatterers. Such topics belong to a more general class of problems with important implications in diverse fields of study: diffusive wave spectroscopy [37], dynamic light scattering [78], tracking and identification of targets with radio waves (the “cruise missile” problem [38]), fluctuations in signal power in cellular telephone networks [39], and very recently in detecting stress fractures in aggregates such as concrete.

This chapter details investigations regarding the interplay between the underlying scattering microstructure, the in-plane scattering of SPPs, and the optical speckle in the cone. More fundamentally, this chapter is centered around the behavior of speckle in systems where a single scatterer is added to a fixed background of scatterers.

6.2 Scattering Model

The physical scattering process producing speckle in the cone is perhaps best understood in context of the simplified model shown in Figure 6.1. The model is general, but for the sake of discussion it is assumed to be the planar scattering structure for SPP excitation in the setup described in Chapter 3 (see Figure 3.2).

The process is thought of as follows: SPPs are excited and come into existence within the elliptical region of an evanescent wave created by the incident beam (in the x - z plane). The SPP then propagates, potentially out of the elliptical region, until either decaying as heat or re-radiated as a photon out into the cone. SPPs which decay as heat or otherwise do not re-radiate as photons into the cone are unobservable in this experiment and are therefore neglected. During propagation, the SPP follows a scattering path, accumulating phase by visiting one or more in-plane scatterers. The final scatterer is the location where SPPs scatter out of plane into the cone. The superposition of light with phases set by all SPPs paths is responsible for the observed speckle in the cone.

Restated, the individual components of the scattering model shown in Figure 6.1 are:

- An elliptical *illuminated region*, representing the incident evanescent field used to excite SPPs.
- *Scatterers*, fixed point defects, assumed to be randomly distributed, which modify the in-plane momentum of an SPP and optionally cause its re-radiation as a photon out of plane into the cone.
- A *scattering path*, the ordered sequence of scatterers an SPP visits before exiting the system.
- An SPP *creation point*, where an SPP comes into existence and begins accumulating phase.

Physically there are two possible in-plane scattering processes, both of which are depicted in Figure 6.1. The first is *single scattering*, whereby only one scatterer is visited in each path from source to observation. An example single scattering path is given in Figure 6.1 by the path $\{C_{ss}, 3\}$, where an SPP is created at C_{ss} , propagates to scatterer 3, then is re-radiated into the cone.

In addition to single scattering, there exists a much more interesting and phenomenologically complex process known as *multiple scattering*. In multiple scattering, each path from source to observation contains multiple scattering events. An example multiple scattering path is shown in Figure 6.1 by the path $\{C_{ms}, 5, 6, 9, 10, 12, 14, 10, 14, 13\}$. This path serves to illustrate several important assumptions which are made regarding the behavior of a multiple scattering path:

- The scatterers are randomly distributed (true for single scattering as well).
- The same scatterer has the possibility of being visited an arbitrary number of times, e.g. $\{10, 12, 14, 10, 14\}$.
- Closed loop and time reversed paths are possible, e.g. $\{10, 12, 14\}$. In these cases the accumulated phase is the same regardless of direction, e.g. $\{10, 12, 14\} \equiv \{14, 12, 10\}$. Such paths are said to have *time reversal symmetry*.

Note the first scatterer visited in both example paths for single and multiple scattering, 3 and 5 respectively, are directly downstream of their SPP creation points. That is to say, to a good approximation, the first scatterer is always located in the $+x$ direction; in the coordinate system of Figure 6.1, an SPP at its creation point has momentum in the $+x$

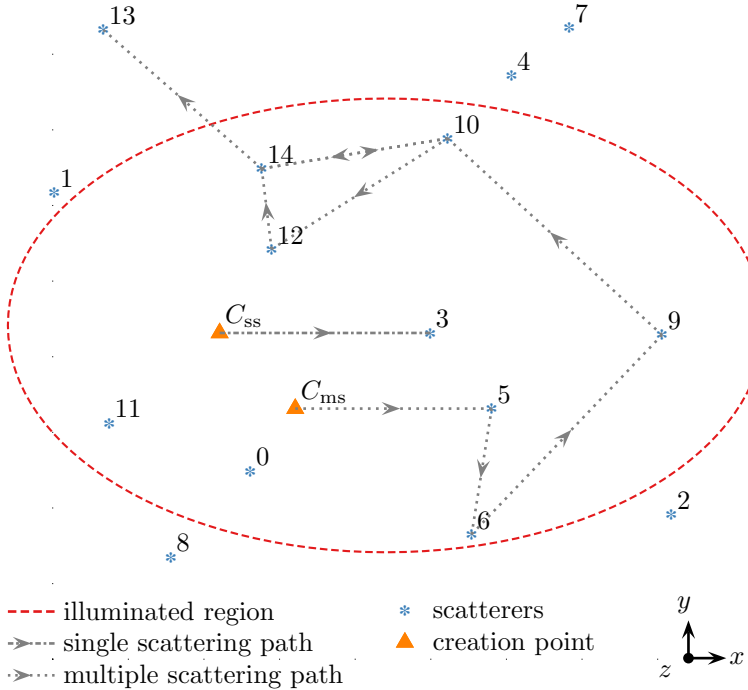


Figure 6.1: A simplified SPP scattering model. An SPP is excited within the illuminated region at its creation point and follows a scattering path amongst fixed point scatterers (numbered). The scattering path can include one (single scattering) or more (multiple scattering) scatterers. The beam creating the illuminated region is incident from the $+x$ direction.

direction. Including this assumption in the scattering model implies not all scatterers can be reached in a single scattering process or as the first scatterer of a multiple scattering process (e.g. scatterers 1, 13, 8, 4, and 7).

6.2.1 Phase Accumulation and Extension to the Far Field

The local in-plane scattering process in the simplified model of Figure 6.1 will now be extended to describe light in the cone. Assume that each scatterer has a location given by the Cartesian coordinates $(x, y, z = 0)$, where the central point of the prism's hypotenuse on the far surface of the film is the origin $(0, 0, 0)$. The central point of the focus of the incident Gaussian beam (the illuminated region) is also coincident at $(0, 0, 0)$.

In the cone, the detector (a two-dimensional image sensor) is assigned the coordinates (x', y', z') . Again, the film is in the x - y plane and the incident light in the x - z plane. The field on the detector has either two or three phase contributions, depending on the scattering order. The first, φ_{loc} , comes from the phase of the local SPP field propagating on the surface in the $+x$ direction to the first scatterer,

$$\varphi_{\text{loc}} = k_{\text{sp}}x. \quad (6.1)$$

In the example paths of Figure 6.1, the variable x in Equation 6.1 would be the x coordinate of either scatterer 3 or 5. Given an SPP is in phase with the exciting field, the choice of the origin and this first phase is arbitrary but is expressed as in Equation 6.1 for simplicity.

The second phase contribution is φ_{ff} : the phase accumulated from the final out of plane scatterer to the detector in the far field,

$$\varphi_{\text{ff}} = k_0 \sqrt{(x - x')^2 + (y - y')^2 + (z - z')^2}, \quad (6.2)$$

where x , y , and z in Equation 6.2 would assume the coordinates of the final scatterer (3 or 13 in the example paths of Figure 6.1).

Following Equations 6.1 and 6.2, the field on the detector for the n th path in the case of single scattering is given by

$$\mathbf{E}_n(x', y', z') = \mathbf{E}_n \exp(i(\varphi_{\text{loc}} + \varphi_{\text{ff}})) \quad (6.3)$$

$$= \mathbf{E}_n \exp\left(ik_{\text{sp}}x + ik_0 \sqrt{(x - x')^2 + (y - y')^2 + (z - z')^2}\right). \quad (6.4)$$

Or in spherical coordinates, with the detector at (ρ', θ', ϕ') ,

$$\mathbf{E}_n(\rho', \theta', \phi') = \mathbf{E}_n \exp\left(ik_{\text{sp}}x\right) \quad (6.5)$$

$$+ ik_0 \sqrt{(\rho' \sin \theta' \cos \phi' x + x)^2 + (\rho' \sin \theta' \sin \phi' + y)^2 + (\rho' \cos \theta' + z)^2}. \quad (6.6)$$

Again, x , y , and z are the coordinates of the sole scatterer in an individual path of the single scattering process. Note that the refractive index change from prism to air has been neglected. To a good approximation, the hemispherical geometry imparts only a constant phase to each scattering path, and therefore has no effect on the speckle pattern.

For a system with M total scatterers and $N \leq M$ scatterers downstream of a creation point within the illuminated region, a single scattering process will produce N unique phasors over N paths. The n th path has a phase φ_n given by the sum of the local and far field phases,

$$\varphi_n = \varphi_{n,\text{loc}} + \varphi_{n,\text{ff}}. \quad (6.7)$$

Assuming each of the N scatterers is visited with equal probability and SPPs re-radiating as photons are scattered isotropically into the cone, the field on the detector is given by the coherent superposition of the paths,

$$\mathbf{E}(x', y', z') = \sum_{n=0}^{N-1} \mathbf{E}_n e^{i(\varphi_{n,\text{loc}} + \varphi_{n,\text{ff}})} \quad (6.8)$$

$$= \sum_{n=0}^{N-1} \mathbf{E}_n e^{i\varphi_n}, \quad (6.9)$$

where \mathbf{E}_n is the fractional contribution of each scattering path to the total amplitude of the electric field \mathbf{E}_0 set by the incident beam, such that

$$\sum_{n=0}^{N-1} \mathbf{E}_n = \mathbf{E}_0. \quad (6.10)$$

For a multiple scattering process, a third phase term, $\varphi_{\text{ms},n}$, must be included for each scattering path. $\varphi_{\text{ms},n}$ accounts for in-plane multiple scattering, where each of N total paths visits K scatterers amongst the M total. If the ordered scattering sequence for the n th path is given by $\{S_{n,0} \dots S_{n,K-1}\}$, and the positions of the k th scatterer in the path sequence is $(x_{S_{n,k}}, y_{S_{n,k}}, z = 0)$, the phase accumulated for the n th path from multiple scattering is

$$\varphi_{\text{ms},n} = \sum_{k=0}^{K-2} k_{\text{sp}} \sqrt{(x_{S_{n,k+1}} - x_{S_{n,k}})^2 + (y_{S_{n,k+1}} - y_{S_{n,k}})^2}. \quad (6.11)$$

The length of S_n and its ordered sequence is assumed to be produced by a stochastic process and will vary from path to path. The field on the detector for multiple scattering is then given by the superposition of all paths from creation to detector

$$\mathbf{E}(x', y', z') = \lim_{N \rightarrow \infty} \sum_{n=0}^{N-1} \mathbf{E}_n \exp(i(\varphi_{n,\text{loc}} + \varphi_{n,\text{ff}} + \varphi_{n,\text{ms}})). \quad (6.12)$$

Equation 6.12 is akin to the path integral formulation of quantum mechanics. By letting $N \rightarrow \infty$, all possible sequences of S_n (again, produced by a yet unspecified stochastic process) will be explored by the multiple scattering paths weighted by \mathbf{E}_n . In the present set of experiments with a 50 mW diode laser, the limit in Equation 6.12 is for all practical purposes fulfilled. Furthermore it will be assumed that the number of scatterers M is sufficient to produce speckle with statistics given by the random phasor sum model (Equation 5.3).

6.2.2 Transition from Single to Multiple Scattering

The transition from the single to the multiple scattering occurs roughly upon fulfillment of the Ioffe-Regel criterion [90], when the transport mean free path l^* is much larger than the spatial frequency of the optical wave, or

$$kl^* \approx 1 \quad (6.13)$$

where $k = \omega/c$ as usual. The transport mean path is defined as the characteristic distance over which the incident wave is scattered out of its incoming direction [34]. This is the optical analog of electron transport in condensed matter physics. For electron transport, one would use the Fermi wavenumber k_F and take l^* to be the mean free path; materials for which $k_F l^* \gg 1$ are conductors, and materials for which $k_F l^* \ll 1$ are insulators. The multiple scattering regime can also be defined in terms of the sample length L , such that if $l^* \ll L$ and $1/(kl^*) \ll 1$, the system can be thought to be the multiple scattering regime.

6.2.3 Sensitivity and Scattering Paths

The number of scatterers visited in the sequence S_n of a scattering path is fundamental in capturing the essence of both single and multiple scattering. Consider a random phasor sum consisting of N phasors. In the case of single scattering, the N phasors map directly to N scatterers, and the problem is equivalent to a random walk in \mathbb{R}^2 . Assuming all scattering paths equally probable, all phasors will have equal magnitude. Furthermore, the phasor magnitude is assumed to be unity, whereby the mean value of the phasor sum is \sqrt{N} . Upon the addition of an additional ($N + 1$) scatterer, the magnitude of the phasor sum for single scattering is therefore altered by an (ensemble averaged) value of $1/N$.

Determining the sensitivity of a speckle pattern to the addition of a single scatterer in the multiple scattering regime is much more complicated; the mathematics of such a determination are well beyond the scope of the present investigation. Using a ladder-operator approach similar to that of FENG, LEE, STONE, and DOUGLAS [76], BERKOVITZ [36] gives an ensemble averaged sensitivity of $1/N^3$ for multiple scattering in the two-dimensional slab geometry [91].

6.3 Addition of a Single Scatterer

6.3.1 Motivation

Consider cone speckle generated by either single or multiple SPP scattering for N fixed scatterers. How does the speckle pattern change upon the addition of a single ($N + 1$) scatterer?

As outlined in Section 5.5, a traditional SPR biosensor looks at the intensity minimum, or notch, in the system's angular spectrum caused by interference between the specularly reflected light and the antiphase re-radiated SPP field. The location of the notch is of course extraordinarily sensitive to local refractive index perturbations of the sample medium, facilitating detection of the adsorption of analytes to the sensor surface [7].

Light is also scattered into the cone. Though the cone has nearly the same angular bulk response as the notch (Section 5.5), its azimuthal component exhibits speckle, which has been shown to be extraordinarily sensitive to both the configuration and motion [34] of its scatterers, even down to sub-wavelength displacements [36] or inclusions [35] of single scatterers.

This is in essence the principle which will be exploited. If a single gold nanoparticle adsorbs to the sensor surface, the scattering microstructure will be altered and the cone speckle pattern will be altered. The ability to detect such a change will correspond to the detection of a nanoparticle binding event.

6.3.2 Quantifying Changes in Speckle

The Pearson product-moment correlation coefficient (PPMCC), C_I , was chosen to measure changes in the structure of cone speckle upon the addition of scatterers to the underlying scattering microstructure. The PPMCC is defined as

$$C_I = \frac{\text{cov}(a, b)}{\sigma_a \sigma_b}, \quad (6.14)$$

where $\text{cov}(a, b)$ is the covariance between signals a and b , and σ_a and σ_b are the respective standard deviations. C_I assumes a value between 1 (total correlation) and -1 (total anti-correlation), with 0 being no correlation. The PPMCC is especially suited to analyzing speckle as it is relatively insensitive to experimental artifacts such as system noise and global intensity fluctuations.

6.3.3 Theoretical Sensitivity

The theoretical sensitivity of a speckle pattern to the addition of a single scatterer depends strongly on the specifics of the underlying scattering process. The dimensionality, degree of single and multiple scattering, and geometry from which light is both incident and collected must all be taken into account. Such theoretical analysis has been solved for specific cases such as in the transmission geometries of dynamic light scattering or diffusive wave spectroscopy, but in general the problem is difficult. As mentioned in Section 6.2.3, determination of the relevant analytic expressions for the sensitivity of a speckle pattern created by SPP single and multiple scattering are beyond the scope of this work. Experimental findings will therefore be emphasized and compared with numerical simulations where they have been found descriptive.

Though speckle from a single and multiple scattering process share the same first order statistics given in Chapter 5, significant differences emerge in *correlations* between speckle patterns when the system is perturbed. Such correlations are amazingly difficult to compute analytically and have up to now only been determined for a limited number of simple transmission and reflection geometries [34]. Additionally, the mathematical methods used in such computations (Feynman diagrams, ladder propagators, vertex operators, etc.) are beyond the scope of this work. Numerical and statistical methods based on the simplified scattering model of Figure 6.1 are employed to encompass the observed phenomena, drawing comparisons to established theory when available.

6.3.4 Experiment

To demonstrate the principle of the method, 50 nm citrate-capped spherical gold nanoparticles in water were introduced into the microfluidic cell and monitor the system as the particles adsorb to the gold sensor surface. These particles scatter light strongly enough that they were able to be observed with the inverted microscope (similar to a TIRF setup) while simultaneously recording the speckle.

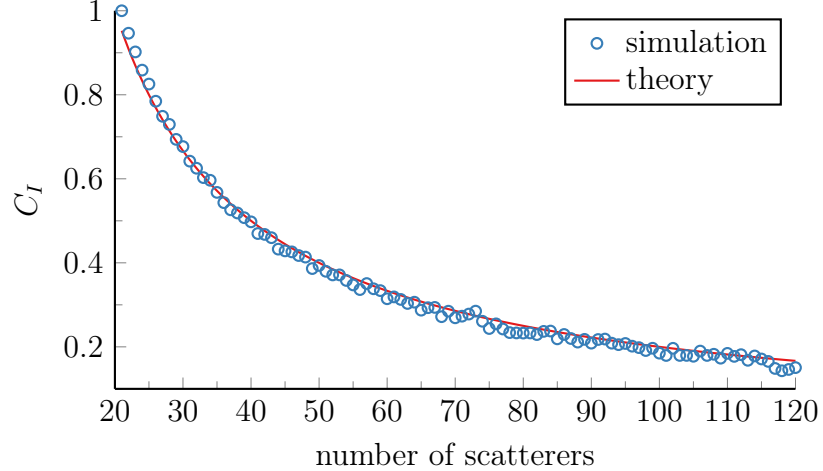


Figure 6.2: Ensemble-averaged Monte Carlo simulation comparing the Pearson product-moment correlation C_I for the addition of a single scatterer in both single and multiple scattering systems.

The experimental setup is as depicted in Figure 3.1. Light from a 50 mW 660 nm diode laser is coupled into a single mode fiber and is re-collimated into a cage system mounted on rotation and translation stages. The light is incident on a polarizing beamsplitter passing p -polarized light, and continues through a 10x objective which is focused on the hypotenuse of a hemispherical prism. Upon the prism's hypotenuse is a structure containing a gold surface whereupon SPPs are excited. The specularly directed and scattered light is collected directly by two imaging sensors, one in the specular direction and one in the cone 90 deg out of this direction. The entire setup is mounted on an inverted microscope stage. A 10x objective is focused on the underside of the prism and simultaneously records the focal spot through an additional image sensor. The sensing area of the prism is enclosed in a transparent microfluidic cell, permitting the controlled introduction of a sample.

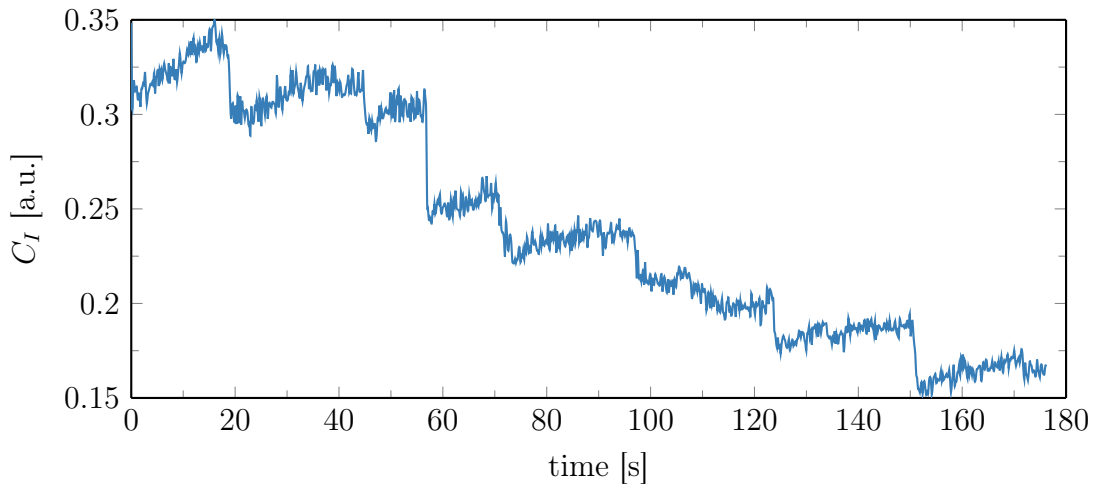


Figure 6.3: Change in speckle measured through the PPMCC (top) before (bottom left) and after (bottom right) the adsorption of a nanoparticle.

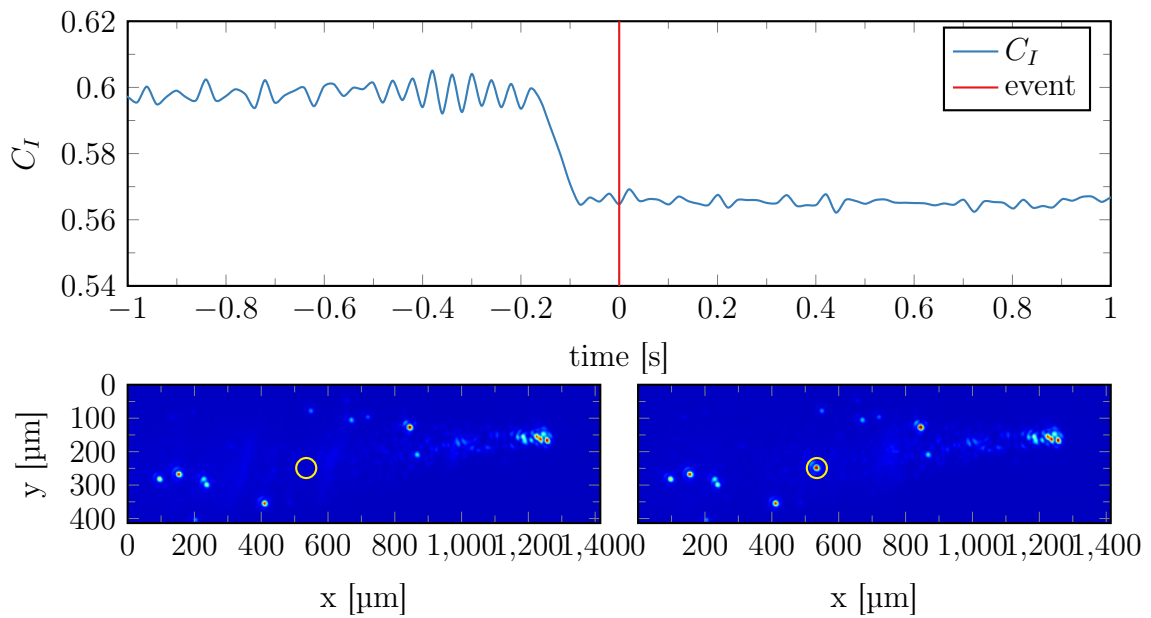


Figure 6.4: Change in speckle measured through the PPMCC (top) before (bottom left) and after (bottom right) the adsorption of a nanoparticle.

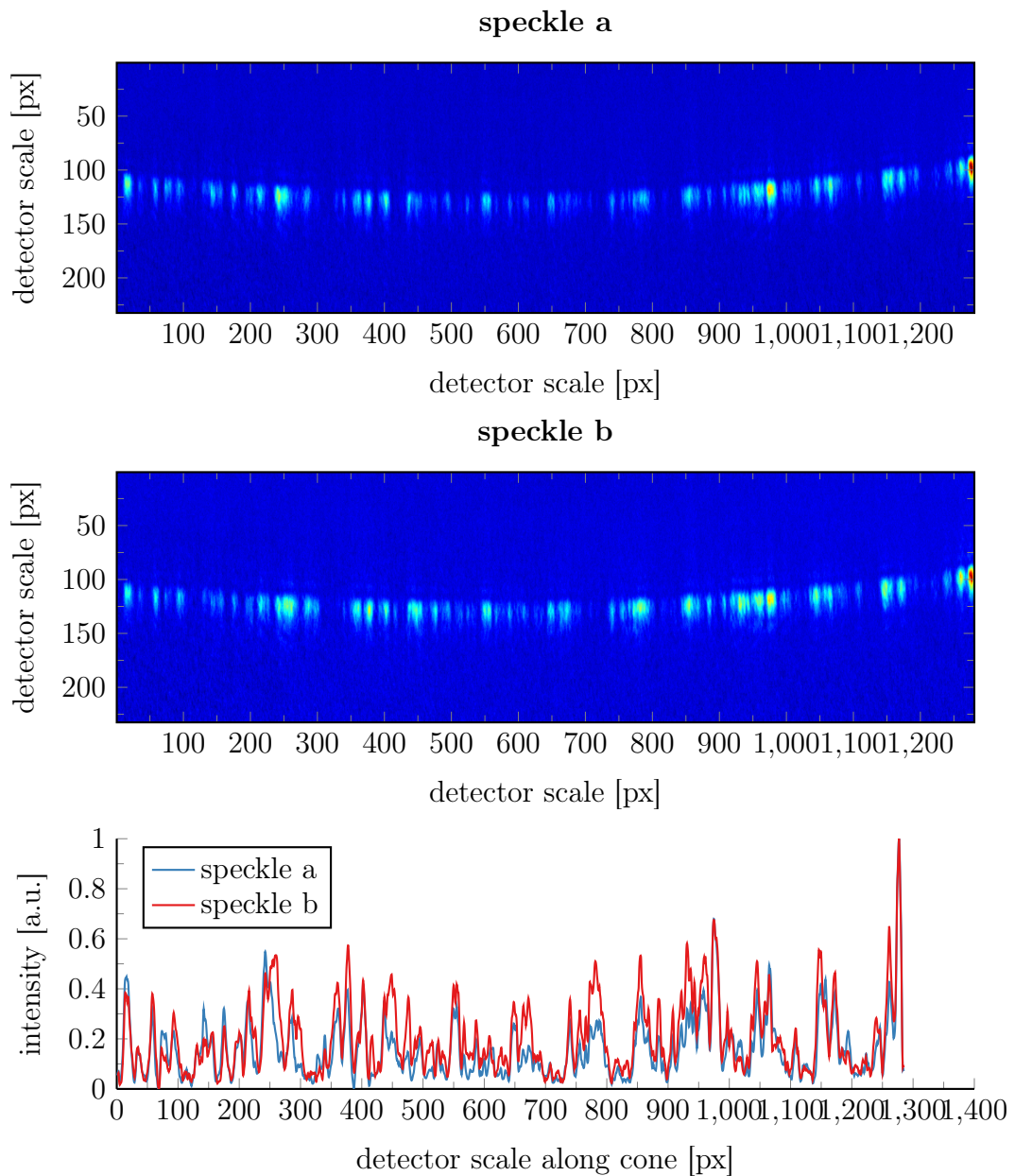


Figure 6.5: Visual change in the specklegram upon the adsorption of a nanoparticle. This figure is taken from the same data and timeframe as a compliment to Figure 6.4.

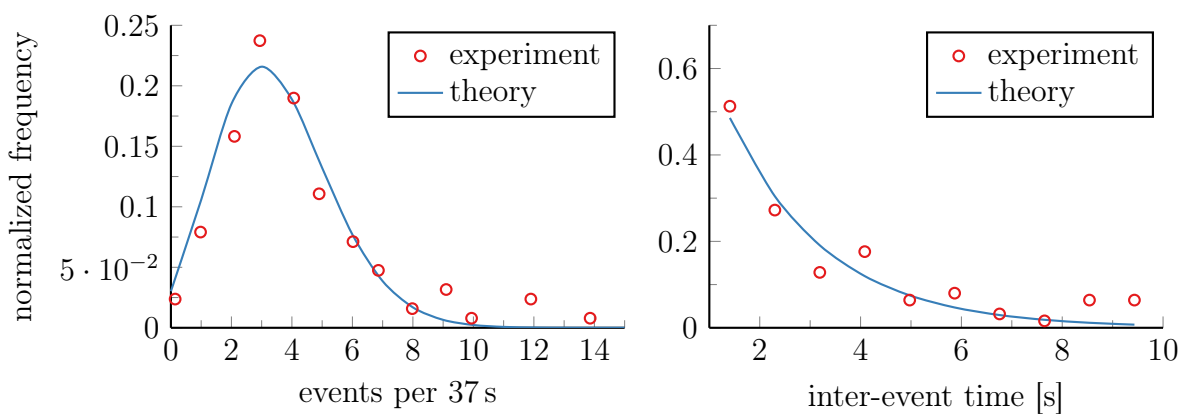


Figure 6.6: Statistics of nanoparticle adsorption. Right: event frequency. Left: inter-event time. Adsorption statistics match well that of theoretical Poisson statistics.

Part II

The Centrifugal Force Quartz Crystal Microbalance

1 | Foundations

1.1 Introduction

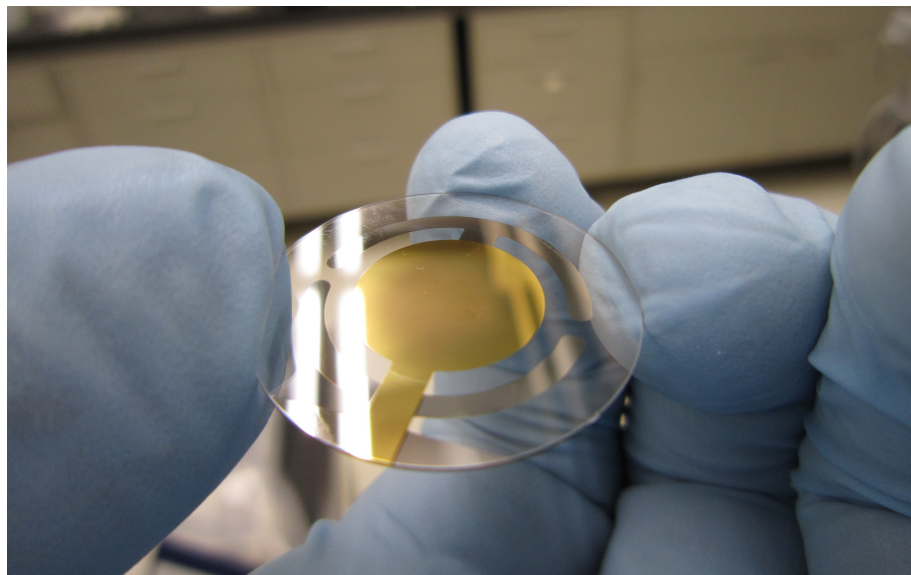


Figure 1.1: A 25 mm 5 MHz quartz crystal microbalance.

There are few experimental techniques allowing the application of force on biological molecules. Among them, optical or magnetic tweezers and atomic force microscopes (AFMs) have provided much insight into the mechanics of molecules such as DNA [92] [93], improved understanding of friction and wear in proteins [94] [95], and have even been able to observe stepwise motion of motor proteins [96].

However powerful, these methods are not able to be deployed as integrated devices to probe the mechanical properties of heterogeneous samples in a wide range of applications; tweezer and AFM experiments rely on highly trained experimentalists, are not widely applicable as analytical tools, and are often constrained to the analysis of well-prepared homogeneous samples not amenable to multiplexing.

Among tools suitable for direct mechanical transduction, the quartz crystal microbalance (QCM) has seen increasing real-world utility as a simple, cost effective, and highly versatile mechanical biosensing platform. A QCM is typically a thin disk-shaped piece of strategically cut piezoelectric quartz with electrodes on either side. When part of an

electronic oscillator circuit, the quartz can form a mechanical resonator which vibrates at certain fundamental frequencies. Changes in the fundamental frequencies and their associated bandwidths upon sample adsorption or desorption are related to the properties of the sample and the strength of its coupling to the QCM. Since its introduction by Sauerbrey [97] in 1959 as sub-monolayer thin-film mass sensors in the gas phase, the understanding of QCM sensors has been repeatedly enhanced to study phenomena such as viscoelastic films in the liquid phase [98], non-destructive contact mechanics [99], and complex topologies of biopolymers and biomacromolecules [100].

Naturally, QCMs do not come without their own disadvantages. The underlying mechanical properties of the sample are often not revealed by the stepwise changes in the QCM sensorgram, an issue complicated by the choice of theoretical model. Operation of QCMs in the liquid phase is also associated with a rather low-Q resonance, limiting their sensitivity and precluding their use for single molecule detection. Furthermore, up to now it has not been possible to integrate the application of force on biomolecules in QCM measurements.

In light of these issues and the analytical power of force-based techniques, herein is described a novel type of instrument using a QCM as a direct mechanical transducer for the response of discrete samples (molecules, particles) placed in a variable force field provided by a standard commercial centrifuge. This *centrifugal force quartz crystal microbalance* (CF-QCM) concept is concerned with direct introduction of pico to nanoscale forces in the liquid phase for analyzing the mechanical properties of biomaterials.

1.2 Historical Perspective

As sensors, QCMs found their initial applications monitoring thin film deposition in the vacuum phase, where it was found that a QCM would exhibit a frequency shift Δf linearly proportional to the adsorbed mass. Such experiments [97] were first carried out by SAUERBREY in the vacuum phase. Known as the *Sauerbrey relation*, the negative proportionality of Δf to adsorbed mass was found to be valid in the regime of sub-monolayer thicknesses of rigidly attached (metal, dielectric) layers.

Initially it was thought that the low Q mechanical resonance of the QCM precluded its use in the liquid phase, however subsequent work published in 1985 by GORDON and KANAZAWA showed liquid phase measurements were indeed possible, extending the treatment of SAUERBREY to encompass viscoelasticity. The relations of GORDON and KANAZAWA, derived from a Butterworth van Dyke equivalent circuit [98], predicted the resonant frequency of the QCM to be sensitive to the density-viscosity product of the liquid in contact with the crystal. In both the gas phase and for viscoelastic materials, the frequency shifts were again always found to be *negative* as a function of increasing mass or density-viscosity.

In the same year as GORDON and KANAZAWA, DYBWAD published a rather elegant experiment [101] in which he looked at the frequency shift of a QCM in air when a single micron-sized gold particle was placed on the sensor surface. Remarkably, DYBWAD

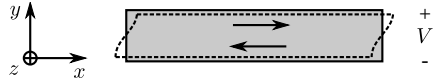


Figure 1.2: Conceptual drawing of a transverse shear wave. An electric potential is applied along the y axis, causing the crystal to shear.

reported a *positive* frequency shift. Dybwad explained the positive frequency shift result with a coupled oscillator model. The coupling between the two systems was mediated by the strength of the contact between the particle and the QCM, which determined the sign of the frequency shift. In the weak coupling regime, the particle was at rest in the laboratory frame while the QCM moved beneath it, and a positive frequency shift was observed. In the strong coupling regime, the QCM and the particle moved together, and the negative frequency shift of SAUERBREY was observed. The coupled oscillator model was more recently developed by JOHANNSMANN, extending the mathematics to encompass heterogenous collections particles in the liquid phase [99].

Further work has been done with nano-indentation probes in the gas phase, particularly by BOROVSKY [102], looking at the influence of micron-sized spherical tips pressed against the sensor surface. When a micron-sized tip is pressed against the QCM surface, the same positive frequency shift as DYBWAD is observed as a function of applied force, which is identified with a lateral (sphere-plate) Hertzian spring constant.

The CF-QCM concept [103] was first proposed by SATO, inspired by a multiplexed optical centrifugal force microscopy technique [104] developed by HALVORSEN and WONG. The present work lies in between that of JOHANNSMANN and BOROVSKY; it is conjectured that the application of force for discrete objects on a QCM will modify the mechanism of coupling which will be observed as a specific feature of the QCM sensorgram.

1.3 Theory

1.3.1 Physical Manifestation

Physically, a QCM is manifest as a thin disc of crystalline quartz, SiO_2 , with metal electrodes deposited on either side (Figure 1.1). The crystalline structure is specifically α -quartz, organized in a trigonal system which is piezoelectric. Typically the crystal employs the “AT-cut” at an angle of 35.25° with respect to the crystallographic axis. In the AT-cut, the vibrational state is dominated by the thickness shear mode, setting up transverse shear waves along the faces of the crystal (Figure 1.2). The AT-cut quartz also has the convenience of a zero frequency temperature coefficient $df/dT = 0$ at 25°C .

When an object is deposited on the crystal surface, the surface acoustic waves will interact with a sample and the resonance frequency of the hybrid system will change. This is the principle of QCM sensing.

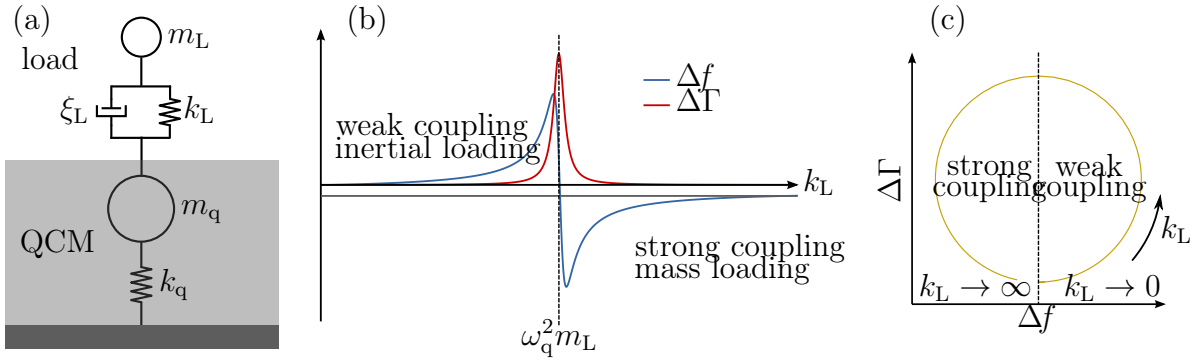


Figure 1.3: Mass-spring-dashpot mechanical model for a QCM under load. In the weak coupling regime the system experiences a positive frequency shift identified with inertial loading, while in the strong coupling regime the system experiences a negative frequency shift identified with mass loading. The fixed relationship between the shift in frequency Δf and bandwidth $\Delta\Gamma$ trace out a circle-like path as a parametric function of k_L .

1.3.2 The Small Load Approximation

A rigorous outline of QCM theory is well beyond the scope of this work. Rather, the introduction of QCM theory will begin much closer to the physics relevant to new results presented herein with what is known as the *small load approximation*. The small load approximation is a statement that for a QCM under load, the *change* in frequency, Δf and bandwidth (half-width at half maximum of the resonance), $\Delta\Gamma$, of a QCM under load are computed by evaluating the ratio of shear stress to speed on the oscillating boundary, according to the relationship [105] [106]

$$\frac{\Delta f + i\Delta\Gamma}{f_F} = \frac{i}{\pi Z_q} Z_L = \frac{i}{\pi Z_q} \left\langle \frac{\sigma}{u} \right\rangle \quad (1.1)$$

where Z_q is the acoustic impedance of AT cut quartz, σ is the stress, u is the speed of the acoustic wave at the boundary, Z_L is the load impedance, f_F is the fundamental frequency, and $\langle \rangle$ denotes an average along the boundary. Since the shear stress is along the x - y plane and the speed along x , all quantities are approximated as scalars. Note that the stress-speed ratio $\langle \sigma/u \rangle$ is dimensionally equivalent to specific acoustic impedance, also called “shock impedance”, sound pressure over speed. In other words, the stress-speed ratio is the impedance of the film. Furthermore, note in Equation 1.1 the common convention of a complex frequency, where Δf represents the maximum of the resonance and $\Delta\Gamma$ the half-width at half maximum of the same resonance distribution.

The small load approximation is a perturbation of the main resonance, and thus is only applicable when the impedance of the load is much smaller than the impedance of the crystal, $Z_L \ll Z_q$, or equivalently $\Delta f \ll f_F$.

1.3.3 Mechanical Model

With the small load approximation in mind, a simple mechanical model based on coupled oscillators is invoked. The arrangement of the mechanical model and the frequency response is shown in Figure 1.3(a). In Figure 1.3, the QCM is represented by a mass m_q on a spring k_q with a fundamental frequency of $\omega_q^2 = k_q/m_q$, and is coupled to a sample load with mass m_L through a parallel spring k_L and dashpot ξ_L representing a Kelvin-Voigt viscoelastic material. The spring and dashpot are not *actual* springs and dashpots, rather they are analogies for the coupling of two systems with different resonances in the small load approximation analogous with $m_L \ll m_q$. The QCM itself has a damping term which is enough to neglect. The spring k_L represents the “stiffness” of the contact — how strongly the particle is coupled to the QCM surface — and the dashpot ξ_L represents energy lost through the coupling.

The coupled system in Figure 1.3, for displacements of m_q by x_q and m_L by x_L , is described by the set of differential equations

$$m_q \ddot{x}_q = -k_q x_q + k_L(x_q - x_L) + \xi_L(\dot{x}_q - \dot{x}_L) \quad (1.2)$$

$$m_L \ddot{x}_L = -k_L(x_q - x_L) - \xi_L(\dot{x}_q - \dot{x}_L), \quad (1.3)$$

which, using an ansatz of $x_q A_q$ and $x_L = A_L e^{i\omega t}$, eigenvalues ω of N_L is a number surface density (number per unit area) for discrete loads.

Using the small load approximation, the response of the system as a function of its coupling k_L is then

$$\frac{\Delta f + i\Delta\Gamma}{f_F} = \frac{N_L}{\pi Z_q} \frac{m_L \omega_q (k_L + i\omega_q \xi_L)}{m_L \omega_q^2 - (k_L + i\omega_q \xi_L)}. \quad (1.4)$$

The mechanical model shown in Figure 1.3(b) has two important regimes as a function of the contact stiffness k_L known as *strong* and *weak* coupling. The strong and weak coupling regimes occur to the left and right of a zero crossing in Δf at $k_{zc} = \omega_q^2 m_L$, and are given asymptotically by

$$\frac{\Delta f}{f_F} = \frac{N_L k_L}{\omega_q \pi Z_q} \quad (\text{weak}, \quad k_L \ll m_L \omega_q^2) \quad (1.5)$$

$$\frac{\Delta f}{f_F} = -\frac{N_L m_L \omega_q}{\pi Z_q} \quad (\text{strong}, \quad k_L \gg m_L \omega_q^2), \quad (1.6)$$

where it is recognized $\Delta\Gamma$ goes to zero in either limit.

The strong coupling regime is identified with mass loading (Sauerbrey [97] behavior) and a *negative* frequency shift linearly proportional m_L . Sauerbrey behavior in the strong coupling regime is most commonly associated with QCM measurements, identified by rigid coupling such that the load takes part in the oscillation of the QCM. In the opposite limit is the weak coupling regime, also called inertial loading [101], which is identified by a *positive* frequency shift independent of the mass and linearly proportional to k_L . In the weak coupling regime, the coupling is sufficiently weak such that the particle remains at rest in the laboratory frame. It is “clamped” by its own inertia [107].

2 | Experimental

2.1 Setup

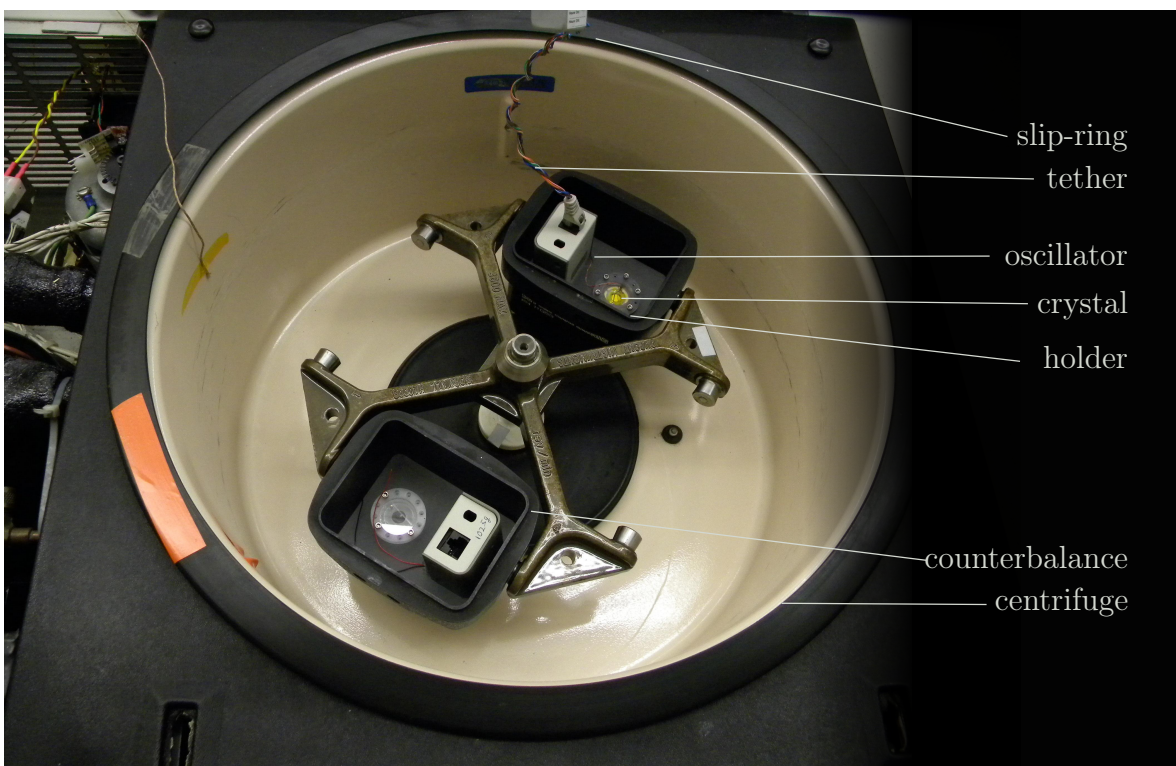


Figure 2.1: Annotated picture of the prototype CF-QCM from above. The centrifuge is a standard swinging bucket type.

The CF-QCM experimental setup is shown in Figure 2.1. It consists of a 25 mm diameter 5 MHz gold-coated crystal in combination with an SRS QCM200 PLL-based driver circuit and an external rubidium frequency standard. The driver circuit and crystal are integrated into the arm of a commercial swinging bucket centrifuge. The QCM is then connected in proximity to a remote driver which is tethered via a slip-ring connector to external data acquisition electronics and a computer. The crystal itself is mounted in a holder such that the centrifugal force F_c is always normal to the surface of the crystal. On the sensing side of the crystal is a 125 μL volume PDMS/glass cell containing the sample. The cell is made of a thin o-ring of PDMS (Sylgard 184, 10:1 ratio, cured 20 min

at 120 °C), outer diameter 25 mm, inner diameter 15.5 mm, in contact with the sensing side of the crystal and covered with 25 mm round № 1 cover glass of nominal thickness 0.15 mm. The non-sensing side of the crystal remains in air and is isolated from the body of the centrifuge.

When in operation, the crystal and cell are mounted in either the *loading* configuration, where the centrifugal force is *in to* the sensing side or, by mounting it upside down, in the *unloading* configuration, where the force is *away from* the sensing side.

In addition to the standard QCM driver output, the computer simultaneously records the angular velocity and internal temperature of the centrifuge itself. The angular velocity is obtained with an optical interrupter switch placed over the spokes of an internal gear, acting as an ersatz wheel encoder. The temperature is obtained with a standard K-type thermocouple. The internal motor of the centrifuge was also interfaced to an external DC power supply whose voltage was set by the same computer, allowing the spin speed and acceleration of the centrifuge to be controlled.

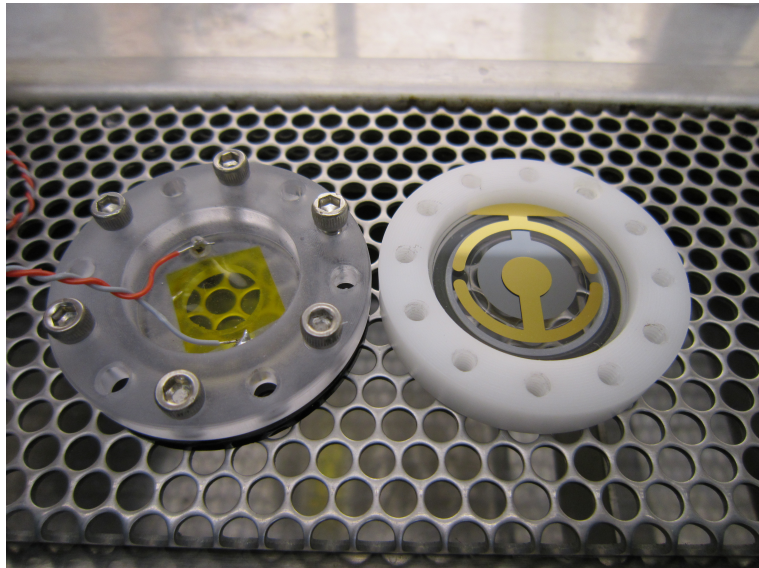


Figure 2.2: Holder for the crystal, shown split into its two halves. The crystal is inside the holder on the right.

2.2 Noise and Comparison to QCM-D

Typical of most QCM circuits, the QCM200 provides an output proportional to Δf , which is used directly in all discussions of Δf . However, unlike a QCM-D device which gives a “dissipation factor”, D , defined in terms of the bandwidth $\Delta\Gamma$ as $D = 2\Delta\Gamma/f_F$, the QCM200 outputs the motional resistance R_m of the Butterworth van Dyke equivalent circuit. R_m is related to the bandwidth Γ and the QCM-D dissipation D by

$$R_m = (4\pi L_m) \Gamma \quad (2.1)$$

$$= (2\pi L_m f_F) D, \quad (2.2)$$

where L_m is the Butterworth van Dyke equivalent motional inductance. Because of the small load approximation, $\Delta f/f_F \ll 1$ and likewise $\Delta L/L_m \ll 1$, L_m can effectively be treated as a constant [108]. The motional inductance L_m is typically in the range of 30 mH [109] [110] to 40 mH [111] [112] [113], with 40 mH being more common and the value used in the present analysis. At $L_m = 40$ mH, the instrument recorded $R_m = 359 \Omega$ in water, which is within 1% of the predicted value [98] of 357 Ω . In this sense, dissipation D and motional resistance R_m are independent but equivalent measures of the QCM bandwidth.

The noise was calculated in Δf and R_m by obtaining the standard deviation of the output signal at constant acceleration. For the SRS QCM200 employed in the experiment the noise was measured at 0.4 Hz (0.008 ppm) for Δf and 0.006 Ω (13 ppm) for R_m , corresponding to a signal to noise ratio of 110 dB. The measured noise is close to the manufacturer's specification [109] of 0.1 Hz for Δf and ± 28 ppm for R_m . The noise was further analyzed for both the loading and unloading orientations of the crystal, as well as for different centrifuge spin speeds. In either case, no discernible difference in the noise was observed. At no point was the centrifuge or bucket assembly modified in an attempt to reduce system noise.

In comparison, a typical QCM-D such as those sold by Q-Sense¹ will have noise of about 0.3 Hz in Δf and 0.2×10^{-6} in D at 5 MHz [114] [115]. Converting from R_m to D and vice-versa, the SRS QCM200 has an equivalent noise in D of 0.005×10^{-6} and the Q-Sense QCM-D an equivalent noise in motional resistance of 0.25 Ω . In terms of $\Delta\Gamma$, the Q-Sense QCM-D has a noise of 0.5 Hz and the SRS QCM200 0.01 Hz. Even though the chosen value for L_m gives R_m within 1% of the predicted value for water, uncertainties in the value of L_m used for the R_m - $\Delta\Gamma$ conversion do not significantly affect the analysis for the range of L_m values quoted in the literature.

It is clear that the SRS QCM200 PLL-based driver and a QCM-D device are both measures of the same underlying physical phenomena taking place in a resonating quartz crystal [108]. It is important to note that the important aspect of the CF-QCM, the centrifugal force, is independent of the type of technique used to drive and monitor the quartz crystal. There is no reason why the CF-QCM technique would not apply to all QCM-based measurement techniques.

2.3 Environmental Effects and Noise

The next chapter presents the response of the CF-QCM under different load situations. Before discussing the various CF-QCM responses, it is prudent to account for all the non-sample phenomena which could influence the sensorgram. Such phenomena have been tabulated in Table 2.1.

From Table 2.1 it is apparent that the dominant source of signal *drift* will be due to the inherent temperature-dependent viscosity of water. This is a good thing, because

¹BiolinScientific / Q-Sense, Hängpilsgatan 7, SE-426 77 Västra Frölunda, Sweden, <http://www.q-sense.com/>

phenomena	response	refs
temperature	8 Hz °C ⁻¹ and 4 Ω °C ⁻¹ in water Third order polynomial with maximum around 24 °C with $a_1 = 2.3888$, $a_2 = -1.8719 \times 10^2$, $a_3 = 4.8587 \times 10^3$, $a_4 = -4.1814 \times 10^4$.	[109] [116]
electric field	negligible	[117]
magnetic field	10 T ⁻¹ for fields smaller than 10 T	[117]
pressure	-2970 Hz cm ² kg ⁻¹ for changes to 2.1 kg cm ⁻² -1458 Hz cm ² kg ⁻¹ (10 MHz crystal)	[116] [118]
mechanical stress	$\Delta f = 1.62g_f^{1.72}$ for two point symmetrical mounting in air	[119]
sedimentation potential		
parasitic capacitance	2 Hz pF ⁻¹ 0.825 Hz pF ⁻¹ (BvD analysis)	[109] []
acceleration	9×10^{-11} /g, depending on orientation 0.021 881 3 Hz/g in air	[120] [121]

Table 2.1: Environmental effects on the QCM resonance frequency.

temperature drift can be a rather slow process compared with other types of signals. Figure 2.3, a parametric plot of g-force verses temperature for a typical 200 s run, provides evidence of this finding for both air and water. In both cases the temperature increases as the centrifuge spins. However, the temperature drifts are extremely small during the course of a run, less than 0.1 °C.

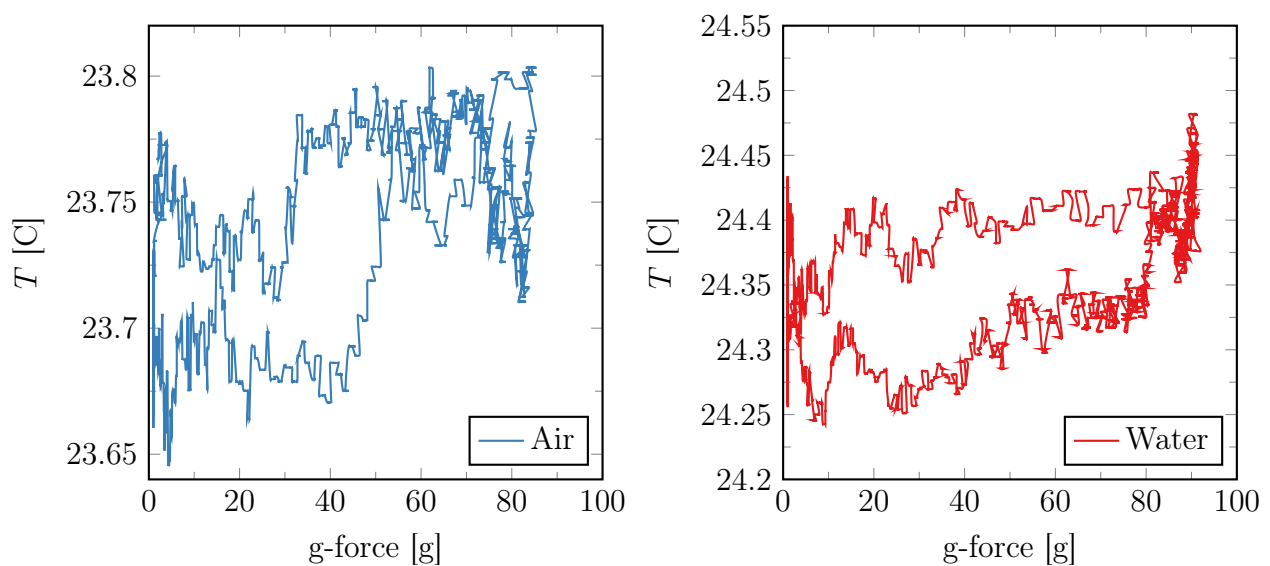


Figure 2.3: Parametric plot showing temperature drift during an experimental run from 0 to 90 g and back, taking 200 s.

3 | Load Situations

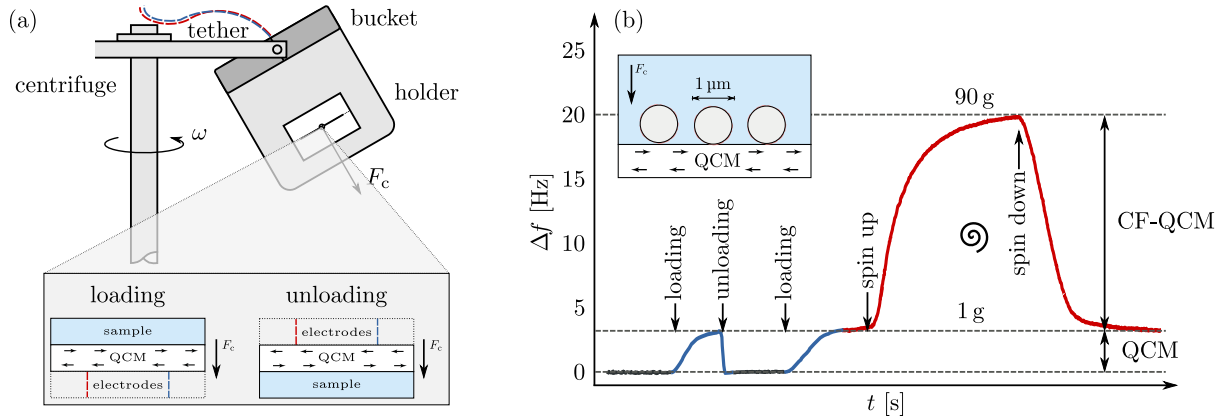


Figure 3.1: Overview of the CF-QCM and its sensorgram. (a) Schematic of the experimental setup. (b) Example CF-QCM sensorgram for a sample consisting of $1 \mu\text{m}$ particles in water, $N_L = 1.58 \times 10^{11} \text{ particle m}^{-2}$, in the “loading” configuration (inset). The horizontal arrows indicate the motion of the QCM’s transverse shear mode.

The central theme of the CF-QCM work is the study of its sensorgram for different load situations. An example of such a load situation is shown in Figure 3.1(b). Here, free $1 \mu\text{m}$ streptavidin coated polystyrene particles in water are introduced into the sample cell. When the cell is rotated to the loading configuration under the influence of gravity alone, the particles fall toward the sensing surface and a positive shift in the QCM’s frequency signal is observed. When the cell is then rotated 180 degrees by hand to the unloading configuration, the particles fall off and the frequency response returns to its original state. Again the cell is rotated 180 degrees to the loading configuration and the positive frequency shift is observed. As the centrifuge spins up towards 90 g, the particles are “pressed” towards the QCM surface and a more than four fold increase in the frequency shift is observed. The centrifuge then spins down and the baseline frequency shift under gravity alone is recovered.

Traditional QCM experiments assume that the inertial properties and rigidity of the sample’s coupling are taken as a fixed parameter (or statistical distribution) under assay. With this approach however, one is only able to obtain discrete values in an otherwise continuous parameter space. Hybrid-QCM experiments involving nanoindenters [102] or AFM probe tips [122] have shown intriguing behavior when force is applied to a sample in a QCM measurement. There have also been reports that accelerations as small as

1 g have a measurable effect on a QCM's response for viscoelastic monolayers such as DNA [123], even for pure Newtonian liquids [124]. All of these responses have been found to be significant compared to the baseline acceleration sensitivity of the QCM itself [125]. With the integration of a centrifuge to a standard QCM, one can observe these effects under enhanced g-forces and make endpoint measurements (measurements taken after the addition of a sample) in the sample's parameter space continuously and repeatedly.

To demonstrate the CF-QCM concept, six different samples were examined under variable accelerations from approximately 1 g to 90 g . The samples were chosen to be examples of the breadth of load situations accessible with the CF-QCM technique. They are:

1. air,
2. deionized water,
3. free particles in water,
4. paramagnetic particles attached to the sensor via short oligonucleotides,
5. 48 kbp lambda phage DNAs attached to the gold electrode, and
6. polystyrene particles tethered to the sensor via 48 kbp lambda phage DNAs.

The quartz crystals are always cleaned before use by immersion in fresh piranha solution (3:1 mixture of 97 % H_2SO_4 and 30 % H_2O_2) for 5 min and rinsed liberally with pure water.

3.1 Air

As a first step, the instrument's response was recorded in air, shown parametrically in Figure 3.2(a). The base acceleration sensitivity (change in frequency versus change in g-force) of AT cut quartz normal to the plane of the crystal has a reported value [126] of $\Delta f/\Delta g = 2.188(6) \times 10^{-2} \text{ Hz g}^{-1}$ (see Table 2.1). The CF-QCM data shows similar behavior: $\Delta f/\Delta g = 2.682(23) \times 10^{-2} \text{ Hz g}^{-1}$ in the loading configuration. The signs of $\Delta f/\Delta g$ are found to be opposite in the loading and unloading configurations. Though no references for the bandwidth or motional resistance dependence of a QCM under acceleration are known, the data predicts a linear relationship of $\Delta\Gamma/\Delta g = 9.203(171) \times 10^{-4} \text{ Hz g}^{-1}$. The slight increase in $\Delta f/\Delta g$ in the unloading situation is attributed to the asymmetric stress caused by the QCM holder under different orientations.

3.2 Deionized Water

Next, deionized water was used as a control sample for measurement in the liquid phase, as shown in Figure 3.2(b). The initial shift in frequency and bandwidth is in agreement

with what is obtained the Kanazawa-Gordon relations [98]

$$\Delta f = -f_F^{3/2} \left(\frac{\rho_L \eta_L}{\pi \rho_q \mu_q} \right)^{1/2} \quad (3.1)$$

$$\Delta R = 2f_F L \left(\frac{4\pi f_F \rho_L \eta_L}{\rho_q \mu_q} \right)^{1/2} \quad (3.2)$$

where ρ_L and η_L are the unknown density and viscosity of the liquid. Substituting in the values for water, $\rho = 1 \text{ g cm}^{-3}$ and $\eta = 1 \text{ mPa s}$, $\Delta f = -714 \text{ Hz}$ and $R = 359 \Omega$, which are close to the measured values of $\Delta f = -716 \text{ Hz}$ and $R = 357 \Omega$. As is evidenced in Figure 3.2(b), the response under centrifugal load is linear and smaller than that of air: $\Delta f/\Delta g = 1.357(24) \times 10^{-2} \text{ Hz g}^{-1}$ and $\Delta \Gamma/\Delta g = 2.865(73) \times 10^{-3} \text{ Hz g}^{-1}$ as found by linear least squares fitting.

It is obvious that acceleration-dependent forces in the liquid phase are not necessarily commensurate with those in the gas phase. However, because the inherent acceleration-dependent signal is small, it does not contribute significantly to the dominant features of the CF-QCM signal for actual loads.

3.3 Free Particles

Utilizing the flexibility that the instrument provides in modifying the coupling between the load and the sensor surface, the technique is applied to the study of discrete micron-sized particles. Free particles (Spherotech SVP-10-5, SVM-15-10, and SVP-200-4), of different diameters were prepared by diluting a solution of $30 \mu\text{L}$ particles in $300 \mu\text{L H}_2\text{O}$. A $125 \mu\text{L}$ aliquot of the $300 \mu\text{L}$ volume was then placed in the PDMS cell in contact with the sensing side of the crystal. The sensing area was calculated to be 1.195 cm^2 . The particles in solution experience a buoyancy, reducing their apparent mass. The surface density N_L was determined as in Figure 3.3 by counting the average number of particles per unit area with a microscope and was found to be within 20 % of the value predicted by the volume concentration.

As first referenced in Figure 3.1(b), the frequency and bandwidth shifts of free particles in the liquid phase as a function of g-force is shown in Figure 3.2(c). Free streptavidin-coated polystyrene particles with mean diameter $\bar{d} = 1.07 \mu\text{m}$ are placed in the sample volume with a surface density of $N_L = 1.58 \times 10^{11} \text{ particle m}^{-2}$, and the signal is observed in both the loading and unloading configurations. The particles did not exhibit adhesion to either the unmodified gold electrode or the glass/PDMS cell surrounding it; in the unloading configuration, the particles quickly drifted away from the sensing area and a signal identical to water was observed. In the loading configuration, a large positive shift in Δf and $\Delta \Gamma$ was observed, consistent with previously observed responses for weakly coupled particles in the micron size range [99].

The initial shift under 1 g was found to be $\Delta f = 2.2 \text{ Hz}$ and $\Delta \Gamma = 7.5 \text{ Hz}$. At the maximum acceleration of 90 g the signal increases to $\Delta f = 16.5 \text{ Hz}$ and $\Delta \Gamma = 37 \text{ Hz}$. This also represents a sensitivity enhancement in the minimum resolvable surface density

of the particles. The scaling of Δf and $\Delta \Gamma$ with increasing centrifugal load is nonlinear in the applied load, implying non-Hertzian behavior [102].

The same experiment was also carried out with 2, 6, 15, and 25 μm polystyrene particles. The loading curves all followed the same trend, but the relative shifts in Δf and $\Delta \Gamma$ differed based on particle size. The results from these loads are summarized in Table 3.1.

Frequency and Bandwidth Shifts				
\bar{d} [μm]	$\Delta f_1/N_L$	$\Delta \Gamma_1/N_L$	$\Delta f_{90}/N_L$	$\Delta \Gamma_{90}/N_L$
1.07 ^p	1.61E-11	3.85E-11	6.98E-11	1.43E-10
1.89 ^m	5.58E-11	6.55E-11	7.90E-10	2.43E-10
5.86 ^m	4.00E-09	3.09E-09	3.43E-10	3.41E-10
15.0 ^p	1.32E-07	6.39E-08	3.99E-08	9.50E-09
24.80 ^p	5.01E-07	1.53E-07	3.26E-07	1.65E-07

Table 3.1: Normalized frequency and bandwidth shifts (in Hz m^2) at 1 and 90 g for various particle sizes in water. The quoted diameter \bar{d} is the sample mean. *p*: polystyrene particles, *m*: magnetite-coated polystyrene.

3.4 Oligo-Attached Particles

In contrast to the situation of free particles, the CF-QCM behavior was also studied in a regime where particles are rigidly coupled to the sensor. Rigid coupling was accomplished by attaching 2 μm (mean diameter $\bar{d} = 1.89 \mu\text{m}$) streptavidin-coated paramagnetic particles modified with biotinylated 25 mer oligos to complementary strands conjugated to the QCM-gold surface via thiol bonds.

To attach oligos to the QCM, they were first immersed in a 1 μM solution of thiolated oligos (5'-ThioMC6-TTT TTT CAC TAA AGT TCT TAC CCA TCG CCC-3') in a 1 M potassium phosphate buffer, 0.5 M KH_2PO_4 , pH 3.8 for 1 h. Next, the sample was immersed in 1 mM 6-Mercapto-1-hexanol (MCH) to block residual reactive sites on the gold electrode. After rinsing, attachment to the prepared particles was done in STE buffer: 1 M NaCl with 10 mM Tris buffer, pH 7.4 and 1 mM EDTA. A complementary strand (5'-biotin-CT CAC TAT AGG GCG ATG GGT AAG AAC TTT AGT-3') was attached to the streptavidin-coated particles. The particles were first washed two times by aliquoting a 100 μL base solution of particles in 100 μL STE buffer, 5000 RPM for 3 min and decanting the supernatant. The particles were resuspended in 20 μL of STE buffer and 10 μg of oligos were added. The mixture was incubated for 15 min at room temperature under slow vortexing, then washed again and resuspended in 100 μL STE buffer. The oligo-attached particle suspension was allowed to attach to the gold surface for 15 min before spinning.

The response for oligo-attached particles is shown in Figure 3.2(d). Note that Δf and $\Delta \Gamma$ are both negative and decrease with centrifugal force in the loading orientation.

When spinning with the oligo-attached particles it is suspected that the presence of the particle is not sensed directly, but rather the sensing is mediated via changes in the conformational state of the oligonucleotide layer. Such an acceleration effect has been observed before [124] [123] but only within the 2 g orientation difference of gravity. When the oligo layer is under centrifugal load, it compresses, causing the density-viscosity product to increase. This behavior is consistent with the behavior of DNA observed on QCMs under the influence of gravity alone [123].

3.4.1 Verification of the Oligo Attachment

The experimental setup provided two separate mechanisms for confirming both the presence of thiolated oligos attached to the QCM gold surface and the rigid attachment of particles to the surface by oligos.

First, with the attachment of oligos the motional resistance of the QCM increased from $R = 357\Omega$ (pure water) to a typical value of about 550Ω for oligos with a standard deviation of 4.3Ω over five different runs. The increase of motional resistance indicates the adsorption of a viscoelastic layer. Second, while observing the sample by eye under a microscope, a handheld neodymium magnet was brought in proximity to the sample. In the absence of the oligo attachment, the particles readily moved away from QCM surface towards the magnet. For samples for which particles were believed to be attached, no such motion was observed.

3.5 Lambda DNA

Moving from particles to viscoelastic monolayers, in Figure 3.2(e), 48 kbp lambda phage DNA in STE buffer were attached to the gold sensor electrode via a complementary thiolated oligo. Lambda DNAs were prepared by combining $50\mu\text{L}$ of lambda DNA at $500\mu\text{g mL}^{-1}$, $5.5\mu\text{L}$ of 10x T4 ligase, and $0.5\mu\text{L}$ of diluted $10\mu\text{M}$ thiolated linker oligonucleotide and heating to 70°C for 5 min. The suspension was left to cool to room temperature as the ligation of the oligos to the DNA COS ends occurred. Once the mixture was at room temperature, $15\mu\text{L}$ 10x ligase buffer, $127\mu\text{L}$ H_2O , and $2\mu\text{L}$ T4 DNA ligase was added to the annealed linker. The reaction was allowed to proceed at room temperature for 3 h. Upon the attachment of the lambda DNA, the motional resistance of the QCM was observed to have increased from its base value of $R = 357\Omega$ for pure water to a typical value of 575Ω . Unfortunately, the surface functionalization of the bare crystal could not be performed *in situ*, and therefore values for Δf are unknown. The QCM200 PLL-based driver reports absolute values for R but relative values for Δf . The instrument has a limited range for Δf , which is set to zero before each experimental run.

Previous studies have shown that, through the use of dissipation monitoring, QCMs are sensitive to not only the adsorbed mass and viscosity, but the physical conformal state (“shape”) of DNAs hybridized to the sensor surface [127]. In the experiment, even though the force on the lambda DNAs is on the order of femtonewtons, a strong linear

decrease ($\Delta\Gamma = -2.9120(95) \text{ Hz g}^{-1}$) in the bandwidth as function of g-force was observed, indicating an increase in viscoelastic loss. However, under larger g-forces the sign of Δf reverses. The origin of the Δf reversal is not understood but could indicate a nonlinear viscoelastic compliance under load. The unloading configuration sees a smaller negative response in $\Delta\Gamma$ with little effect on Δf .

At this point it is important to make an observation about the specific influence of a salt buffer when used in experiments involving DNA. There are several studies [128] [129] regarding the effects of various electrolytic buffer solutions and their concentrations on QCM measurements, including reports of an immersion angle (and therefore gravity) dependence [130]. These reports suggest the immersion angle dependence may be related to the behavior of the interfacial layer and ion transport in monovalent electrolytic solutions in accelerating frames [131] [132]. In the CF-QCM experiment, a significant contribution in the unloading configuration was observed for STE buffer alone ($\Delta f = -0.3260(29) \text{ Hz g}^{-1}$, and $\Delta\Gamma$ nonlinear), which was subsequently “screened” [133] by the presence of both oligos and lambda DNAs, making the effect negligible in the current set of experiments. Further investigation is required to explain this precisely.

3.6 Tethered Particles

With the sensitivity to both particles and monolayers, the instrument raises a possibility for using beads tethered by lambda DNA as a transduction mechanism to investigate its kinetics. One such example is shown in Figure 3.2(f). Streptavidin-coated polystyrene particles with a mean diameter of $24.8 \mu\text{m}$ were tethered to the CF-QCM by means of a 48 kbp lambda phage DNA. Experiments were done in STE buffer whose density reduced the maximum force the bead could exert to about 40 pN which, according to the worm-like chain model [93], should almost fully extend the lambda DNA to a length of $16 \mu\text{m}$.

In addition to the streptavidin-coated polystyrene particles, visual confirmation of attachment was made by eye with a microscope, magnet, and paramagnetic particles in the same way as was done for the free particles.

Though the instrument has not yet been developed enough to make accurate quantitative measurements of tethered particles, the behavior of the data is a clear indication of its potential. As the tethered bead extends the DNA under centrifugal force, Δf increases and $\Delta\Gamma$ decreases. In the case where the DNAs are trapped and pushed between the bead and the surface, both Δf and $\Delta\Gamma$ increase. The signs of the shifts were confirmed with $10 \mu\text{m}$ and $6 \mu\text{m}$ paramagnetic particles, using a magnet to either pull or push the particles toward or away from the sensor surface. The observed behavior was distinct from either the case of lambda DNA or free particles alone.

At $F_c = 40 \text{ pN}$, the frequency shift indicates an effective decrease in the density-viscosity product of 10 % or about 1.5 pg . For the surface densities involved ($N_L = 3.25 \times 10^7 \text{ particle m}^{-2}$), the equivalent interfacial mass lost for a fully extended lambda DNA predicted by the worm-like chain model are in the picogram range and cannot account for the more than 10^6 signal difference shown. If indeed the response is due to lambda DNA extension, fu-

ture experiments involving high frequency, large centrifugal force CF-QCMs could easily detect the kinetics of a single tether.

3.7 Particle Sizing

The coupled oscillator model (Equation 1.4), when analyzed for samples of free particles (Figure 3.1(b), Figure 3.2(c), and Table 3.1), suggests an avenue to allow QCMs to determine the size of large micron-sized particles in the liquid phase. Thus far this has only been possible with nanometer-sized particles which lie within the QCM's shear acoustic wave [134]. If one plots Δf versus $\Delta\Gamma$ in Equation 1.4 as a parametric function of k_L , the points are found to lie on a circle with radius r_L (see Figure 1.3).

Making the approximation $\xi_L \ll k_L$, and that the damping is small, $\xi_L \ll 1$, the radius is found to be

$$\frac{r_L}{f_F} = \frac{N_L}{\pi Z_q} \frac{(m_L \omega_q)^2}{2\xi_L} \sqrt{1 + \left(\frac{\xi_L}{m_L \omega_q}\right)^2} \quad (3.3)$$

$$\approx \frac{N_L}{\pi Z_q} \frac{(m_L \omega_q)^2}{2\xi_L}, \quad \text{for } \xi_L \ll 1. \quad (3.4)$$

In considering the parametric representation of Δf and $\Delta\Gamma$, the physical mechanism modifying k_L is removed from the problem. If a circle is fitted to the experimentally observed Δf - $\Delta\Gamma$ data (again, plotted parametrically as a function of g-force), its behavior can be extrapolated to the strong coupling regime by finding the point at which $\Delta\Gamma = 0$ and $\Delta f < 0$. Knowing Δf , Equation 1.6 can then be inverted to solve for either number density or particle size/mass. An example of the fitting procedure is shown in Figure 3.4 using the same data for 1 μm particles shown in Figure 3.1 and Figure 3.2. Inset is a table for the same predictions done for particles with known diameter $\bar{d}_{\text{actual}} = 1, 2, 15, \text{ and } 25 \mu\text{m}$. In all cases the surface density was known and the diameter $\bar{d}_{\text{predicted}}$ was derived from the mass m_L , found by inverting Equation 1.6. The results are surprisingly accurate despite the exploratory nature of the instrument's construction. It should also be mentioned that with knowledge of the way in which the g-force modifies k_L , the frequency zero crossing at $k_{zc} = \omega_q^2 m_L$ can be used to determine the mass m_L without knowledge of the number density N_L .

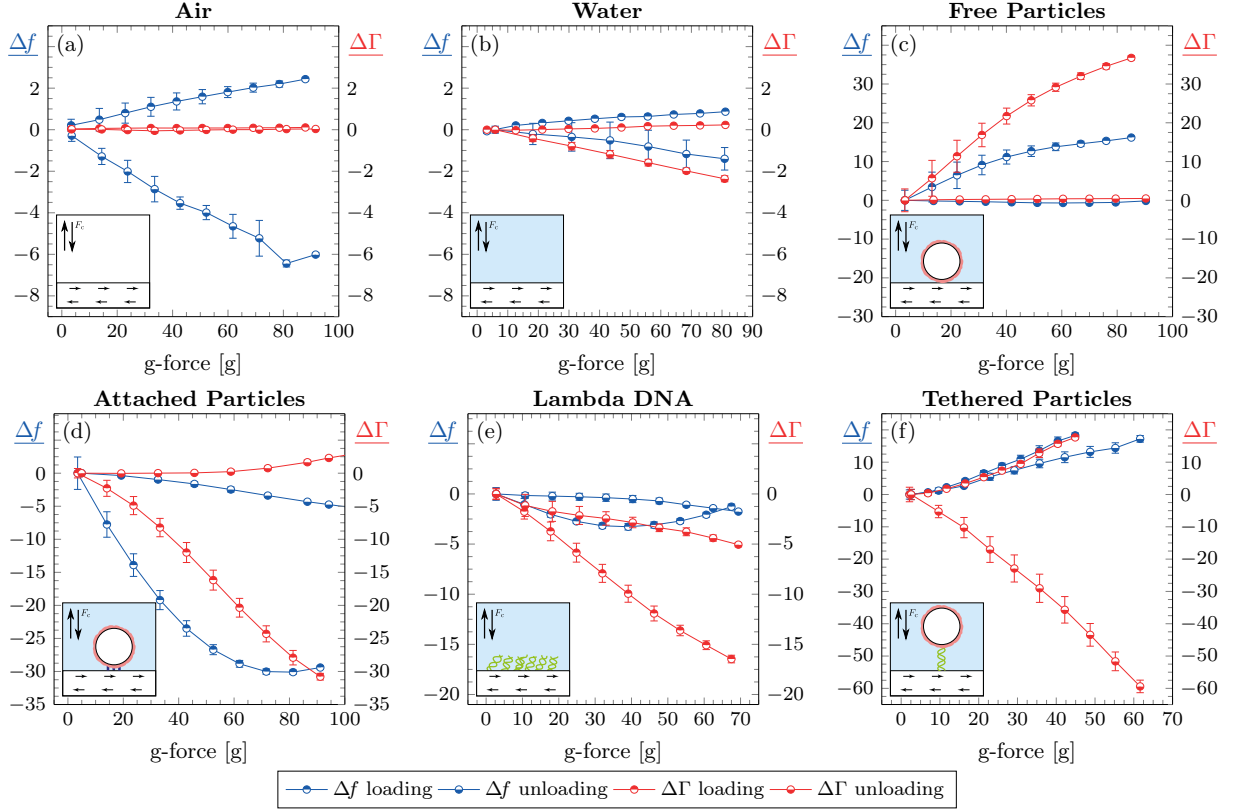


Figure 3.2: Load situations. Change in frequency Δf and bandwidth $\Delta \Gamma$ (in hertz, inferred from motional resistance) of the CF-QCM under different load situations as the centripetal acceleration is directed into (*loading*, represented by circles with the top half colored) and out of (*unloading*, represented by circles with the bottom half colored) the plane of the crystal. The situations are (a) unloaded crystal in air, (b) deionized water, (c) free $1\text{ }\mu\text{m}$ diameter streptavidin-coated polystyrene particles, $N_L = 1.58 \times 10^{11}\text{ particle m}^{-2}$, (d) $2\text{ }\mu\text{m}$ diameter streptavidin-coated paramagnetic particles, $N_L = 1.65 \times 10^{10}\text{ particle m}^{-2}$, attached with 25 mer oligonucleotides, (e) lambda DNA only attached to the gold electrode, and (f) $25\text{ }\mu\text{m}$ diameter streptavidin coated polystyrene particles, $N_L = 3.25 \times 10^7\text{ particle m}^{-2}$, tethered to the sensor surface with 48 kbp lambda DNAs. Error bars are derived from uncertainties (standard deviation) in the centrifuge both spinning up and spinning down in a single experimental run.

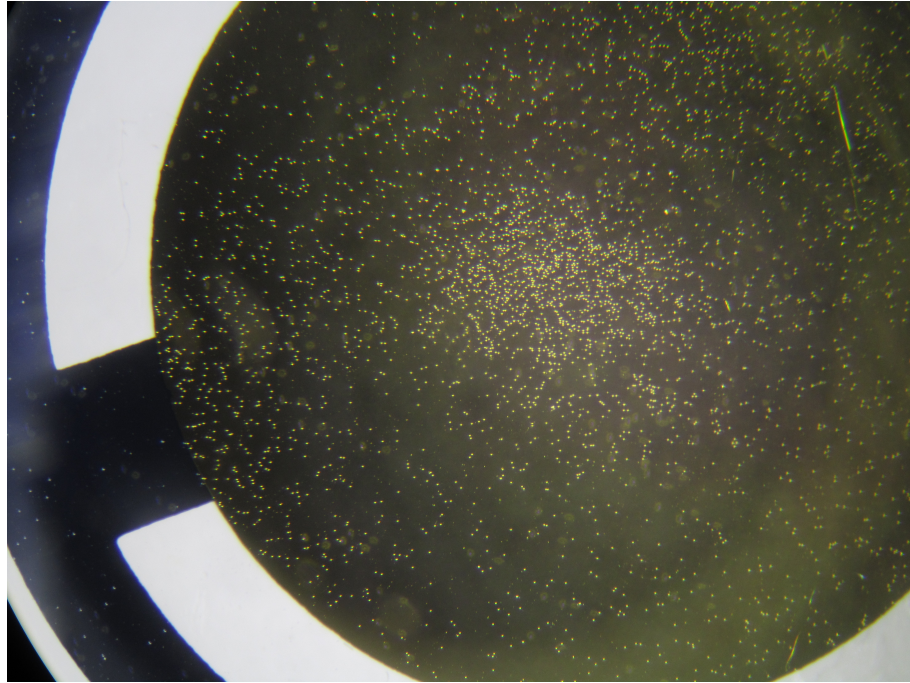


Figure 3.3: Free particles on the surface of the QCM. The particle number density N_L was determined by manually counting particles imaged in a microscope and dividing by the corresponding area.

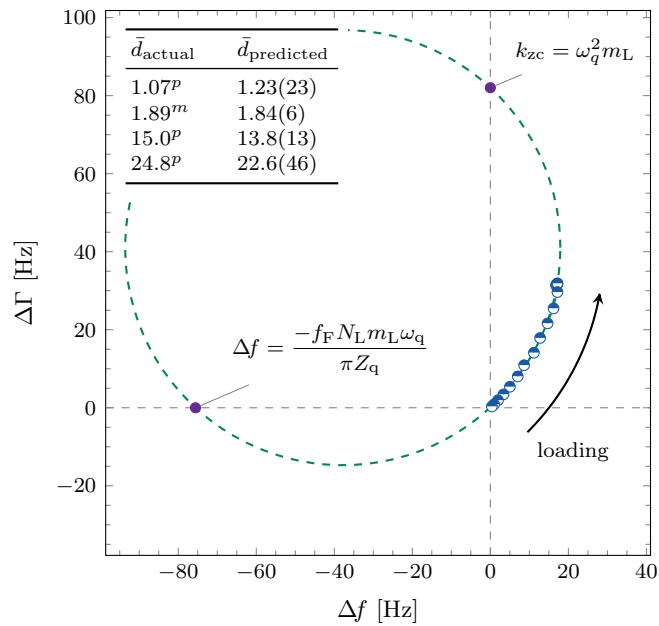


Figure 3.4: Particle sizing. Method for sizing micron-sized particles using the CF-QCM. Δf versus $\Delta \Gamma$ is plotted parametrically as a function of g-force, and the data is fit to a circle. The point on the circle for which $\Delta \Gamma = 0$ and $\Delta f < 0$ provides an estimate of mass adsorption and thus particle size. Results for particles with diameters $\bar{d}_{\text{actual}} = 1, 2, 15$, and $25 \mu\text{m}$ are shown in Table 3.1. Fit circle has a radius of 55.77 Hz and a center of $(-37.83, 41.05)\text{Hz}$.

4 | Simulation

4.1 Introduction

4.2 Finite Element Modeling

A finite element simulation was carried out using the software **COMSOL Multiphysics** 4.3 (4.3.0.233) (Comsol Inc., Burlington, MA). Though the source code of COMSOL is not available for scrutinous review, the following implementation is generic and may be carried out using other software (e.g. **OpenFOAM** [135], **SU2** [136]). Unless otherwise stated, implementation specific information is applicable to **COMSOL**.

The simulation is done by solving the steady state incompressible Navier Stokes equations, neglecting turbulence, using finite element analysis in two dimensions

$$\rho (\dot{\mathbf{u}} \cdot \nabla) \dot{\mathbf{u}} = \nabla \cdot \left(-\rho \mathbf{I} + \eta \left(\nabla \dot{\mathbf{u}} + (\nabla \dot{\mathbf{u}})^T \right) \right) + \mathbf{F} \quad (4.1)$$

$$\rho \nabla \cdot \dot{\mathbf{u}} = 0 \quad (4.2)$$

where $\dot{\mathbf{u}}$ is the flow velocity field, ρ is the fluid density, $\eta = \eta' + i\eta''$ is the complex dynamic viscosity, \mathbf{I} is the identity matrix, and \mathbf{F} is the body force per unit volume. The computational domain is set up as shown in Figure 4.1.

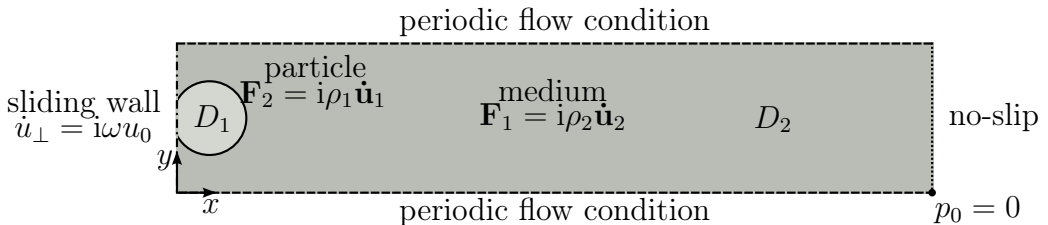


Figure 4.1: Two-dimensional computational domain for the finite element simulation.

It is important to note that, because the simulation is two-dimensional, what is actually simulated are infinite cylinders rather than spheres. For Sauerbrey-type viscoelastic films, the difference between two- and three-dimensional simulations is negligible. However, for asperity contacts such as spheres the results, however qualitatively correct, did not always result in exact numerical agreement with experiment [137]. An extended simulation in three dimensions is warranted.

The left hand (---) is a sliding wall given a tangential velocity of

$$\dot{\mathbf{u}} = \begin{pmatrix} \dot{u}_x \\ \dot{u}_y \end{pmatrix} = \begin{pmatrix} \dot{u}_{\parallel} \\ \dot{u}_{\perp} \end{pmatrix} = \begin{pmatrix} 0 \\ i\omega u_0 \end{pmatrix} \quad (4.3)$$

where $\omega = 2\pi f$ is the angular frequency of oscillation, $u_0 = 1 \times 10^{-2}$ nm is the amplitude, $\dot{u}_x = \dot{u}_{\parallel} = 0$ is the parallel velocity component, and $\dot{u}_y = \dot{u}_{\perp} = i\omega u_0$ is the tangential velocity component. The top and bottom boundaries (----) are given a periodic flow condition such that their pressure difference is zero. The right-hand side (-----) has a zero-slip condition. The two materials 1, the particle, and 2, the medium in domains D_1 and D_2 are assigned a volume force $\mathbf{F} = i\omega\rho\dot{\mathbf{u}}$, where ρ is the density of the material, (e.g. $\rho_1 = 1.06 \text{ g cm}^{-3}$ for polystyrene and $\rho_2 = 1 \text{ g cm}^{-3}$ for water). Finally, an initial pressure point constraint of $p_0 = 0$ is assigned to the point in the bottom right of the domain.

The sphere (or, more appropriately, cylinder, since the simulation is two-dimensional) is domain D_1 with diameter d and radius r and is located a distance $s > -r$, measured from the bottom of the sphere, from the oscillating boundary. If $s > 0$, the sphere does not make contact with the boundary. If $s \leq 0$, the sphere is truncated at the boundary resulting in a finite contact radius r_c ; this truncation is identified with a finite contact radius r_c in terms of contact mechanics. It is useful to sample in either domain, so either r_c or s is swept, converting between them with

$$r_c(s) = \sqrt{2r - s} \sqrt{s} \quad (4.4)$$

$$s(r_c) = \left(r - \sqrt{r^2 - r_c^2} \right) \operatorname{sgn}(r_c). \quad (4.5)$$

The number density N_L was controlled by increasing or decreasing the height of the domain proportional to the size of the sphere.

The materials in the simulation are assigned a complex dynamic viscosity $\eta = \eta' - i\eta''$. The complex dynamic viscosity is related to the complex bulk modulus $G = G' + iG''$ by

$$\eta = \frac{G}{i\omega} \quad (4.6)$$

and the loss tangent, the angle of the complex phasor relative to the real axis is

$$\tan \delta = \frac{G''}{G'}. \quad (4.7)$$

Specific to the stationary solver in COMSOL, in the **Study**→**Stationary Solver**→**Advanced** window, “Allow complex-valued output from functions with real input” was checked. Enabling complex-valued output, coupled with the complex-valued input for the body forces produced shear waves in the simulation.

The mesh settings were calibrated in COMSOL for fluid dynamics with a maximum mesh size of 1×10^{-9} m along the oscillating boundary. All other meshes were generated automatically. As for the size of the computational domain, we find that a height (parallel to the oscillating boundary) of $h = 2d$ and width (tangential to the oscillating boundary) $w = 2d$, minimum of 500 nm, produces consistent results with a minimum of error and computational resources.

4.2.1 Extracting Shifts

Shifts in frequency, Δf , and bandwidth (half-width at half maximum), $\Delta\Gamma$, are computed by evaluating the stress-speed ratio of the oscillating boundary according to the relationship

$$\frac{\Delta f + i\Delta\Gamma}{f_F} = \frac{i}{\pi Z_q} Z_L = \frac{i}{\pi Z_q} \left\langle \frac{\sigma}{\dot{u}_\perp} \right\rangle \quad (4.8)$$

where σ is the complex stress, \dot{u}_\perp is the complex tangential velocity component, Z_L is the load impedance, and $\langle \rangle$ denotes a line average along the boundary. In COMSOL, and in the coordinates of Figure 4.1, σ is **Total stress**, y component (v) and \dot{u} is **Velocity field**, y component, ($spf.T_stressy$). As in Equation 1.1, note again that the stress-speed ratio $\langle \sigma/\dot{u} \rangle$ is dimensionally equivalent to specific acoustic impedance, also called “shock impedance”, sound pressure over tangential velocity; the stress-speed ratio is the impedance of the film.

4.2.2 Verification Examples

The validity of the numerical simulation was checked against two results for which the response is well known: the extension of a shear evanescent wave beyond the oscillating boundary and the complex frequency shifts in the presence of viscoelastic media.

Shear Evanescent Wave

The finite element simulation when set up as described in Section 4.2, predicts a shear evanescent wave out from the tangentially oscillating boundary. The predictions from the finite element simulation closely match theory [138], shown in Figure 4.2. The theoretical expression for the shear evanescent wave is taken as [138]

$$\frac{u(x)}{u_0} = \exp \left(-\sqrt{\frac{i\rho\omega}{\eta}} x \right), \quad (4.9)$$

where x is the spatial extension from the tangentially oscillating boundary in the coordinates of Figure 4.1. The 1/e penetration depth δ is

$$\delta = - \left(\Im \left(\sqrt{\frac{\rho\omega}{i\eta}} \right) \right)^{-1}. \quad (4.10)$$

In Equation 4.10, \Im represents a function returning the imaginary component of a complex variable.

With the material properties of water, $\rho = 1 \text{ g cm}^{-3}$ and $\eta = 1 \text{ mPa s}$, Equation 4.10 predicts $\delta \approx 252 \text{ nm}$, in good agreement with the simulation data shown in Figure 4.2.

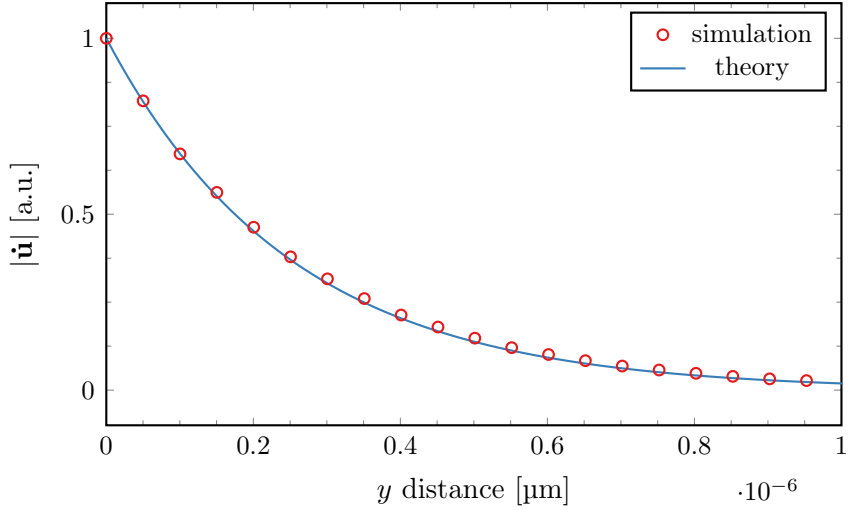


Figure 4.2: Finite element prediction of a shear evanescent wave at 5 MHz in a liquid with $\rho = 1 \text{ g cm}^{-3}$ and $\eta = 1 \text{ mPa s}$, compared with theory (Equation 4.14).

Semi-Infinite Viscoelastic Medium

A semi-infinite medium will produce a complex response described by [98] [139], valid for crystals with one side in contact with a viscoelastic material,

$$\frac{\Delta f + i\Delta\Gamma}{f_F} = \frac{i}{\pi Z_q} \sqrt{\rho G} \quad (4.11)$$

$$= \frac{1}{\pi Z_q} \frac{(-1+i)}{\sqrt{2}} \sqrt{\omega \rho \eta}. \quad (4.12)$$

In terms of the complex dynamic viscosity and shear modulus, Equations 4.11 and 4.12 can be expressed as

$$\frac{\Delta f + i\Delta\Gamma}{f_F} = \frac{i}{\pi Z_q} \frac{(-1+i)}{\sqrt{2}} \sqrt{\rho \omega (\eta' - i\eta'')} \quad (4.13)$$

$$= \frac{i}{\pi Z_q} \sqrt{\rho (G' + iG'')}. \quad (4.14)$$

The simulation geometry was set as described in Figure 4.1 but without D_1 (no cylinder). Extracted values of Δf and $\Delta\Gamma$ are presented in Figure 4.3 as a function of the viscosity η of medium 2. In Figure 4.3(a) η' is swept for a Newtonian fluid, $\eta'' = 0$. In Figure 4.3(b) a non-Newtonian sample is modeled; $\eta' = 1 \text{ mPa s}$ and η'' is swept. The excellent agreement with theory demonstrates that the simulation is applicable for a wide range of materials.

It is of note that the Navier-Stokes approach (which solves for $\dot{\mathbf{u}}$) does not converge in the limit of a perfectly elastic material, e.g. $G = G'$ or $\eta = \eta''$; these systems are typically solved for \mathbf{u} . It is perhaps possible to couple these two domains, but we have not attempted to do so.

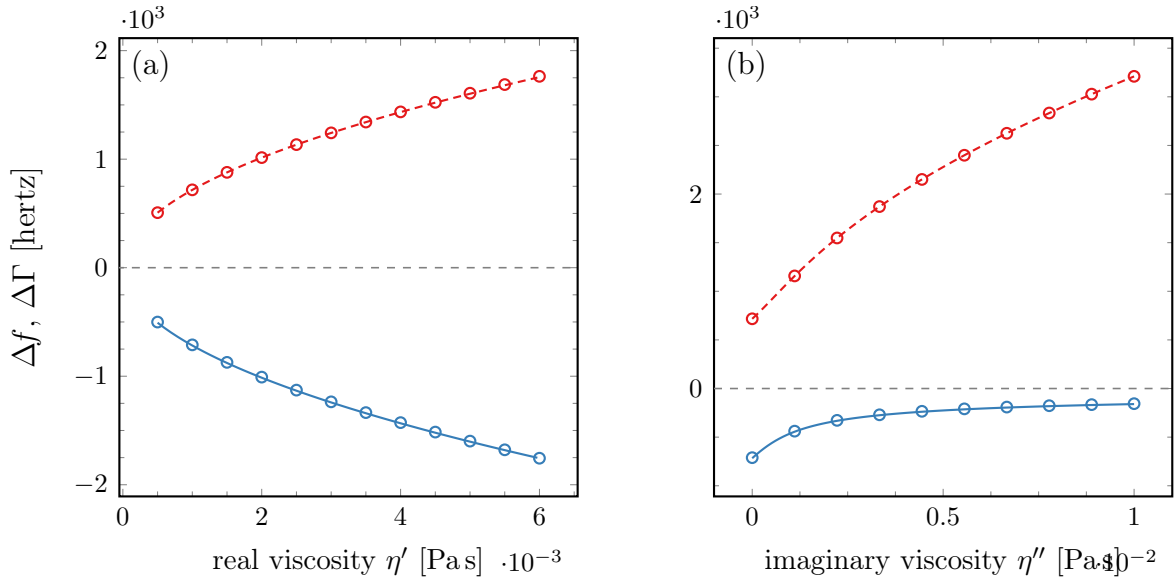


Figure 4.3: Comparison of Δf and $\Delta\Gamma$ versus viscosity η for both the finite element simulation and Equation 4.12. (a) $\eta'' = 0$ and η' is swept (a Newtonian liquid). (b) $\eta' = 1$ mPas and η'' is swept.

4.3 Analysis and Prediction

4.3.1 Particles

A plot of the simulated response in frequency and bandwidth for a $10\text{ }\mu\text{m}$ particle is depicted in Figure 4.4. The spheres were modeled as polystyrene cylinders with density $\rho = 1.06\text{ g cm}^{-3}$, shear modulus $|G_L| = 1.3\text{ GPa}$, and loss tangent $\tan \delta = 0.001$. The cylinders are in water with density 1.0 g cm^{-3} and viscosity 1.0 mPa s . The shifts in Δf and $\Delta\Gamma$ are plotted as a function of a dimensionless contact surface density A_c , defined as the contact area of the sample per unit area on the oscillating boundary.

The behavior of the simulation closely matches experimental observations. As the cylinder approaches and makes (weak) contact with the oscillating boundary, a *positive* shift in both frequency and bandwidth is observed. As the contact radius increases, the cylinder becomes more strongly coupled to the boundary. The amount of energy dissipated into the particle increases until $\Delta\Gamma$ reaches a maximum and Δf experiences a zero crossing. The limiting case sees a rigid attachment and the common *negative* frequency shift proportional to mass adsorption takes hold.

There are two aspects of the simulation that deserve additional consideration:(1) positive shifts in Δf and $\Delta\Gamma$ begin before physical contact with the oscillating boundary and (2) for smaller particles $\Delta\Gamma > \Delta f$ while for larger particles $\Delta f > \Delta\Gamma$.

The experiment shows the same behavior, as evidenced in Table 3.1. However, it should be noted that the procedure of truncation and its interpretation as finite contact radius in the

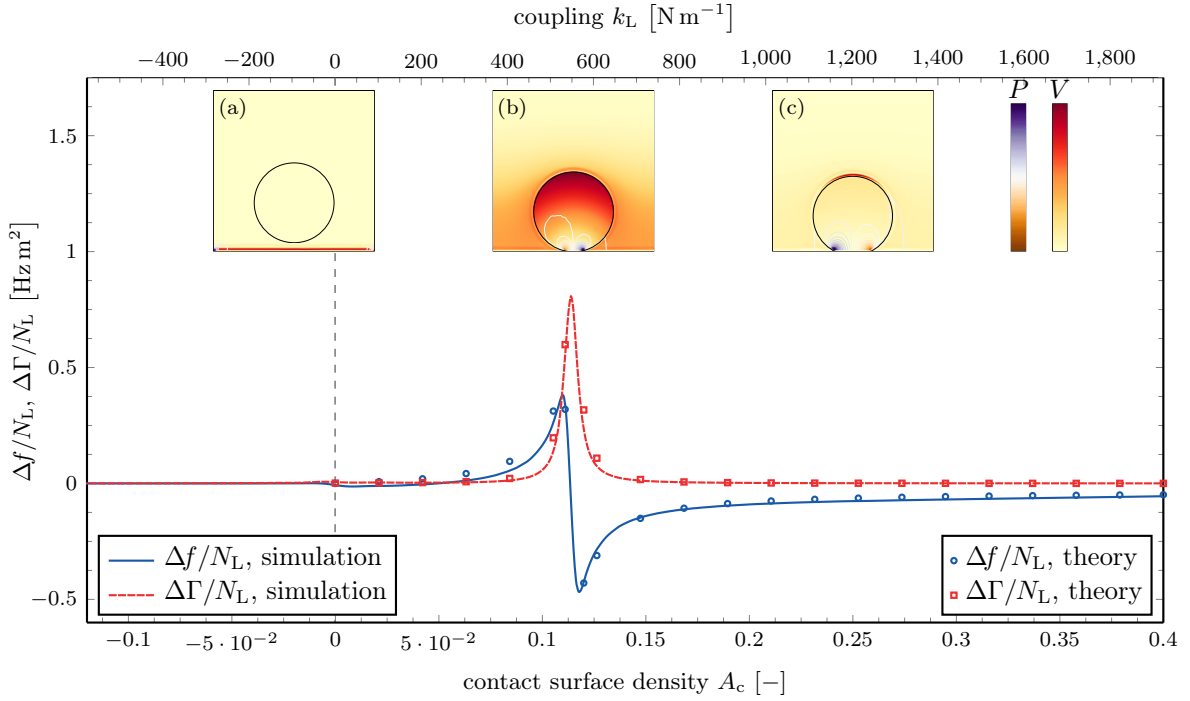
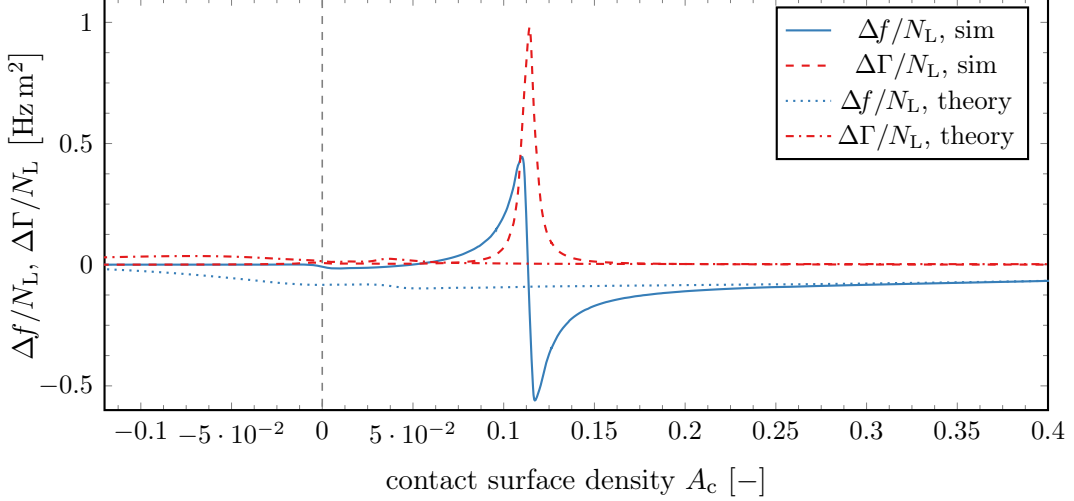


Figure 4.4: Simulation of the CF-QCM behavior. Finite element simulation for a $10\text{ }\mu\text{m}$ polystyrene sphere (cylinder in 2D) as a function of contact surface density A_c . Negative values of A_c indicate positive separation from the surface. Discussion in the text. (a-c): Density plot of the pressure P and velocity U distributions. Units are normalized. Note that in all situations with finite contact radius, stress is annularly distributed around the edge of the contact as per the Mindlin model [3]. (main plot): Shifts in Δf and $\Delta\Gamma$. Points on the plot are a best fit of the mechanical model, Equation 1.1, to the simulation.

framework of contact mechanics utilized on discrete objects are more accurate for larger particles ($10\text{ }\mu\text{m}$, as shown in Figure 4.4) than smaller ones. The accuracy discrepancy is explained in the following way. It is known in the context of DVLO¹ theory [140] that a micron-sized polystyrene sphere in water near a similarly charged gold surface will experience a repulsive force due to electrostatic double-layer effects [141] [142]. The balance between electrostatic double-layer effects and the gravitational force determines the height at which the particle will be at equilibrium above the surface. For the relevant material parameters [140] [143] it is found that, even at 90 g , the smaller 1 and $2\text{ }\mu\text{m}$ particles never make contact with the surface but “hover” at separations of approximately $0.3\text{ }\mu\text{m}$ to $0.15\text{ }\mu\text{m}$. At nonzero separations it is posited that the sphere-surface coupling, being mediated by a viscous liquid, will be dominated by loss, hence $\Delta\Gamma > \Delta f$. On the other hand, larger particles ($\sim 10\text{ }\mu\text{m}$ and above) with significant mass will overcome the double-layer forces and make contact with the QCM through a finite contact radius. In this case the coupling losses decrease and $\Delta f > \Delta\Gamma$.

¹Derjaguin, Landau, Verwey and Overbeek



4.3.2 Sample Viscoelasticity

Finally, a comment on the potential of the CF-QCM technique to be sensitive to different specific viscoelastic properties of discrete samples. While the mechanical properties seen in biomaterials spans an enormous range [144], three general categories were chosen to highlight potentially interesting sensor responses. As per Figure 4.5 these are: cells [145], agarose microparticles [146] [147], and protein microcrystals [148]. Each is treated in the finite element simulation as a discrete sphere, with complex shear modulus $G_L = G'_L + G''_L$, where G'_L is the storage modulus related to elasticity, and G''_L is the loss modulus related to viscosity. G_L is related to viscosity η_L by $\eta_L = G_L/(i\omega_q)$. The shifts in frequency Δf and bandwidth $\Delta \Gamma$ are again plotted as a function of the dimensionless contact surface density A_c . A fictitious negative A_c is identified with a finite separation distance from the simulated QCM surface. In all cases the coverage ratio was 50%, and furthermore it is assumed that centrifugal force will act to “push” the sample into the QCM surface, increasing A_c and thus the rigidity of its contact with the QCM.

As can be seen, the simulated response of the CF-QCM is markedly different in each case. Cells, shown in Figure 4.5(a), are assigned a shear modulus of $G_L = (10 + 50i) \text{ kPa}$ [145] [149] and density ρ_L equal to the surrounding liquid medium. The high loss modulus and low storage modulus predict the cell will exhibit shifts characteristic of a viscous fluid. Likewise, the simulation shows Δf and $\Delta \Gamma$ decrease and increase linearly proportional to the contact parameter, beginning before physical contact occurs. The proportionality is a simple function of the shear modulus and density in the semi-infinite approximation [150] [98]

$$\frac{\Delta f + i\Delta \Gamma}{f_F} = \frac{i}{\pi Z_q} \sqrt{\rho_L G_L} (A_c) \quad (4.15)$$

Cells in and of themselves span a large range of viscoelastic properties which have been demonstrated to be predictive for diseases such as cancer [151]. If one knows the way with which A_c is modulated by an applied force (e.g. viscoelastic compliance), linear fitting to the CF-QCM response will recover G_L or ρ_L .

Next, Figure 4.5(b) shows the simulated response of agarose microparticles with a complex

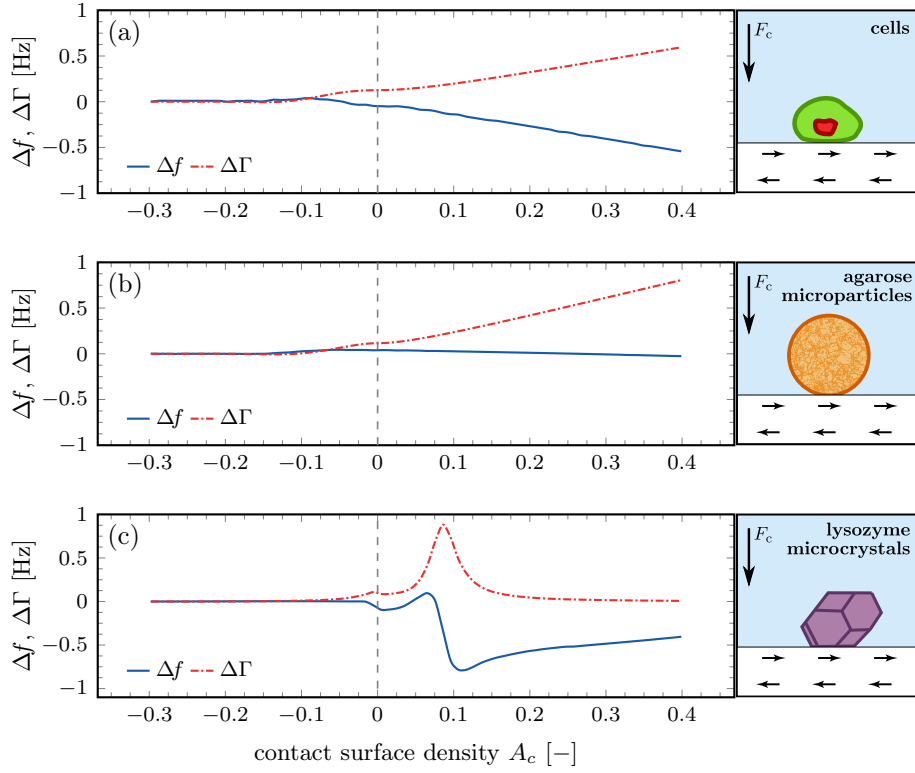


Figure 4.5: Simulated response for different materials. Finite element simulation of normalized Δf and $\Delta \Gamma$ for three categories of samples as a function of contact surface density, A_c . Negative values of A_c indicate the sample has not made contact with the sensor surface. The samples are (a) cells, $G_L = (10 + 50i)$ kPa, (b) agarose microparticles, $G_L = (78 + 78i)$ kPa and (c) lysozyme microcrystals, $G_L = (0.659 + 0.235i)$ GPa.

shear modulus of $G_L = (78 + 78i)$ kPa [152] [153]. Again the density was assumed to be the same as the surrounding medium. Similar to the viscous behavior of cells, $\Delta \Gamma$ decreases linearly with A_c . However, in the simulated agarose microparticles, an equally large elastic term, G'_L , precludes the equally linear decrease in Δf seen for cells. Instead, Δf increases slightly before contact and decreases slightly.

At the end of the spectrum, Figure 4.5(c) are lysozyme microcrystals. These microcrystals are “hard”, having been assigned a complex shear modulus of $G_L = (0.659 + 0.235i)$ GPa [148] [154]. The simulated response of these is similar to what is experimentally observed with polystyrene microparticles ($G_L = 1.3$ GPa). When the microcrystal enters the acoustic evanescent wave, there is an initial negative shift as the effective viscosity-density product increases. At small contact parameters there is a positive shift in Δf and $\Delta \Gamma$. Increasing the contact parameter, $\Delta \Gamma$ sees a maximum and Δf a zero crossing. As the microcrystal becomes strongly coupled to the QCM, the familiar negative Δf is recovered which, as in Figure 3.4, can be used to determine the particle size or mass.

5 | Conclusions

We have observed the QCM sensorgram under the influence of centrifugal force for samples such as DNA monolayers, free discrete polystyrene particles, and particles tethered to the QCM electrode with lambda DNA. We present simulations and a theoretical framework to interpret the QCM signals in the context of the sample's properties.

The data presented thus far points to an interesting avenue for the investigation of force on biomolecules using a quartz crystal microbalance. In addition to the data discussed, we have also observed other types of signals in some of our datasets within the overall trend shown here, which we suspect may be related to ionic transport [131] [132], the conformal state of DNA, and nonlinear viscoelastic behavior. Objects such as microparticles attached or tethered to a biopolymer on the QCM surface become inertial transducers through which one can extract mechanical and thermodynamic properties of the macromolecules. Furthermore, the technique is applicable to microscopic biological objects such as viruses, bacteria, and cells where measurements of mechanical properties and their changes have been directly linked to disease [155] [156] [157].

Enhanced signals for most samples under centrifugal load points to some interesting possibilities for further research in state of the art QCM biosensors. This is true even with the present state of our instrument, which is limited to low-g regimes when compared to other commercial centrifuges. With operation below 90 g, we have observed sensitivity increases corresponding to changes of 10 % in the density-viscosity product for viscoelastic loads and up to a factor of 10 increase in sensitivity for discrete particles. However, there is no technical reason why future incarnations could not spin much faster and considerably clarify the CF-QCM sensorgram. It might also be possible to use this platform in other related modalities such as the nanotribological effects of sliding friction [158] caused by orienting the crystal at an angle to the applied centrifugal force, propelling biomolecules across the surface.

A | Appendix

A.1 Bluestein's FFT Algorithm

It has become all but standard to assume that when Fourier transforms of real data are carried out in a work, the author has used the fast Fourier transform [159] [160]. This work has adopted a different and much more powerful convention which is briefly described herein.

The Fast Fourier Transform

Recall that for a finite number of sampling points, the discrete Fourier transform (DFT) maps a set of discrete complex input data $x = \{x_1 \dots x_n : x_n \in \mathbb{Z}\}$ onto a set of discrete complex output data $X = \{X_1 \dots X_k : X_k \in \mathbb{Z}\}$. This is defined by the formula

$$X_k = \sum_{n=1}^N x_n e^{i2\pi kn/N}, \quad k = 1, \dots, N. \quad (\text{A.1})$$

Direct computation of a DFT is of $O(N^2)$ complexity for N sampling points. However, if the DFT data is linearly sampled, a fast Fourier transform (FFT) can be used. The FFT is able to compute sums of the form of Equation A.1 in $O(N \log N)$ time. The “cost” of this computational efficiency is that the sampling of X_k is fixed according to the sampling of x_n .

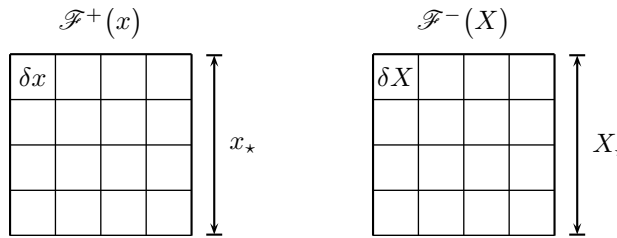


Figure A.1: Coordinates in the fast Fourier transform.

Because of this, there is a symmetric set of relationships for the mapping $x_n \mapsto X_k$ (and vice versa) in the FFT. For example, assume one obtains N samples of x with bounds

x_1 and x_N . The spacing δx between x_n and x_{n+1} is just the range (denoted by a \star) $x_\star = x_N - x_1$ divided by the number of samples, N ,

$$\delta x = \frac{x_\star}{N}. \quad (\text{A.2})$$

The resultant transform in terms of X has units inverse to that of x

$$\delta X = \frac{1}{x_\star} \quad (\text{A.3})$$

and

$$X_\star = \frac{1}{\delta x} = \frac{N}{x_\star}. \quad (\text{A.4})$$

Restated, these relationships are

$$\delta x = \frac{x_\star}{N} \quad x_\star = \frac{1}{\delta X} \quad (\text{A.5})$$

$$\delta X = \frac{1}{x_\star} \quad X_\star = \frac{1}{\delta x}. \quad (\text{A.6})$$

The Chirp-Z Transform

As hinted at, there is a much more interesting way of doing things. Consider a more general type of DFT of the form

$$X_k = \sum_{n=1}^N x_n z_k^n, \quad k = 1, \dots, M \quad (\text{A.7})$$

for N elements of input X_n and M elements of output x_k as a function of the (sampled) complex variable z_k . This is called the chirp-z transform [161] [162]. If

$$z_k = e^{i2\pi k/N}, \quad k = 1, \dots, N, \quad (\text{A.8})$$

Equation A.1 is recovered. Note that the size of x_n and X_k are not the same. The variable z_k is now generalized to a contour in the complex plane

$$z_k = AW^k, \quad k = 1, \dots, N \quad (\text{A.9})$$

where A and W are complex numbers. Specifically, A defines the starting point and W the complex ratio between adjacent points on the contour. For $M = N$, $A = 1$ and $W = \exp(i2\pi/N)$, Equation A.1 is again recovered.

The important property of the chirp-z transform is that both the band-limited resolution and output coordinates can be specified independent of the input. For example, suppose one samples x with N samples of spacing δx . If one wishes to obtain M samples in the output X field with spacing δX beginning with X_1 ,

$$W = \exp(i2\pi\delta x\delta X) \quad (\text{A.10})$$

$$A = \exp(i2\pi X_1\delta x). \quad (\text{A.11})$$

The chirp-z transform can additionally be computed with the same efficiency as the FFT. Consider the relationship

$$nk = \frac{-(k-n)^2}{2} + \frac{n^2}{2} + \frac{k^2}{2}. \quad (\text{A.12})$$

Using Equation A.12, Equation A.1 can be rewritten

$$X_k = \sum_{n=1}^N x_n e^{i2\pi kn/N} \quad k = 1, \dots, N \quad (\text{A.13})$$

$$X_k = e^{i\pi k^2/N} \sum_{n=1}^N \left(x_n e^{i\pi n^2/N} \right) e^{i\pi(k-n)^2/N} \quad k = 1, \dots, N, \quad (\text{A.14})$$

which is simply a convolution. The convolution theorem states that the Fourier transform of the convolution of two functions f and g is simply the product of the Fourier transforms of f and g , namely

$$\mathcal{F}^+((f * g)) = \mathcal{F}^+(x)\mathcal{F}^+(g). \quad (\text{A.15})$$

Through the convolution theorem, the chirp-z transform can be expressed as a pair of FFTs, and thus be efficiently computed.

A.2 Abeles Matrix Formalism

A.2.1 Matrix Formalism

The Fresnel reflection and transmission coefficients r and t for s (transverse-electric) and p (transverse-magnetic) polarization and a single ($i-j$) interface are derived from Equation 2.23, given by

$$r^s = \frac{k_{z,i} - k_{z,j}}{k_{z,i} + k_{z,j}} \quad (\text{A.16})$$

$$r^p = \frac{\epsilon_i k_{z,j} - \epsilon_j k_{z,k}}{\epsilon_i k_{z,j} + \epsilon_j k_{z,k}} \quad (\text{A.17})$$

$$t^s = \frac{2k_{z,i}}{k_{z,i} + k_{z,j}} \quad (\text{A.18})$$

$$t^p = \frac{2\epsilon_i \epsilon_j k_{z,i}}{\epsilon_i k_{z,j} + \epsilon_j k_{z,i}} \quad (\text{A.19})$$

$$(\text{A.20})$$

where the superscript denotes the polarization. Note that k_z can be equivalently expressed either as a function of incident angle θ or k_x

$$k_{z,i} = k_0 \sqrt{\epsilon_i - \epsilon_{i-1} \sin \theta} \quad (\text{A.21})$$

$$= \sqrt{k_0^2 \epsilon_i - k_x^2} \quad (\text{A.22})$$

For multilayer systems, these equations can be applied recursively. In this work we use the much more computationally efficient Abeles matrix formalism [163]. Here, the n th system matrix for s and p polarization, C_n^s and C_n^p , are

$$C_n^s = \begin{pmatrix} e^{-ik_{z,n}d_n} & r_{n,n+1}^s e^{-ik_{z,n}d_n} \\ r_{n,n+1}^s e^{ik_{z,n}d_n} & e^{ik_{z,n}d_n} \end{pmatrix} \quad (\text{A.23})$$

$$C_n^p = \begin{pmatrix} e^{-ik_{z,n}d_n} & r_{n,n+1}^p e^{-ik_{z,n}d_n} \\ r_{n,n+1}^p e^{ik_{z,n}d_n} & e^{ik_{z,n}d_n} \end{pmatrix} \quad (\text{A.24})$$

where n and $n + 1$ are the layer indices for a single interface. A matrix is constructed for each layer of the system and the resultant matrix found as the product of these matrices

$$M^s = \prod_n C_n^s \quad (\text{A.25})$$

$$M^p = \prod_n C_n^p \quad (\text{A.26})$$

From this matrix the system Fresnel coefficients are determined viz.

$$r^p = \frac{M_{21}^p}{M_{11}^p} \quad (\text{A.27})$$

$$r^s = \frac{M_{21}^s}{M_{11}^s} \quad (\text{A.28})$$

$$t^p = \frac{1}{M_{11}^p} \quad (\text{A.29})$$

$$t^s = \frac{1}{M_{11}^s} \quad (\text{A.30})$$

$$(\text{A.31})$$

where the subscripts identify the matrix elements.

A.3 Reference Data

A.4 Colophon

This document was typeset using pdfL^AT_EX. All plots were rendered using pgfplots [164] with styles influenced by EDWARD TUFTE [165] [166]. Colors were chosen from datasets provided by JAN BREWER [167]. Schematics and other line drawings were prepared using Inkscape. Generation of text was done under Arch Linux using vim. Some tables were pre-processed using LyX.

The Monte Carlo simulations were written in c with parallelism accomplished using mpi. The vortex tracking and image processing algorithms were written in octave.

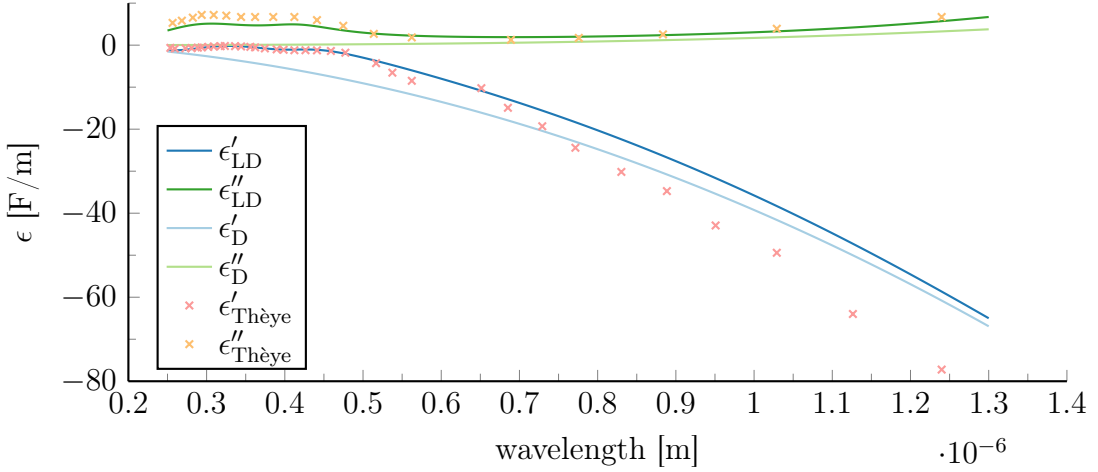


Figure A.2: Comparison of the complex permittivity for gold calculated using the Drude ($\epsilon'_D + i\epsilon''_D$) and the Lorentz Drude ($\epsilon'_L + i\epsilon''_L$) model compared with experimental results by THÈYE [4]

Weirdospace images were processed using python and scipy/numpy. Parallel execution when required was done at FAU RRZE, Erlangen, Germany. Multiple scattering code written by MATTHEW FOREMAN was written in MATLAB. All sources available through the author.

A.5 Dipole-Dipole Simulation

We have constructed a theoretical model which enables fast simulation of the re-radiated SPP field, including multiple scattering effects. The system is modeled as a collection of n dipoles with an induced moment of $\mathbf{p}_n = \vec{\alpha} \mathbf{E}_{\text{exc}}(\mathbf{r}_n)$ from the exciting field \mathbf{E}_0 . The field \mathbf{p}_k seen by each scatterer depends on the field from all other scatterers

$$\mathbf{p}_k = \vec{\alpha}_k \mathbf{E}_0(\mathbf{r}_k) + \omega^2 \mu_0 \vec{\alpha}_k \vec{\mathbf{G}}_s(\mathbf{r}_k, \mathbf{r}_k) \mathbf{p}_k \quad (\text{A.32})$$

$$+ \omega^2 \mu_0 \sum_{\substack{n=1 \\ n \neq k}}^N \vec{\alpha}_k \vec{\mathbf{G}}(\mathbf{r}_k, \mathbf{r}_n) \mathbf{p}_n \quad k = 1, \dots, N \quad (\text{A.33})$$

and the total field $\mathbf{E}(\mathbf{r})$ is evaluated as the sum of each individual dipole field

$$\mathbf{E}(\mathbf{r}) = \mathbf{E}_0(\mathbf{r}) + \omega^2 \mu_0 \sum_{n=1}^N \vec{\mathbf{G}}(\mathbf{r}, \mathbf{r}_n) \mathbf{p}_n \quad (\text{A.34})$$

Bibliography

- [1] F.I. Baida, D.V. Labeke, and J.M. Vigoureux. Theoretical study of near-field surface plasmon excitation, propagation and diffraction. *Optics communications*, 171(4-6):317–331, 1999.
- [2] P Dawson, BAF Puygranier, and JP Goudonnet. Surface plasmon polariton propagation length: a direct comparison using photon scanning tunneling microscopy and attenuated total reflection. *Physical Review B*, 63(20):205410, 2001.
- [3] E Kumacheva. Interfacial friction measurement in surface force apparatus. *Progress in Surface Science*, 58(2):75–120, 1998.
- [4] Marie-Luce Thèye. Investigation of the optical properties of au by means of thin semitransparent films. *Physical Review B*, 2(8):3060, 1970.
- [5] Bora Ung and Yunlong Sheng. Interference of surface waves in a metallic nanoslit. *Optics express*, 15(3):1182–1190, 2007.
- [6] A.D. Rakic, A.B. Djurišić, J.M. Elazar, and M.L. Majewski. Optical properties of metallic films for vertical-cavity optoelectronic devices. *Applied Optics*, 37(22):5271–5283, 1998.
- [7] Jiri Homola, Sinclair S Yee, and Gunter Gauglitz. Surface plasmon resonance sensors: review. *Sensors and Actuators B: Chemical*, 54(1):3–15, 1999.
- [8] Jiri Homola. *Surface plasmon resonance based sensors*, volume 4. Springer, 2006.
- [9] XD Hoa, AG Kirk, and M Tabrizian. Towards integrated and sensitive surface plasmon resonance biosensors: a review of recent progress. *Biosensors and Bioelectronics*, 23(2):151–160, 2007.
- [10] Y-K Kim, PM Lundquist, JA Helfrich, JM Mikrut, GK Wong, PR Auvil, and JB Ketterson. Scanning plasmon optical microscope. *Applied physics letters*, 66(25):3407–3409, 1995.
- [11] YK Kim, JB Ketterson, and DJ Morgan. Scanning plasmon optical microscope operation in atomic force microscope mode. *Optics letters*, 21(3):165–167, 1996.
- [12] Gerd Binnig and Heinrich Rohrer. Scanning tunneling microscopy. *IBM Journal of research and development*, 44(1-2):279–293, 2000.

- [13] RH Ritchie. Plasma losses by fast electrons in thin films. *Physical Review*, 106(5):874, 1957.
- [14] D. Bohm and D. Pines. A collective description of electron interactions. i. magnetic interactions. *Physical Review*, 82(5):625, 1951.
- [15] D. Pines and D. Bohm. A collective description of electron interactions: II. collective vs individual particle aspects of the interactions. *Physical Review*, 85(2):338, 1952.
- [16] R W Wood. On a remarkable case of uneven distribution of light in a diffraction grating spectrum. *Proceedings of the Physical Society of London*, 18(1):269, 1902.
- [17] Lord Rayleigh. III. note on the remarkable case of diffraction spectra described by prof. wood. *Philosophical Magazine Series 6*, 14(79):60–65, 1907.
- [18] E. Kretschmann and H. Raether. Radiative decay of non radiative surface plasmons excited by light. *Z Naturf.*, 230:2135–2136, 1968.
- [19] Heinz Raether. *Springer tracts in modern physics*, volume 111. Springer-Verlag., 1988.
- [20] A. Otto. Excitation of nonradiative surface plasma waves in silver by the method of frustrated total reflection. *Zeitschrift für Physik A Hadrons and Nuclei*, 216(4):398–410, 1968.
- [21] WP Chen, G. Ritchie, and E. Burstein. Excitation of surface electromagnetic waves in attenuated total-reflection prism configurations. *Physical Review Letters*, 37(15):993–997, 1976.
- [22] HJ Simon and JK Guha. Directional surface plasmon scattering from silver films. *Optics Communications*, 18(3):391–394, 1976.
- [23] H. Raether. Surface plasmons on smooth and rough surfaces and on gratings. *Springer Tracts in Modern Physics (Springer, Berlin, 1988)*, 1997.
- [24] B. Liedberg, C. Nylander, and I. Lunstrom. Surface plasmon resonance for gas detection and biosensing. *Sensors and Actuators*, 4:299–304, 1983.
- [25] B. Liedberg, C. Nylander, and I. Lundström. Biosensing with surface plasmon resonance—how it all started. *Biosensors and Bioelectronics*, 10(8):i–ix, 1995.
- [26] R.V. Andaloro, R.T. Deck, and H.J. Simon. Optical interference pattern resulting from excitation of surface mode with diverging beam. *JOSA B*, 22(7):1512–1516, 2005.
- [27] HJ Simon, RV Andaloro, and RT Deck. Observation of interference in reflection profile resulting from excitation of optical normal modes with focused beams. *Optics letters*, 32(11):1590–1592, 2007.
- [28] SL Chuang. Lateral shift of an optical beam due to leaky surface-plasmon excitations. *JOSA A*, 3(5):593–599, 1986.
- [29] R.P. Schumann and S. Gregory. Near-field modification of interference components in surface plasmon resonance. *Arxiv preprint arXiv:0804.3418*, 2008.

- [30] Robert Paul Schumann. *Surface plasmon random scattering and related phenomena*. PhD thesis, University of Oregon, 2009.
- [31] Shechao Feng, Charles Kane, Patrick A Lee, and A Douglas Stone. Correlations and fluctuations of coherent wave transmission through disordered media. *Physical review letters*, 61(7):834, 1988.
- [32] Joseph W Goodman. *Speckle phenomena in optics: theory and applications*, volume 1. Roberts & Company, 2007.
- [33] Joseph W Goodman. Statistical properties of laser speckle patterns. In *Laser speckle and related phenomena*, pages 9–75. Springer, 1975.
- [34] Richard Berkovits and Shechao Feng. Correlations in coherent multiple scattering. *Physics Reports*, 238(3):135–172, 1994.
- [35] Richard Berkovits and Shechao Feng. Theory of speckle-pattern tomography in multiple-scattering media. *Physical Review Letters*, 65(25):3120, 1990.
- [36] Richard Berkovits. Sensitivity of the multiple-scattering speckle pattern to the motion of a single scatterer. *Physical Review B*, 43(10):8638, 1991.
- [37] DJ Pine, DA Weitz, PM Chaikin, and E Herbolzheimer. Diffusing wave spectroscopy. *Physical Review Letters*, 60(12):1134, 1988.
- [38] RG Atkins, RT Shin, and JA Kong. A neural network method for high range resolution target classification. *Progress In Electromagnetics Research*, 4:255–292, 1991.
- [39] Ali Abdi, Cihan Tepedelenlioglu, Mostafa Kaveh, and Georgios Giannakis. On the estimation of the k parameter for the rice fading distribution. *Communications Letters, IEEE*, 5(3):92–94, 2001.
- [40] Eric Larose, Thomas Planes, Vincent Rossetto, and Ludovic Margerin. Locating a small change in a multiple scattering environment. *Applied Physics Letters*, 96(20):204101, 2010.
- [41] Stefan Alexander Maier. *Plasmonics: Fundamentals and Applications: Fundamentals and Applications*. Springer, 2007.
- [42] Oliver Benson. *Elements of Nanophotonics*. Humboldt-Universität zu Berlin, 2009.
- [43] A.F. Oskooi, D. Roundy, M. Ibanescu, P. Bermel, JD Joannopoulos, and S.G. Johnson. Meep: A flexible free-software package for electromagnetic simulations by the fdtd method. *Computer Physics Communications*, 181(3):687–702, 2010.
- [44] Peyman Jahanshahi, Mostafa Ghomeishi, and Faisal Rafiq Mahamd Adikan. Study on dielectric function models for surface plasmon resonance structure. *The Scientific World Journal*, 2014, 2014.
- [45] Iftikhar Ahmed and Zhizhang Chen, editors. *Computational Electromagnetics—Retrospective and Outlook*. Springer, 2015.

- [46] Yuji Kuwamura, Masuo Fukui, and Osamu Tada. Experimental observation of long-range surface plasmon polaritons. *Journal of the Physical Society of Japan*, 52(7):2350–2355, 1983.
- [47] Alan E Craig, Grieg A Olson, and Dror Sarid. Experimental observation of the long-range surface-plasmon polariton. *Optics letters*, 8(7):380–382, 1983.
- [48] Valery N Konopsky and Elena V Alieva. Long-range plasmons in lossy metal films on photonic crystal surfaces. *Optics letters*, 34(4):479–481, 2009.
- [49] Valery N Konopsky and Elena V Alieva. Long-range propagation of plasmon polaritons in a thin metal film on a one-dimensional photonic crystal surface. *Physical Review Letters*, 97(25):253904, 2006.
- [50] Jiri Homola, Ivo Koudela, and Sinclair S Yee. Surface plasmon resonance sensors based on diffraction gratings and prism couplers: sensitivity comparison. *Sensors and Actuators B: Chemical*, 54(1):16–24, 1999.
- [51] S Andréasson, SILAS E GUSTAESSON, and Nils-Olov Halling. Measurement of the refractive index of transparent solids and fluids. *JOSA*, 61(5):595–599, 1971.
- [52] Richard P Brent. *Algorithms for minimization without derivatives*. Courier Dover Publications, 1973.
- [53] D Heitmann and V Permien. Determination of surface roughness from light scattering measurements. *Optics Communications*, 23(1):131–134, 1977.
- [54] M. Piliarik and J. Homola. Surface plasmon resonance (SPR) sensors: approaching their limits? *Optics express*, 17(19):16505–16517, 2009.
- [55] Yung-Kyu Kim, PR Auvil, and JB Ketterson. Conical electromagnetic radiation in the kretschmann attenuated total reflections configuration. *Applied optics*, 36(4):841–846, 1997.
- [56] Johannes Schindelin, Ignacio Arganda-Carreras, Erwin Frise, Verena Kaynig, Mark Longair, Tobias Pietzsch, Stephan Preibisch, Curtis Rueden, Stephan Saalfeld, Benjamin Schmid, et al. Fiji: an open-source platform for biological-image analysis. *Nature methods*, 9(7):676–682, 2012.
- [57] Peter Johansson, R Monreal, and Peter Apell. Theory for light emission from a scanning tunneling microscope. *Physical Review B*, 42(14):9210, 1990.
- [58] C Horstmann. Multiple scattering of plasmons at rough surfaces. *Optics Communications*, 21(1):173–176, 1977.
- [59] E Kretschmann. Decay of non radiative surface plasmons into light on rough silver films. comparison of experimental and theoretical results. *Optics Communications*, 6(2):185–187, 1972.
- [60] D-L Hornauer. Light scattering experiments on silver films of different roughness using surface plasmon excitation. *Optics Communications*, 16(1):76–79, 1976.

- [61] E Kretschmann. *Untersuchungen zur Anregung und Streuung von Oberflächenplasmaschwingungen an Silberschichten*. PhD thesis, Universität Hamburg, 1972.
- [62] E Kröger and E Kretschmann. Scattering of light by slightly rough surfaces or thin films including plasma resonance emission. *Zeitschrift für Physik*, 237(1):1–15, 1970.
- [63] František Mikeš, Yu Yang, Iwao Teraoka, Takaaki Ishigure, Yasuhiro Koike, and Yoshiyuki Okamoto. Synthesis and characterization of an amorphous perfluoropolymer: Poly (perfluoro-2-methylene-4-methyl-1, 3-dioxolane). *Macromolecules*, 38(10):4237–4245, 2005.
- [64] Jorge Jesus Moré. The Levenberg-Marquardt algorithm: Implementation and theory. In *Numerical Analysis, Lecture Notes in Mathematics 630*, Springer Verlag, pages 105–116, 1977.
- [65] Daniel A Steck. Classical and modern optics, June 2006.
- [66] Chak-Fong Cheang, Yi-Cheng Li, Kuo-Chih Chiu, Chun-Yu Lin, Yun-Chorng Chang, and Shean-Jen Chen. Study of nanoprisms via apertureless near-field optical microscopy. In *SPIE OPTO*, pages 79461M–79461M. International Society for Optics and Photonics, 2011.
- [67] Kuo-Chih Chiu, Chun-Yu Lin, Chen Yuan Dong, and Shean-Jen Chen. Optimizing silver film for surface plasmon-coupled emission induced two-photon excited fluorescence imaging. *Optics express*, 19(6):5386–5396, 2011.
- [68] RF Bianchi, MF Panssiera, JPH Lima, L Yagura, AM Andrade, and RM Faria. Spin coater based on brushless dc motor of hard disk drivers. *Progress in organic coatings*, 57(1):33–36, 2006.
- [69] Eva Kocsis, Benes L Trus, Clifford J Steer, Margaret E Bisher, and Alasdair C Steven. Image averaging of flexible fibrous macromolecules: the clathrin triskelion has an elastic proximal segment. *Journal of Structural Biology*, 107(1):6–14, 1991.
- [70] Aaron Webster and Frank Vollmer. Interference of conically scattered light in surface plasmon resonance. *Optics letters*, 38(3):244–246, 2013.
- [71] Xiaonan Shan, Xinpeng Huang, Kyle J Foley, Peiming Zhang, Kangping Chen, Shaopeng Wang, and Nongjian Tao. Measuring surface charge density and particle height using surface plasmon resonance technique. *Analytical Chemistry*, 82(1):234–240, 2009.
- [72] Patrick A Lee and A Douglas Stone. Universal conductance fluctuations in metals. *Physical Review Letters*, 55(15):1622, 1985.
- [73] E Akkermans, PE Wolf, and R Maynard. Coherent backscattering of light by disordered media: Analysis of the peak line shape. *Physical review letters*, 56(14):1471, 1986.

- [74] Isaac Freund, Michael Rosenbluh, and Shechao Feng. Memory effects in propagation of optical waves through disordered media. *Physical review letters*, 61(20):2328, 1988.
- [75] Isaac Freund. ‘1001’correlations in random wave fields. *Waves in random media*, 8(1):119–158, 1998.
- [76] Shechao Feng, Patrick A Lee, and A Douglas Stone. Sensitivity of the conductance of a disordered metal to the motion of a single atom: Implications for 1 f noise. *Physical review letters*, 56(18):1960, 1986.
- [77] Pappu Srinivasa Ravikanth. *Physical one-way functions*. PhD thesis, Massachusetts Institute of Technology, 2001.
- [78] Bruce J Berne and Robert Pecora. *Dynamic light scattering: with applications to chemistry, biology, and physics*. Courier Dover Publications, 2000.
- [79] J Christopher Dainty. Laser speckle and related phenomena. In *Berlin and New York, Springer-Verlag (Topics in Applied Physics. Volume 9)*, 1975. 298 p, volume 9, 1975.
- [80] Eo Jakeman. Speckle statistics with a small number of scatterers. *Optical Engineering*, 23(4):234453–234453, 1984.
- [81] Pavel Zakharov, Frédéric Cardinaux, and Frank Scheffold. Multispeckle diffusing-wave spectroscopy with a single-mode detection scheme. *Physical Review E*, 73(1):011413, 2006.
- [82] Joseph W Goodman. Dependence of image speckle contrast on surface roughness. *Optics Communications*, 14(3):324–327, 1975.
- [83] Xudong Fan, Ian M White, Siyka I Shopova, Hongying Zhu, Jonathan D Suter, and Yuze Sun. Sensitive optical biosensors for unlabeled targets: A review. *Analytica Chimica Acta*, 620(1):8–26, 2008.
- [84] Joseph Wang. Nanomaterial-based amplified transduction of biomolecular interactions. *small*, 1(11):1036–1043, 2005.
- [85] Prashant K Jain, Xiaohua Huang, Ivan H El-Sayed, and Mostafa A El-Sayed. Review of some interesting surface plasmon resonance-enhanced properties of noble metal nanoparticles and their applications to biosystems. *Plasmonics*, 2(3):107–118, 2007.
- [86] Shiping Fang, Hye Jin Lee, Alastair W Wark, and Robert M Corn. Attomole microarray detection of micrornas by nanoparticle-amplified spr imaging measurements of surface polyadenylation reactions. *Journal of the American Chemical Society*, 128(43):14044–14046, 2006.
- [87] Sadagopan Krishnan, Vigneshwaran Mani, Dhanuka Wasalathanthri, Challa V Kumar, and James F Rusling. Attomolar detection of a cancer biomarker protein in serum by surface plasmon resonance using superparamagnetic particle labels. *Angewandte Chemie International Edition*, 50(5):1175–1178, 2011.

- [88] Min Jeong Kwon, Jaeyoung Lee, Alastair W Wark, and Hye Jin Lee. Nanoparticle-enhanced surface plasmon resonance detection of proteins at attomolar concentrations: comparing different nanoparticle shapes and sizes. *Analytical chemistry*, 84(3):1702–1707, 2012.
- [89] Hye Rim Sim, Alastair W Wark, and Hye Jin Lee. Attomolar detection of protein biomarkers using biofunctionalized gold nanorods with surface plasmon resonance. *Analyst*, 135(10):2528–2532, 2010.
- [90] AF Ioffe and AR Regel. Non-crystalline, amorphous and liquid electronic semiconductors. *Progress in Semiconductors*, 4:237–291, 1960.
- [91] Th M Nieuwenhuizen and MCW van Rossum. Role of a single scatterer in a multiple scattering medium. *Physics Letters A*, 177(1):102–106, 1993.
- [92] Yujia Cui and Carlos Bustamante. Pulling a single chromatin fiber reveals the forces that maintain its higher-order structure. *Proceedings of the National Academy of Sciences*, 97(1):127–132, 2000.
- [93] John F Marko and Eric D Siggia. Stretching DNA. *Macromolecules*, 28(26):8759–8770, 1995.
- [94] Hitoshi Suda. Origin of friction derived from rupture dynamics. *Langmuir*, 17(20):6045–6047, 2001.
- [95] Volker Bormuth, Vladimir Varga, Jonathon Howard, and Erik Schäffer. Protein friction limits diffusive and directed movements of kinesin motors on microtubules. *Science*, 325(5942):870–873, 2009.
- [96] Charles L Asbury, Adrian N Fehr, and Steven M Block. Kinesin moves by an asymmetric hand-over-hand mechanism. *Science*, 302(5653):2130–2134, 2003.
- [97] Günter Sauerbrey. Verwendung von schwingquarzen zur wägung dünner schichten und zur mikrowägung. *Zeitschrift für Physik*, 155(2):206–222, 1959.
- [98] K. Keiji Kanazawa and Joseph G. Gordon. Frequency of a quartz microbalance in contact with liquid. *Analytical Chemistry*, 57(8):1770–1771, 1985.
- [99] Diethelm Johannsmann. *Studies of Contact Mechanics with the QCM*, pages 151–170. Springer, 2007.
- [100] Kenneth A Marx. Quartz crystal microbalance: a useful tool for studying thin polymer films and complex biomolecular systems at the solution-surface interface. *Biomacromolecules*, 4(5):1099–1120, 2003.
- [101] GL Dybwad. A sensitive new method for the determination of adhesive bonding between a particle and a substrate. *Journal of Applied Physics*, 58:2789, 1985.
- [102] B Borovsky, J Krim, SA Syed Asif, and KJ Wahl. Measuring nanomechanical properties of a dynamic contact using an indenter probe and quartz crystal microbalance. *Journal of Applied Physics*, 90(12):6391–6396, 2001.

- [103] Aaron Webster, Frank Vollmer, and Yuki Sato. Probing biomechanical properties with a centrifugal force quartz crystal microbalance. *Nature Communications*, October 2014.
- [104] Ken Halvorsen and Wesley P Wong. Massively parallel single-molecule manipulation using centrifugal force. *Biophysical journal*, 98(11):L53–L55, 2010.
- [105] F Eggers and Th Funck. Method for measurement of shear-wave impedance in the mhz region for liquid samples of approximately 1 ml. *Journal of Physics E: Scientific Instruments*, 20(5):523, 1987.
- [106] D Johannsmann, K Mathauer, G Wegner, and W Knoll. Viscoelastic properties of thin films probed with a quartz-crystal resonator. *Physical Review B*, 46(12):7808, 1992.
- [107] Binyang Du, Alexander Martin König, and Diethelm Johannsmann. On the role of capillary instabilities in the sandcastle effect. *New Journal of Physics*, 10(5):053014, 2008.
- [108] SJ Geelhood, CW Frank, and K Kanazawa. Transient quartz crystal microbalance behaviors compared. *Journal of the Electrochemical Society*, 149(1):H33–H38, 2002.
- [109] Stanford Research Systems. *QCM200 Quartz Crystal Microbalance Digital Controller, Operation and Service Manual*. Stanford Research Systems, 2004.
- [110] Yazan Hussain, Jacqueline Krim, and Christine Grant. Ots adsorption: A dynamic qcm study. *Colloids and Surfaces A: Physicochemical and Engineering Aspects*, 262(1):81–86, 2005.
- [111] Daniel E Gottschling, Robert D Grober, and Michael Sailor. Detection of biological warfare agents. 1(10), 2000.
- [112] A Arnau, T Sogorb, and Y Jiménez. Circuit for continuous motional series resonant frequency and motional resistance monitoring of quartz crystal resonators by parallel capacitance compensation. *Review of Scientific Instruments*, 73(7):2724–2737, 2002.
- [113] Shannon L Snellings, Jason Fuller, and David W Paul. Response of a thickness-shear-mode acoustic wave sensor to the adsorption of lipoprotein particles. *Langmuir*, 17(8):2521–2527, 2001.
- [114] Xiaodi Su, Ying-Ju Wu, and Wolfgang Knoll. Comparison of surface plasmon resonance spectroscopy and quartz crystal microbalance techniques for studying DNA assembly and hybridization. *Biosensors and Bioelectronics*, 21(5):719–726, 2005.
- [115] Wendy YX Peh, Erik Reimhult, Huey Fang Teh, Jane S Thomsen, and Xiaodi Su. Understanding ligand binding effects on the conformation of estrogen receptor α -DNA complexes: A combinational quartz crystal microbalance with dissipation and surface plasmon resonance study. *Biophysical Journal*, 92(12):4415–4423, 2007.

- [116] Vytas Reipa, Jamie Almeida, and Kenneth D Cole. Long-term monitoring of biofilm growth and disinfection using a quartz crystal microbalance and reflectance measurements. *Journal of microbiological methods*, 66(3):449–459, 2006.
- [117] Fred L Walls and John R Vig. Fundamental limits on the frequency stabilities of crystal oscillators. *Ultrasonics, Ferroelectrics and Frequency Control, IEEE Transactions on*, 42(4):576–589, 1995.
- [118] KE Heusler, A Grzegorzewski, L Jackel, and J Pietrucha. Measurement of mass and surface stress at one electrode of a quartz oscillator. *Ber. Bunsenges. Phys. Chem.*, 92(11):1218–1225, 1988.
- [119] ED Fletcher and AJ Douglas. A Comparison of the Effects of Bending Moments on the Vibrations of AT and SC (or TTC) Cuts. In *33rd Annual Symposium on Frequency Control. 1979*, pages 346–350. IEEE, 1979.
- [120] Jerry R Norton and Raymond J Besson. Tactical bva quartz resonator performance. In *Frequency Control Symposium, 1993. 47th., Proceedings of the 1993 IEEE International*, pages 609–613. IEEE, 1993.
- [121] M. Valdois, J. Besson, and J.-J. Gagnepain. Influence of environment conditions on a quartz resonator. In *28th Annual Symposium on Frequency Control. 1974*, pages 19–32, 1974.
- [122] Ralf Richter, Anneke Mukhopadhyay, and Alain Brisson. Pathways of lipid vesicle deposition on solid surfaces: a combined QCM-D and AFM study. *Biophysical Journal*, 85(5):3035–3047, 2003.
- [123] Newton C Fawcett, Richard D Craven, Ping Zhang, and Jeffrey A Evans. Evidence for gravity’s influence on molecules at a solid-solution interface. *Langmuir*, 20(16):6651–6657, 2004.
- [124] Minoru Yoshimoto and Shigeru Kurosawa. Effect of immersion angle of a one-face sealed quartz crystal microbalance in liquid. *Analytical Chemistry*, 74(16):4306–4309, 2002.
- [125] Raymond L Filler. The acceleration sensitivity of quartz crystal oscillators: a review. *Ultrasonics, Ferroelectrics and Frequency Control, IEEE Transactions on*, 35(3):297–305, 1988.
- [126] M. Valdois, J. Besson, and J.-J. Gagnepain. Influence of environment conditions on a quartz resonator. In *28th Annual Symposium on Frequency Control. 1974*, pages 19–32, 1974.
- [127] Achilleas Tsortos, George Papadakis, and Electra Gizeli. Shear acoustic wave biosensor for detecting dna intrinsic viscosity and conformation: A study with qcm-d. *Biosensors and Bioelectronics*, 24(4):836–841, 2008.
- [128] Joao M Encarnaçao, Peter Stallinga, and Guilherme NM Ferreira. Influence of electrolytes in the QCM response: Discrimination and quantification of the interference to correct microgravimetric data. *Biosensors and Bioelectronics*, 22(7):1351–1358, 2007.

- [129] Zuxuan Lin and Michael D Ward. The role of longitudinal waves in quartz crystal microbalance applications in liquids. *Analytical Chemistry*, 67(4):685–693, 1995.
- [130] Minoru Yoshimoto, Shin Tokimura, and Shigeru Kurosawa. Characteristics of the series resonant-frequency shift of a quartz crystal microbalance in electrolyte solutions. *Analyst*, 131(10):1175–1182, 2006.
- [131] Richard C Tolman. The electromotive force produced in solutions by centrifugal action. *Journal of the American Chemical Society*, 33(2):121–147, 1911.
- [132] Th. Des Coudres. Unpolarisirbare electrolytische Zellen unter dem Einflusse der Centrifugalkraft. *Annalen der Physik*, 285(6):284–294, 1893.
- [133] Y. Zhang, R. H. Austin, J. Kraeft, E. C. Cox, and N. P. Ong. Insulating behavior of λ -DNA on the micron scale. *Physical Review Letters*, 89:198102, Oct 2002.
- [134] Adam LJ Olsson, Ivan R Quevedo, Danqing He, Mohan Basnet, and Nathalie Tufenkji. Using the quartz crystal microbalance with dissipation monitoring to evaluate the size of nanoparticles deposited on surfaces. *ACS Nano*, 7(9):7833–7843, 2013.
- [135] Hrvoje Jasak, Aleksandar Jemcov, and Zeljko Tukovic. Openfoam: A c++ library for complex physics simulations. In *International workshop on coupled methods in numerical dynamics*, pages 1–20, 2007.
- [136] Francisco Palacios, Michael R Colombo, Aniket C Aranake, Alejandro Campos, Sean R Copeland, Thomas D Economou, Amrita K Lonkar, Trent W Lukaczyk, Thomas WR Taylor, and Juan J Alonso. Stanford university unstructured (su2): An open-source integrated computational environment for multi-physics simulation and design. *AIAA Paper*, 287:2013, 2013.
- [137] Ewa Vittorias, Michael Kappl, Hans-Jürgen Butt, and Diethelm Johannsmann. Studying mechanical microcontacts of fine particles with the quartz crystal microbalance. *Powder Technology*, 203(3):489–502, 2010.
- [138] Claudia Steinem, Andreas Janshoff, and Matthew A Cooper. *Piezoelectric sensors*, volume 5. Springer, 2007.
- [139] Stephen J Martin, Victoria Edwards Granstaff, and Gregory C Frye. Characterization of a quartz crystal microbalance with simultaneous mass and liquid loading. *Analytical Chemistry*, 63(20):2272–2281, 1991.
- [140] Jacob N Israelachvili. *Intermolecular and surface forces: revised third edition*. Academic Press, 2011.
- [141] Barbara M Alexander and Dennis C Prieve. A hydrodynamic technique for measurement of colloidal forces. *Langmuir*, 3(5):788–795, 1987.
- [142] Scott G Flicker, Jennifer L Tipa, and Stacy G Bike. Quantifying double-layer repulsion between a colloidal sphere and a glass plate using total internal reflection microscopy. *Journal of Colloid and Interface Science*, 158(2):317–325, 1993.

- [143] Mukul M Sharma, Habib Chamoun, DSH Sarma, and Robert S Schechter. Factors controlling the hydrodynamic detachment of particles from surfaces. *Journal of Colloid and Interface Science*, 149(1):121–134, 1992.
- [144] Marc André Meyers, Po-Yu Chen, Albert Yu-Min Lin, and Yasuaki Seki. Biological materials: structure and mechanical properties. *Progress in Materials Science*, 53(1):1–206, 2008.
- [145] Fang Li, James H-C Wang, and Qing-Ming Wang. Thickness shear mode acoustic wave sensors for characterizing the viscoelastic properties of cell monolayer. *Sensors and Actuators B: Chemical*, 128(2):399–406, 2008.
- [146] Ang Li, Edmondo M Benetti, Davide Tranchida, Jarred N Clasohm, Holger Schönher, and Nicholas D Spencer. Surface-grafted, covalently cross-linked hydrogel brushes with tunable interfacial and bulk properties. *Macromolecules*, 44(13):5344–5351, 2011.
- [147] Leena Patra and Ryan Toomey. Viscoelastic response of photo-cross-linked poly (n-isopropylacrylamide) coatings by QCM-D. *Langmuir*, 26(7):5202–5207, 2009.
- [148] Amir Zamiri and Suvernu De. Modeling the mechanical response of tetragonal lysozyme crystals. *Langmuir*, 26(6):4251–4257, 2009.
- [149] RE Mahaffy, S Park, E Gerde, JACK Käs, and CK Shih. Quantitative analysis of the viscoelastic properties of thin regions of fibroblasts using atomic force microscopy. *Biophysical Journal*, 86(3):1777–1793, 2004.
- [150] Cynthia M Flanigan, Manishi Desai, and Kenneth R Shull. Contact mechanics studies with the quartz crystal microbalance. *Langmuir*, 16(25):9825–9829, 2000.
- [151] LM Rebelo, JS de Sousa, J Mendes Filho, and M Radmacher. Comparison of the viscoelastic properties of cells from different kidney cancer phenotypes measured with atomic force microscopy. *Nanotechnology*, 24(5):055102, 2013.
- [152] Kang De Yao, Wen Guang Liu, Zhang Lin, and Xiao Hui Qiu. In situ atomic force microscopy measurement of the dynamic variation in the elastic modulus of swollen chitosan/gelatin hybrid polymer network gels in media of different ph. *Polymer international*, 48(9):794–798, 1999.
- [153] Emilios K Dimitriadis, Ferenc Horkay, Julia Maresca, Bechara Kachar, and Richard S Chadwick. Determination of elastic moduli of thin layers of soft material using the atomic force microscope. *Biophysical Journal*, 82(5):2798–2810, 2002.
- [154] Senli Guo and Boris B Akhremtchev. Investigation of mechanical properties of insulin crystals by atomic force microscopy. *Langmuir*, 24(3):880–887, 2008.
- [155] R Merkel, E Sackmann, and E Evans. Molecular friction and epitactic coupling between monolayers in supported bilayers. *Journal de Physique*, 50(12):1535–1555, 1989.

- [156] Ashish S Yeri, Lizeng Gao, and Di Gao. Mutation screening based on the mechanical properties of DNA molecules tethered to a solid surface. *The Journal of Physical Chemistry B*, 114(2):1064–1068, 2009.
- [157] Ofer Tevet, Palle Von-Huth, Ronit Popovitz-Biro, Rita Rosentsveig, H Daniel Wagner, and Reshef Tenne. Friction mechanism of individual multilayered nanoparticles. *Proceedings of the National Academy of Sciences*, 108(50):19901–19906, 2011.
- [158] J Krim, DH Solina, and R Chiarello. Nanotribology of a kr monolayer: A quartz-crystal microbalance study of atomic-scale friction. *Physical Review Letters*, 66(2):181–184, 1991.
- [159] Matteo Frigo and Steven G Johnson. Fftw: An adaptive software architecture for the fft. In *Acoustics, Speech and Signal Processing, 1998. Proceedings of the 1998 IEEE International Conference on*, volume 3, pages 1381–1384. IEEE, 1998.
- [160] James W Cooley and John W Tukey. An algorithm for the machine calculation of complex fourier series. *Mathematics of computation*, 19(90):297–301, 1965.
- [161] Lawrence R Rabiner, Ronald W Schafer, and Charles M Rader. The chirp z-transform algorithm and its application. *Bell System Technical Journal*, 48(5):1249–1292, 1969.
- [162] L Rabiner, Ronald W Schafer, and Charles M Rader. The chirp z-transform algorithm. *Audio and Electroacoustics, IEEE Transactions on*, 17(2):86–92, 1969.
- [163] F Abeles. Sur la propagation des ondes électromagnétiques dans les milieux stratifiés. 3(4):504–520, 1948.
- [164] Christian Feuersänger. Pgfpplots-a la-tex package to create normal/logarithmic plots in two and three dimensions, 2014.
- [165] Edward R Tufte and PR Graves-Morris. *The visual display of quantitative information*, volume 2. Graphics press Cheshire, CT, 1983.
- [166] Edward R Tufte. Envisioning information. *Optometry & Vision Science*, 68(4):322–324, 1991.
- [167] Mark Harrower and Cynthia A Brewer. Colorbrewer.org: an online tool for selecting colour schemes for maps. *Cartographic Journal, The*, 40(1):27–37, 2003.

Declaration of Originality

I affirm that the work presented in this dissertation is, to the best of my knowledge, original and my own, except as acknowledged in the text.

Hiermit erkläre ich, diese Arbeit selbständig angefertigt und keine anderen als die zugelassenen Hilfsmittel verwendet zu haben.

Erlangen, Saturday 16th April, 2016

Aaron Webster

Acknowledgements

I would like to extend my sincerest gratitude to the following individuals who contributed to this work: JIAPENG HUANG, for his enthusiasm and focused efforts in carrying out many tedious but necessary experiments, YUQIANG WU for establishing the DNA related protocols, MATTHEW FOREMAN for insightful theoretical modeling of SPP multiple scattering and for significant contributions to the quality of this dissertation, FRANK VOLLMER for his creativity and optimism in seeking out new ideas and seeing this work to a successful completion, STEPHEN GREGORY and R.P. SCHUMANN whose pioneering experiments are the basis for my own, and YUKI SATO for his patience and progressive scientific ideas regarding the CF-QCM. This gratitude is also extended to MARTIN BAASKE who knows where I'm coming from. Most significantly, I would like to recognize NORBERT LINDLEIN who invited me to Germany and showed me true scientific rigor, without whom this dissertation would not be possible.